Thermomechanical Modeling of Oxidation Effects in Porous Ultra-High Temperature Ceramics

Brenton A. Morris

Thesis submitted to the Faculty of the

Virginia Polytechnic Institute and State University

in partial fulfillment of the requirements for the degree of

Master of Science

in

Aerospace Engineering

Gary D. Seidel, Chair

Carolina Tallon

Rakesh K. Kapania

May 11, 2021

Blacksburg, Virginia

Keywords: Oxidation, Ultra-High Temperature Ceramics, Macroporosity, Material Point Method, Titanium Diboride

Copyright 2021, Brenton A. Morris

Thermomechanical Modeling of Oxidation Effects in Porous Ultra-High Temperature Ceramics

Brenton A. Morris

(ABSTRACT)

The effects of oxidation in the thermomechanical response of porous TiB_2 have been investigated. An in-house quasi-static material point method tool was used to perform two-dimensional plane strain simulations on unoxidized hexagonal representative volume elements (RVEs) with macroporosity volume fractions of 10%, 40% and 70% to establish a baseline for the response due to geometric effects. Compressive strains of up to 30% were applied at room temperature. The 10% and 40% RVEs showed shear banding and subsequent shear failure of the inter-pore struts, while shear banding in 70% RVE weakened the struts, which lead to buckling failure. A snapshot oxidation model was then applied to the hexagonal RVEs in place of a transient, diffusion-based oxidation solver. Compressive strain simulations were performed on RVEs with oxide layers ranging from 5 to 50 µm. In RVEs with porosity of 40% or higher, oxide percolation in the struts reduced the effective elastic modulus and compressive strength, though further oxidation beyond the percolation point did not have a significant impact. Ramped and cyclic thermal loads were applied and the damage due to thermal expansion coefficient mismatch at the oxide-substrate interface decreased as the oxide layer was increased. Finally, the snapshot oxidation modeling approach was applied to large porous RVEs derived from micro-computed tomography images of TiB_2 foam. The effective elastic modulus decreased by 47% when the 5 µm layer was applied due to many thin, flexible struts becoming fully oxidized. Subsequent oxidation did not have a significant impact on the thermomechanical response.

Thermomechanical Modeling of Oxidation Effects in Porous Ultra-High Temperature Ceramics

Brenton A. Morris

(GENERAL AUDIENCE ABSTRACT)

Thermal loading experienced by hypersonic flight vehicles has posed significant design challenges in the development of platforms for military and re-entry applications. The advent of hypersonic strike weapons and waveriders has led to an interest in utilizing ceramics with melting points above 3000°C, called ultra-high temperature ceramics (UHTCs), that offer improved resistance to high-temperature oxidation. Beyond load-carrying applications, UHTCs imbued with macroscale porosity have been introduced as candidates for providing thermal insulation of sensitive on-board components. This thesis presents a first pass at modeling the coupled effects of oxidation and continuum damage in the thermomechanical response of such materials. Using an in-house material point method tool, two-dimensional compressive strain simulations were performed on hexagonal representative volume elements (RVEs) of TiB_2 foam with varying levels of macroporosity, along with large porous RVEs derived from micro-computed tomography images of TiB_2 foam. A snapshot oxidation model was applied to these RVEs in place of a transient, diffusion-based oxidation solver, then simulations with applied compressive strains of up to 30% were performed on RVEs with oxide layers ranging from 5 to 50 µm. Ramped and cyclic thermal loads were applied to explore the effects of thermal expansion mismatch between the substrate and oxide phases. The oxide layers were shown to reduce the effective stiffness, compressive strength, and thermal conductivity of the RVEs, with the oxidation state of the inter-pore struts having a large impact on the overall material response.

Acknowledgments

I would first like to thank my advisor, Dr. Gary Seidel, for providing a tremendous amount of support over the past year. Given my accelerated time frame, I largely attribute the completion of this thesis to his persistent encouragement and guidance. I am grateful for his unwavering commitment to this effort, even when I had doubts of my own. In my view, he exceeded his obligations as my advisor, sacrificing much of his own time to ensure that I had a complete and meaningful experience that will undoubtedly be beneficial in my future endeavors. Above all, I would like to thank Dr. Seidel for being a mentor who has taught me a great deal throughout my graduate studies.

I would also like to thank my advisory committee members, Dr. Carolina Tallon and Dr. Rakesh Kapania. Dr. Tallon, for providing crucial insights from her expertise in the fabrication and characterization of ceramics, and Dr. Kapania for sharing his knowledge of solid mechanics through various courses and individual discussions throughout my time at Virginia Tech. Furthermore, thank you to my colleagues in the Seidel Research Group for bringing me into the fold, albeit for a short time. Special thanks are due to Stefan Povolny, whose recent Ph.D. work served as the foundation for this research effort. In addition to developing the code employed in this work, Stefan added functionalities that enabled the objectives set forth in this thesis to be achieved and often shared helpful observations regarding the simulation results.

On a professional level, I would like to acknowledge the mentorship provided by Dr. Pradeep Raj and Dr. H. Pat Artis and thank them for allowing me to serve as the teaching assistant for their capstone aircraft design course sequence. Additionally, I am grateful for the generosity of the Virginia Tech Aerospace and Ocean Engineering department in providing

me with a graduate assistantship. I would also like to acknowledge those within Lockheed Martin's Advanced Development Programs who provided me with many opportunities to expand and deepen my knowledge of airframe structural analysis.

On a personal level, I would like to acknowledge the support of my friends and family. Thank you to my father, Jeff, and brother, Logan, for helping me find balance throughout my academic journey. Thank you to my mother, Cindy, for instilling in me a fraction of her tenacity and optimism, elements that were essential to the completion of this thesis. I am also grateful for the support of my closest friends, Colby White and Khanh Nguyen.

Finally, I must express my sincerest gratitude for the love and support of my fiancé, Brenna, whose steadfast encouragement kept me moving forward even at my lowest points. I admire the patience and understanding she has shown throughout our years together and am deeply grateful for the sacrifices she made to help this work come into existence.

Contents

List of Figures **ix**

List of Tables **xvii**

1 Introduction **1**

2 Motivation & Background **3**

2.1 High Temperature Material Exposure 3

2.2 Material Usage in Hypersonic Flight Vehicles 4

2.3 Ultra-High Temperature Ceramics 5

3 Oxidation Kinetics & Modeling **8**

3.1 Oxidation Behavior in C/C and UHTCs 8

3.2 Oxidation Resistance and Mechanical Response 10

3.3 Modeling of Oxidation Kinetics in UHTCs 11

4 Thermomechanical Material Point Method **16**

4.1 Quasi-Static Material Point Method 16

4.2 Effective Properties 20

5 Baseline Hexagonal RVE Simulations **24**

5.1 TiB_2 Material Properties & 1D Modeling 24

5.1.1 Temperature-Dependent Material Properties 24

5.1.2 Solution for Uniaxial Bar with Uniform Temperature Distribution . . 27

5.1.3 1D Finite Element Solution for Uniaxial Bar 27

5.2 2D Plane Strain Simulations 30

5.2.1 Hexagonal Representative Volume Element 31

5.2.2 Simulation Boundary Conditions 32

5.3 Compressive Loading of Hexagonal RVEs 34

5.3.1 Effects of Ramped Thermal Loading 41

5.3.2 Effects of Cyclic Thermal Loading 45

5.3.3 Compressive Loading Takeaways 49

5.4 Effective Thermal Conductivity of Hexagonal RVEs 50

6 Oxidation Model Implementation in the MPM 53

6.1 Snapshot Oxidation Model 53

6.1.1 Oxide Layer Thickness 53

6.1.2 Two-Phase Temperature-Dependent Material Properties 60

6.2 Compressive Loading of Hex Snapshots 63

6.2.1 Mechanical Response of Hex Snapshots with 40% Porosity 64

6.2.2 Mechanical Response of Hex Snapshots with 10% Porosity 81

6.2.3 Mechanical Response of Hex Snapshots with 70% Porosity 86

6.2.4 Effect of Macroporosity on Hex Snapshot Mechanical Reponse 91

6.3 Effective Thermal Conductivity of Hex Snapshots 93

6.4 Extension to Large Porous TiB_2 RVE 97

6.4.1 Large Porous RVE & Boundary Conditions 97

6.4.2 Compression of Large Porous RVE Snapshots 100

6.4.3 Thermal Conductivity of the Large Porous RVE 108

7 Conclusions **111**

Bibliography **120**

Appendices **126**

Appendix A Simulation Result Verification **127**

A.1 Numerical Noise in Constrained Cyclic Thermal Loading Simulations 127

List of Figures

2.1 X-ray tomography (a) and SEM (b) images of TiB_2 foam samples. 7

3.1 SEM micrographs of fracture surface of TiB_2 specimen exposed to air (A) at 800°C for 10 h and (B) at 1200°C for 2 h 9

5.1 Temperature-dependent material properties for TiB_2. 26

5.2 Load configuration for uniaxial bar problem with uniform temperature distribution 27

5.3 Elongation of the uniaxial bar over a range of uniform temperature distributions 28

5.4 Load configuration for 1D FEM problem with applied heat flux and thermal boundary 29

5.5 Temperature and Elastic Modulus distributions for 1D FEM solution with 1000 linear elements 29

5.6 Elongation for the 1D FEM problem with an applied heat flux boundary condition compared against the uniform temperature solution 30

5.7 Hexagonal RVEs containing varying levels of macroporosity to represent TiB_2 foam 31

5.8 Mechanical and thermal boundary conditions applied to the hexagonal RVE 32

5.9 Profile of the thermal loads applied to the top boundary of the RVE 33

5.10 Stress vs. compressive strain curves for hexagonal RVEs with 10%, 40%, and 70% macroporosity at room temperature. 35

5.11 Damage vs. compressive strain curves for hexagonal RVEs with 10%, 40%, and 70% macroporosity at room temperature. 35

5.12 Contour plots of the principal stress fields at the corresponding macro-damage initiation strain of each baseline RVE. 38

5.13 Damage field contour plots for each RVE showing the response at (a) the corresponding macro-damage initiation strain, (b) one load step beyond the macro-damage initiation strain, and (c) 21% applied engineering strain . . . 40

5.14 Compressive stress vs. time for hexagonal RVEs with 10%, 40%, and 70% macroporosity subjected to the ramped applied thermal load and no applied engineering strain. 41

5.15 Stress vs. compressive strain curves for hexagonal RVEs with 10%, 40%, and 70% macroporosity with the ramped applied thermal load 42

5.16 Damage vs. compressive strain curves for hexagonal RVEs with 10%, 40%, and 70% macroporosity with the ramped applied thermal load 42

5.17 Contour plots of temperature and damage parameter fields for the hexagonal RVE with 70% macroporosity subjected to ramped thermal loading and 10.2% compressive strain. Snapshots represent the field parameters when $t = 18s$. . 44

5.18 Compressive stress vs. time for hexagonal RVEs with 10%, 40%, and 70% macroporosity subjected to the cyclic applied thermal load and no applied engineering strain. 45

5.19 Stress vs. compressive strain curves for hexagonal RVEs with 10%, 40%, and 70% macroporosity with the cyclic applied thermal load 46

5.20 Damage vs. compressive strain curves for hexagonal RVEs with 10%, 40%, and 70% macroporosity with the cyclic applied thermal load 46

5.21 Contour plots of temperature and damage parameter fields for the hexagonal RVE with 40% macroporosity subjected to ramped thermal loading and 15% compressive strain. Snapshots represent the field parameters when $t = 26s$. . 48

5.22 Comparison of the elastic and damage metrics for the unoxidized hexagonal RVEs subjected to each applied thermal load. 50

5.23 Variation in effective thermal conductivity with applied compressive load for varying levels of macroporosity 52

6.1 Oxidized Hexagonal RVE Snapshots with 10% macroporosity 56

6.2 Oxidized Hexagonal RVE Snapshots with 40% macroporosity 57

6.3 Oxidized Hexagonal RVE Snapshots with 70% macroporosity 58

6.4 Oxide thickness vs. exposure time for TiB_2 exposted to air at 1200°C. 59

6.5 Temperature-dependent material properties for TiO_2 shown with previously established functions for TiB_2. 62

6.6 Profile of the thermal load applied to the top boundary of the hexagonal RVE. 63

6.7 Stress vs. compressive strain curves for hexagonal RVEs with 40% macroporosity at varying levels of oxidation. 64

6.8 Damage vs. compressive strain curves for hexagonal RVEs with 40% macroporosity at varying levels of oxidation. 65

6.9 Contour plots of the 2nd principal stress fields for hex snapshots of $t_{ox} = 15$ µm (a) and $t_{ox} = 30$ µm (b) at their respective micro-damage initiation strains. 66

6.10 Damage field contour plots for hex snapshot with 40% macroporosity showing the room temperature response at the corresponding macro-damage initiation strain with varying levels of oxide layer thickness 67

6.11 Damage field contour plots for RVEs with oxide layers of (a) 30 µm and (b) 50 µm subjected to 21% applied compressive strain 68

6.12 Damage field contour plots for hex snapshot with 40% macroporosity showing the room temperature response at 22.8% applied compressive strain with varying levels of oxide layer thickness 69

6.13 Compressive stress-time curves for hexagonal RVEs with 40% macroporosity subjected to the ramped thermal load at varying levels of oxidation. 70

6.14 Damage-time curves for hexagonal RVEs with 40% macroporosity subjected to the ramped thermal load at varying levels of oxidation. 70

6.15 Damage field contour plots for hex snapshots with 40% macroporosity showing the response at $t = 49s$ with a ramped thermal load and no applied engineering strain 71

6.16 Stress vs. compressive strain curves for hexagonal RVEs with 40% macroporosity subjected to the ramped thermal load at varying levels of oxidation. . 72

6.17 Damage vs. compressive strain curves for hexagonal RVEs with 40% macroporosity subjected to the ramped thermal load at varying levels of oxidation. 72

6.18 Compressive stress-time curves for hexagonal RVEs with 40% macroporosity subjected to the cyclic thermal load at varying levels of oxidation. 74

6.19 Damage (a) and tensile damage (b) vs. time curves for hexagonal RVEs with 40% macroporosity subjected to the cyclic thermal load at varying levels of oxidation. 75

6.20 Damage field contour plots for hex snapshots with 40% macroporosity subjected to the cyclic thermal load. The left and right columns for each oxide layer show $t = 48s$ and $t = 50s$, respectively. 76

6.21 Stress vs. compressive strain curves for hexagonal RVEs with 40% macroporosity subjected to the cyclic thermal load at varying levels of oxidation. . . 77

6.22 Damage vs. compressive strain curves for hexagonal RVEs with 40% macroporosity subjected to the cyclic thermal load at varying levels of oxidation. . 77

6.23 Stress vs. compressive strain curves for hexagonal RVEs with 40% macroporosity subjected to each thermal load at varying levels of oxidation. 78

6.24 Damage vs. compressive strain curves for hexagonal RVEs with 40% macroporosity subjected to each thermal load at varying levels of oxidation. 78

6.25 Metric comparison for the 40% porous hex snapshot across all three thermal load cases. 79

6.26 Stress vs. compressive strain curves for hexagonal RVEs with 10% macroporosity subjected to the ramped thermal load at varying levels of oxidation. . 81

6.27 Damage vs. compressive strain curves for hexagonal RVEs with 10% macroporosity subjected to the ramped thermal load at varying levels of oxidation. 82

6.28 Damage field contour plots for hex snapshot with 10% macroporosity showing the response at the corresponding macro-damage initiation strain with varying levels of oxide layer thickness 84

6.29 Damage field contour plots for hex snapshot with 10% macroporosity showing the response at 21% applied engineering strain with varying levels of oxide layer thickness 85

6.30 Stress vs. compressive strain curves for hexagonal RVEs with 70% macroporosity subjected to the ramped thermal load at varying levels of oxidation. . 86

6.31 Damage vs. compressive strain curves for hexagonal RVEs with 70% macroporosity subjected to the ramped thermal load at varying levels of oxidation. 87

6.32 Damage field contour plots for hex snapshot with 70% macroporosity showing the response at the corresponding macro-damage initiation strain with varying levels of oxide layer thickness 89

6.33 Damage field contour plots for hex snapshot with 70% macroporosity showing the response at 12% applied engineering strain with varying levels of oxide layer thickness 90

6.34 Metric comparison for oxidized hex snapshots of all three macroporosity volume fractions subjected to ramped thermal loading. 92

6.35 Effective thermal conductivity vs. oxide thickness at room- and elevated temperatures. Rule of mixtures prediction shown with dashed lines. 95

6.36 Variation of effective thermal conductivity in hexagonal RVEs with the applied engineering load at room temperature and 1000 K 96

6.37 Large porous RVE CT image with binarization and addition of artificial porosity performed by Povolny et al. 97

6.38 Mechanical boundary conditions applied to the large porous RVE 98

6.39 Thermal boundary conditions applied to the large porous RVE 98

6.40 Oxidized Large Porous RVE Snapshots with 70% macroporosity 99

6.41 Stress vs. compressive strain curves (a,b) and Damage vs. compressive strain curves (c) for the large porous RVE at room temperature. 101

6.42 Overlay of the volume-averaged compressive stresses in the 1- (solid) and 2-directions (dashed) for the hexagonal RVE with 70% macroporosity (blue) and large porous RVE (red). 102

6.43 Thin struts throughout the RVE are oxidized after just the first snapshot, thus creating a network of flexible joints that strongly influence the overall mechanical response. 102

6.44 Damage contours for a small region of the RVE at oxidation levels of $t_{ox} = 0 - 15\,\mu m$ for a compressive strain of 3% at room temperature. 103

6.45 Stress-time curves (a,b) and damage-time curves (c) for the large porous RVE subjected to constrained ramped thermal loading. 104

6.46 Stress vs. compressive strain curves (a,b) and Damage vs. compressive strain curves (c) for the large porous RVE subjected to ramped thermal loading. . 105

6.47 Stress-time curves (a,b) and damage-time curves (c) for the large porous RVE subjected to constrained ramped thermal loading. 106

6.48 Stress vs. compressive strain curves (a,b) and damage-strain curves (c) for the large porous RVE subjected to cyclic thermal loading. 107

6.49 Variation of effective thermal conductivity with the applied engineering load at room temperature (solid) and 1000 K (dashed) 110

6.50 Effective thermal conductivity vs. oxide thickness at room temperature and 1000 K 110

A.1 Damage-time response for fully constrained baseline hexagonal RVEs with no applied engineering strain. 127

A.2 Damage-field contour plot corresponding to $t = 50s$ the fully constrained baseline hexagonal RVE with 10% macroporosity and no applied engineering strain. 128

List of Tables

5.1 Elastic and damage properties of hexagonal RVE snapshots with various levels of macroporosity at room temperature 36

5.2 Elastic and damage properties of hexagonal RVE snapshots with various levels of macroporosity with the ramped applied thermal load 43

5.3 Elastic and damage properties of hexagonal RVE snapshots with various levels of macroporosity with the cyclic applied thermal load 47

5.4 Effective thermal conductivity of hexagonal RVE snapshots with various levels of macroporosity [Units: $W/(m-K)$] 51

6.1 Volume fractions of TiO_2 for oxidized hex snapshots with 10%, 40%, and 70% macroporosity. 55

6.2 Room temperature material properties for dense, fully sintered TiB_2 and TiO_2 62

6.3 Elastic and damage properties of hexagonal RVE snapshot with 40% macroporosity at room temperature at various levels of oxidation 65

6.4 Elastic and damage properties of 40% hexagonal RVE snapshots with the ramped thermal load applied at various levels of oxidation 73

6.5 Elastic and damage properties of 40% hexagonal RVE snapshots with the cyclic thermal load applied at various levels of oxidation 77

6.6 Elastic and damage properties of 10% hexagonal RVE snapshots with the ramped thermal load applied at various levels of oxidation 82

6.7 Elastic and damage properties of 70% hexagonal RVE snapshots with the ramped thermal load applied at various levels of oxidation 87

6.8 Effective thermal conductivity of hexagonal RVE snapshots at various oxide layer thicknesses as determined by **simulation** 94

6.9 Effective thermal conductivity of hexagonal RVE snapshots at various oxide layer thicknesses as determined by **rule of mixtures** 94

6.10 Effective elastic modulus of oxidized large porous RVE snapshots for different thermal load cases. 108

6.11 Effective thermal conductivity of large porous RVE snapshots at various oxide layer thicknesses as determined by **simulation** [Units: $W/(m-K)$] 109

Chapter 1

Introduction

The thermal loading experienced by hypersonic flight vehicles, those traveling at Mach 5+, has posed significant design challenges in the development of platforms for military and re-entry applications. The level of structural, propulsive, and radio-frequency [1] performance these vehicles can achieve is a direct function of high-temperature material capability [2]. The harsh thermal environment induced by aerodynamic heating while traveling at high velocities requires these vehicles to be equipped with a Thermal Protection System (TPS) to prevent structural failure before the mission has been completed [3]. Passive TPS solutions, such as blunt-body geometry and ablative ceramic tiles, are often used to maintain the structural integrity of hypersonic vehicles [3]. Proposed active TPS solutions, including leading edge or heat shield cooling via circulating refrigerant, have not been fielded in modern hypersonic vehicles [4]. The advent of hypersonic strike weapons and waveriders has led to an interest in utilizing ceramics with melting points above 3000°C [5], called ultra-high temperature ceramics (UHTCs), in sharp leading edges where the blunt body approach would result in an unacceptable aerodynamic performance deficit [6].

UHTCs offer improvement in oxidation resistance over traditional carbon-carbon (C/C) leading edges that deteriorate when subjected to long exposure times in high-temperature environments [7]. The benefit of using UHTCs is clear, but manufacturing these ceramics and testing them in a simulated operating environment is both challenging and expensive [5]. This motivates the development of computational tools that can predict the effects

of oxidation and damage under thermomechanical load. While commercial finite element software packages offer a range of thermal modeling tools, oxidation modeling can currently only be added with user-defined subroutines. A more robust approach is to add an oxidation damage model to an existing open-source structural analysis tool, which allows for greater control over the solver and could lead to smoother integration with more complex modeling tools. For instance, such a tool could be implemented as the material response solver for a coupled fluid-structure interaction model. Inputs regarding the physical state and chemical composition of the high-speed flow can be passed to this material solver to determine the structure's response and select the ideal composition or microstructure to achieve the performance desired. Another advantage of improving an open-source code is the ability to model two-phase materials, such as nanostructure-toughened UHTCs. Ultimately, modeling the effects that oxidation has on the mechanical properties of a structure is critical to improving the properties of UHTCs and shortening the development time of hypersonic vehicles.

The objective of this research effort is to develop and integrate an oxidation damage model within an existing computational tool for predicting the elastic modulus and thermal conductivity of UHTCs which have been subjected to thermomechanical loading.

Chapter 2

Motivation & Background

In this chapter, the physical and chemical processes that affect materials exposed to high-temperatures are discussed. Then a brief history of material usage in hypersonic flight vehicles is presented to provide further context for the application of the desired computational tool. This is followed by an overview of UHTCs with a focus on introducing UHTCs with multiscale porosity for weight reduction and improved thermal insulation.

2.1 High Temperature Material Exposure

The primary phenomena that occur in materials exposed to oxygen-rich environments at high temperatures are ablation and oxidation, which have distinctly different effects on the structure. Ablation is an endothermic reaction that protects the vehicle by means of consuming exterior material. Further incoming convective heat flux is blocked by the outflow of hot gasses that result from this process, thereby protecting the vehicle at the cost of surface recession [8]. Coupling between a flow field solver and material response solver, otherwise known as fluid-structure interaction (FSI) modeling, is required to accurately capture the aerothermodynamic physics of ablation [9]. Such a model is beyond the scope of this research effort due to the computational complexity and heavy focus on fluid mechanics.

Oxidation occurs when oxygen reacts with the material's external surface and inner pores to convert the substrate into reaction products such as TiO_2 or B_2O_3, given a TiB_2 substrate.

Oxidation has been found to reduce the compressive strength, elastic modulus, and flexural strength of high-temperature materials significantly [7], [10]. Unlike ablation, investigating oxidation damage in high-temperature materials is possible because the solid is converted to oxide-based reaction products rather than being carried away with the boundary layer flow. In addition to experimental oxidation testing, mathematical and numerical models have been developed to determine oxide layer thickness and growth rate [11], [12]. Implementing such models within a finite element method (FEM) or material point method (MPM) solver would provide even more information about the correlation between oxidation and continuum damage.

2.2 Material Usage in Hypersonic Flight Vehicles

Since the late 1950s, a variety of missile, spacecraft, and high-speed aircraft platforms have required careful consideration of thermal loads. One of the earliest examples of this is the North American X-15, which used Inconel and titanium to manage the thermal loads on its leading edges and substructure [3]. The X-15 also featured antennas and skin panels that were coated in silicon elastomeric ablative insulation. Aside from this early ablative coating, the X-15 relied on the high thermal conductivity of its metallic airframe to draw heat away from the nose cone and leading edges, then radiate or convect that thermal energy back into the atmosphere [3]. A similar approach was adopted on early intercontinental ballistic missiles and re-entry vehicles, which featured metallic heat shields with blunt-body geometry. Through further development of intercontinental ballistic missiles and re-entry vehicles, ablative ceramics quickly replaced metallic heat shields as the baseline for TPS design. The downside to relying on ablation was the lack of reusability, an issue that was addressed in the design of the Space Shuttle and the proposed Lockheed X-33 [3]. The

Shuttle incorporated reinforced carbon-carbon (C/C) composites to protect the nose cone and wing leading edges for multiple re-entry heating cycles, as reinforced C/C was found to maintain its strength and thermal shock resistance at high temperatures. Additionally, the C/C plates were coated with SiC to provide improved oxidation resistance [3].

Emerging hypersonic platforms, including air-breathing cruise missiles and boost-glide strike weapons, have followed suit by using reinforced C/C leading edges and aeroshells. The NASA X-43 and Boeing X-51, both air-breathing hypersonic waveriders, share similar construction including C/C leading edges, steel keel beams, aluminum and titanium bulkheads, and both ceramic and steel skin panels [13]. The use of C/C was taken a step further on the DARPA HTV-2 hypersonic boost-glide demonstrator. On HTV-2, the aeroshell was constructed of C/C with an ablative SiC coating applied to the leading edge [14]. While C/C is an excellent choice for aeroshell components due to its increased strength at high temperatures, it is highly vulnerable to oxidation. The SiC coating was necessary to prevent rapid oxidation that would otherwise deteriorate the leading edge when exposed to high temperatures [14]. Uncoated C/C begins to oxidize at 450°C [7], thus it stands no chance of surviving for an extended duration at hypersonic speeds. Many studies have investigated the improvement of C/C oxidation resistance by including SiC and UHTC coatings and matrix additives [7], [15], [16], [17]. Further research in high-temperature and ultra-high temperature materials, along with the related modeling and fabrication techniques, is a critical step in the continued development of hypersonic platforms.

2.3 Ultra-High Temperature Ceramics

In addition to enhancing the oxidation resistance of C/C composites, UHTCs offer a moderate coefficient of thermal expansion, high thermal conductivity, and high bending strength

at high temperatures [7]. Given these benefits, several refractory diborides (ZrB_2, HfB_2, and TiB_2) have been proposed for hypersonic applications, specifically for use in leading edges [11, 18]. Despite their advantages, UHTCs suffer from low fracture toughness, poor thermal shock resistance, and low damage tolerance. Processing UHTCs is also a challenge, given that achieving uniform densification at low temperatures (usually only possible at high temperatures, which leads to poor mechanical properties) requires additives such as SiC [7]. Similar to C/C composites, UHTCs have been shown to benefit from SiC coatings in terms of increased oxidation resistance [19–21]. Furthermore, colloidal processing routes have been shown to enable near-net shaping of UHTC components with the complex geometries required to meet the aerothermodynamic performance needs of hypersonic vehicles [22–24].

Beyond the purposes of withstanding extreme heat fluxes that result in temperatures of up to 3000°C on leading edges or combustors of hypersonic vehicles, UHTCs have recently been discussed as good candidates for providing thermal insulation of critical components within these vehicles. Taking advantage of several ceramic processing techniques, Tallon et al. [25] proposed multiscale porous UHTC materials to be used as thermal insulators between hot external UHTC components and cooler interior components. Key benefits of porous UHTCs include a reduction in the thermal expansion coefficient mismatch between heat zones and the insulator, improved oxidation resistance over C/C or ceramic oxides, maintained thermal stability, and vehicle weight reduction. The use of several ceramic processing techniques, including the sponge replica method, particle-stabilized foam (PSF) gel-casting, ice templating, and partial sintering, resulted in ZrB_2 and TiB_2 specimens, such as the one shown in 2.1(a), with total porosities of up to 93% with pore sizes ranging from 80 to 1000 µm. Hicks et al. employed electrospun polymer fibers to imbue TiB_2 with pores ranging from 5 to 21 µm that resulted in total porosities of up to 72% [26].

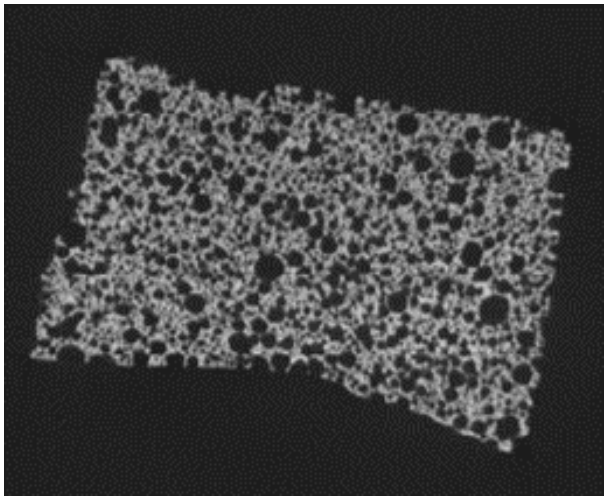

(a) X-ray tomography image of TiB_2 foam with 84% porosity. Reprinted with permission from Tallon et al. [25]

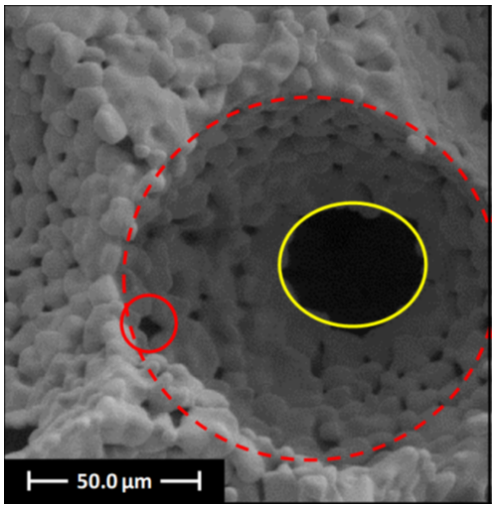

(b) SEM image of multiscale porosity achieved in TiB_2 foam. Reprinted with permission from Povolny et al. [27]

Figure 2.1: X-ray tomography (a) and SEM (b) images of TiB_2 foam samples.

These previous efforts focused on the processing techniques required to achieve near-net shaping of multiscale porous UHTCs, as well as the characterization of the material's effective elastic modulus and thermal conductivity through mechanical testing and numerical simulation. Related works by Povolny et al. [27, 28] involve multiscale modeling of TiB_2 foam obtained through PSF gel-casting (to induce macroporosity) and subsequent partial sintering (which imbues up to 30% microporosity). Figure 2.1(b) scanning electron microscope (SEM) image of TiB_2 foam containing multiscale porosity. The solid red circle indicates a micropore, which has a length scale of 1 µm, while the dashed red circle indicates a macropore with a length scale of 100 µm. The yellow ellipse highlights the intersection of two macropores. This material is also the subject of the current research, which seeks to add oxidation effects to the thermomechanical characterization of TiB_2 foam. Numerical prediction of the thermal conductivity, stiffness, and strength of oxidized porous UHTCs will allow tailoring of the microstructure via processing refinement to generate materials that are well-suited for use in hypersonic vehicles.

Chapter 3

Oxidation Kinetics & Modeling

This chapter discusses the oxidation kinetics that occur in C/C and UHTCs at high temperatures. Then a brief summary of attempts that have been made to characterize UHTC performance and model oxidation in high-temperature environments is presented. Emphasis is placed on the difficulty in creating a transient, diffusion-based oxidation model for implementation alongside material response solver.

3.1 Oxidation Behavior in C/C and UHTCs

For C/C composites exposed to temperatures below 600°C, oxidation is caused by chemical reactions at active spots on the material surface [7]. Active spots are the result of porosity, density, production method, impurity, and residual stress on the material surface. Between 600 and 800°C, the diffusion velocity of oxygen through surface pores governs the reaction [7]. Beyond the transition temperature, the diffusion velocity of oxygen in the boundary layer controls the oxidation rate [7]. In general, the kinetics are very similar for UHTCs. The oxidation behavior of dense TiB_2 specimens with 2.5 wt% Si_3N_4 as a sintering aid exposed to air at temperatures of 800°and 1200°C was investigated by Koh et al. [29]. Figure 3.1 shows SEM micrographs of the fracture surface for TiB_2 specimens after oxidation in both temperature regimes.

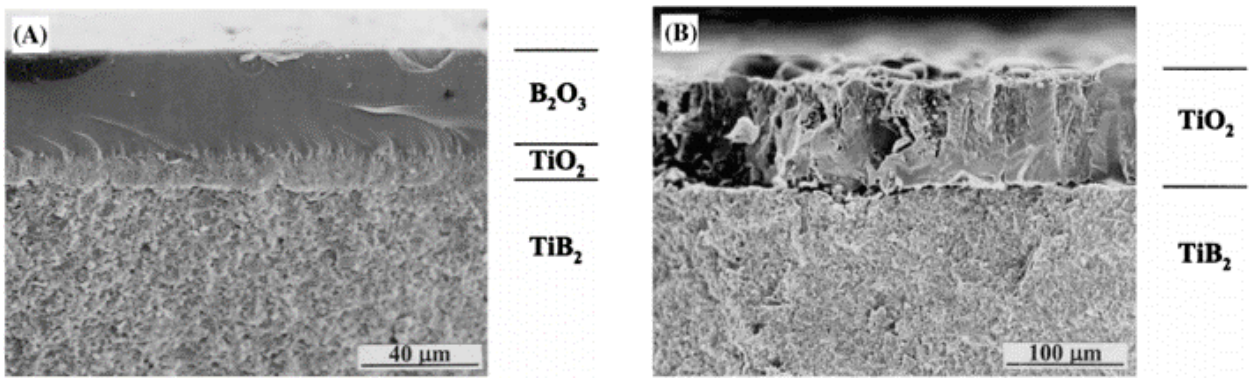

Figure 3.1: "SEM micrographs of fracture surface of TiB_2 specimen exposed to air (A) at 800°C for 10 h and (B) at 1200°C for 2 h." Reprinted with permission from John Wiley and Sons (License Number: 5047771331056) from [29], Copyright 2001

Depending on the exposure temperature, one of the two following reactions is known to be dominant:

$$\mathrm{TiB_2}(s) + \frac{5}{2}\,\mathrm{O_2}(g) = \mathrm{TiO_2}(s) + \mathrm{B_2O_3}(l) \tag{3.1}$$

$$\mathrm{B_2O_3}(l) = \mathrm{B_2O_3}(g) \tag{3.2}$$

Given the parabolic weight gain reported and the presence of both $TiO_2(s)$ and $B_2O_3(l)$, it is clear that reaction 3.1 dominates the low temperature oxidation kinetics. Note that the B_2O_3 phase is liquid at high temperatures but becomes solid once the specimen is cooled to room temperature, as shown in Figure 3.1(A). The authors note an initial weight gain attributed to the formation of $TiO_2(s)$ and $B_2O_3(l)$, followed by a slight decrease in weight. It was postulated that once the amount of oxidation products reached a certain value, the vaporization of $B_2O_3(l)$ occurred rapidly according to reaction 3.2, thus causing slight weight loss [29]. In the specimen oxidized at 1200°C, the vaporization of $B_2O_3(l)$ occurs instantaneously at the oxide-substrate interface, thus no $B_2O_3(l)$ phase is present in the SEM image.

The reaction in this high temperature regime is:

$$\mathrm{TiB_2}(s) + \frac{5}{2}\,\mathrm{O_2}(g) = \mathrm{TiO_2}(s) + \mathrm{B_2O_3}(g) \tag{3.3}$$

This results in a two-phase specimen consisting of the TiB_2 substrate and a 100 µm thick layer of TiO_2 (corresponding to a 10 h exposure time). This study highlights the complexities of the oxidation kinetics in UHTCs, even without the addition of toughening mechanisms. In the context of continuum mechanics modeling, representing the liquid phase present at lower temperatures would require significant modifications to in-house computational tools.

3.2 Oxidation Resistance and Mechanical Response

With surface defects leading to the creation of active spots that accelerate oxidation, refined densification and nanostructure-toughening techniques can be used to improve both the strength and oxidation resistance of C/C composites and UHTCs. Different additives have been considered for improving the oxidation resistance of these materials, with SiC being the most common. The literature contains many studies of UHTC performance at high temperatures, including studies of UHTCs containing some vol% of SiC [19–21]. The performance of ZrB_2 with SiC content ranging from 20 to 80 vol% was evaluated at 1773 and 2073 K with observations being made about the oxidation reaction pathways, the formation and thickness of a protective SiO_2 surface coating, and possible UHTC density reduction with SiC additives [21]. Similar tests were performed on sharp leading edge samples of HfB_2-20 vol% SiC using a direct-connect scramjet rig, where emphasis was placed on interpreting oxide scale thickness via physics-based models [30].

Recent efforts by Silvestroni et al. investigated ZrB_2 containing WC and SiC in a supersonic arc-jet wind tunnel, exposing the ceramic to temperatures of 2650 and 2800 K to explore the dependency of oxidation behavior on oxygen content in the flow and the vol% of WC or SiC [31]. This brief sample reflects the general nature of the research being performed on oxidation in UHTCs, as most researchers focus on the thickness and makeup of the oxide layer, rather than the structural properties. That said, several studies have investigated the temperature dependencies of mechanical properties for ZrB_2 and TiB_2 specimens [19, 32]. Munro compiled the results of the literature for monolithic TiB_2, publishing a wide range of material properties for temperatures up to 2000°C [32]. Neuman et al. performed similar experiments for ZrB_2 with SiC added, publishing elastic modulus, flexural strength, and fracture toughness values for temperatures up to 1600°C [19]. Though these investigations of high-temperature mechanical properties mention oxidation and even capture oxide layer thickness, they do not provide a direct link between oxidation and damage. Further testing and modeling is required to isolate the effects of oxidation from that of general high-temperature exposure.

3.3 Modeling of Oxidation Kinetics in UHTCs

The literature contains various methods for modeling oxidation which have been considered for implementation within an in-house computational tool. Parthasarathy et al. formulated a mechanistic model for the oxidation behavior of ZrB_2, HfB_2 and TiB_2 within the temperature range of 1000-1800°C, specifically predicting weight change, substrate recession, and scale thickness [11]. Other oxidation models presented in the literature have been developed as tools for interpreting experimental data, rather than as models derived from first principles

[17, 30]. For instance, the aforementioned study of HfB_2 leading edge samples included a combined aerothermal-oxidation model, which was based on experimental data from furnace tests, to account for the observed oxide scale thickness at the tip [30].

Bongiorno et al. discussed the formulation of a model for oxygen transport through the oxide scale of ZrB_2 and HfB_2 using first principles, simulations, and experimental results [33]. The model itself is not presented, but several challenges were acknowledged. First, the explicit modeling of the microstructural evolution of a complex oxide scale demands continuum-based methods due to complex 3D microstructures with coexisting material phases. Beyond this, incorporation of the mechanical and thermal conditions suggests that equations for stress and heat diffusion may need to be solved simultaneously with mass transport equations [33]. Despite these difficulties, they reiterate that predictive models which can identify optimum UHTC composition and microstructures for use in the hypersonic flight environment are highly desirable [33].

Similar to the shortage of oxidation-specific damage data, there is a lack of oxidation damage modeling efforts. Radhi et al. conducted a finite element analysis of a ZrB_2-30 vol% SiC composite to investigate the self-healing properties of the oxidation process [34]. This model couples oxygen kinetics with quasi-brittle damage propagation, where an Arrhenius relation is used to connect the oxidative reaction to the change of a damage parameter. It is important to note that the damage parameter captures the damage and the self-healing characteristics of passive oxidation only [34]. A potential improvement of this effort would be to consider the material loss that comes from active oxidation. While this study did indeed link oxidation to damage, few modeling efforts make this connection.

Since the goal of this effort is to implement an oxidation model within an existing computational tool, a better understanding of the oxidation kinetics that govern the process is required. As a first step, oxidation can be viewed in a macroscopic, one-dimensional sense

as being governed by Fickian diffusion. The following equation, gives a simple oxide layer growth model [12]:

$$\frac{dx}{dt} = n\,(2D)^n\,t^{n-1} \tag{3.4}$$

where n is determined by the Pilling-Bedworth ratio to have a value of either 1 or 0.5 to indicate linear or parabolic scale growth, respectively. D is the diffusion coefficient, which may be solved for via Fick's Second Law [12]. This offers a first pass at obtaining the thickness of the oxide layer as a function of time, allowing the oxidation of a material domain to become a boolean function of distance from the nearest exposed surface. This model is valid with the assumption that the material is nonporous in the parabolic growth stage, meaning it would not be directly applicable to UHTC foams that have some degree of microporosity. Modifications would need to be made to account for the change in diffusion rate due to porosity. That, along with the complexities in solving for the diffusion coefficient, make implementing the seemingly simple model a non-trivial exercise.

Further challenges develop when moving into modeling a 2D material system which incorporates macroscale porosity. One approach to implement the 1D growth law in a 2D material is considering one boundary of the material specimen to be exposed to an oxygen-rich environment, then specify a time-dependent oxide front that grows into the material from this boundary. An improvement of this approach for porous materials specifically would be to grow the oxide layer according to Equation 3.4 from every pore surface. Computationally speaking, this would require calculating the normal vector at each point along these surfaces and specifying the oxide depth offset from those points at each time step. While this could have been a reasonable first step, the focus of the research shifted to investigating a 2D diffusion-based oxidation model.

It was postulated that the oxidation state of any point in the material domain could be specified by determining the temperature and oxygen content at that point, which necessitates a two-dimensional diffusion solver. The governing equation to be solved in this case comes from the three-dimensional form of Fick's Second Law, also called the diffusion equation [35]:

$$\frac{\partial c}{\partial t} = D\nabla^2 c \tag{3.5}$$

where c is the concentration of oxygen and D is again the diffusion coefficient, which is assumed to be independent of direction. By solving the diffusion equation to determine the oxygen content and simultaneously solving for the temperature at any point in the material domain, the reaction in Equation 3.1 could be used to inform the oxidation state of that domain. While this may seem simple at first glance, there are two major obstacles that prevent the connection of the diffusion equation solution to an oxidation state for eventual thermomechanical simulation. The first of which is determining what reaction should occur in any given material region given a specified oxygen concentration, especially when there is not sufficient concentration to cause the reaction given in Equation 3.1.

An alternate approach would be developing a ternary phase diagram of the Ti-B-O system, which could be used to explicitly define what reactions occur given concentrations of the three species at a certain temperature. While data for this ternary system were not available in the literature, Hosoda et al. presented a phase diagram for the Al-Ti-B-O quaternary system in the context of understanding the phase reactions of Al-based metal matrix composites [36]. The quaternary phase diagram can be interpreted as a tetrahedron with the vertices representing 100% concentration of each of the four species, respectively. This implies that each face represents a ternary system where the concentration of the fourth species is always 0%, thus the system presented by Hosoda et al. could theoretically be

used to back out the phase reactions of the Ti-B-O species of interest. However, to fully determine the phase reactions, quaternary phase diagrams at several temperatures must be linearly interpolated between. Unfortunately, these data were not found anywhere in the literature, thus preventing meaningful results from being drawn from the diffusion equation solution.

Even if there were sufficient data to inform accurate phase reactions, a second obstacle arises in the form of lacking the connection between the oxidation state and the associated damage. In addition to predicting the mechanical response, another complexity is understanding the connection between microcracks caused by mechanical damage and the change in oxygen diffusion rate, a situation not present in the test data or models available in the literature. While an attempt could be made to connect the oxide layer thickness model developed by Parthasarathy et al. [37] to the passive oxidation damage model presented by Radhi et al. [34], a high level of insight into both models would be necessary. Given the limited nature of their respective publications, this solution would not be feasible within the scope of this research effort. Furthermore, the oxidation model of Parthasarathy et al. [37] was developed under several constraining assumptions, namely that there was no diffusion of oxygen through solid ZrO_2 or TiO_2 so diffusion only occurs through cylindrical pores in the oxide layer. This explicit definition of the oxide scale configuration limits the approach's application to a general concentration state-based oxidation model.

It is clear that although oxidation kinetics are well understood in terms of weight recession, substrate recession, and oxide layer thickness, there is much progress to be made in utilizing phase reactions to link oxygen diffusion to mechanical properties. Thus, a more reasonable first-pass approach is the snapshot oxidation model to be discussed in Chapter 6, which captures oxidation effects based on known experimental oxide growth data without being inhibited by the aforementioned obstacles.

Chapter 4

Thermomechanical Material Point Method

The computation tool used to perform simulations on oxidized UHTCs considered herein was an in-house MPM code developed by Povolny et al. This chapter presents the motivation for selecting this code over more conventional tools, along with details of the mechanical and thermal aspects of the code. These details are available in [28], but a summary of the governing equations is presented here to offer a more complete view of the modeling effort. The brittle damage model employed in the code is discussed, then an overview of the theory for determining the effective thermomechanical properties of the material is provided. Since the focus of this thesis is the integration of oxidation effects in an existing tool, a full review of previous works which employed numerical simulations to determine the thermomechanical response of porous UHTCs is not included. Such a review was performed by Povolny et al. to motivate the development of the MPM tool discussed herein, thus more details on the background of these simulations can be found in [27, 28].

4.1 Quasi-Static Material Point Method

As identified by Povolny et al. [27], a wide range of computational approaches, including Mori-Tanaka micromechanics and the FEM, have been used to assess the performance of

UHTCs under compressive loading. Given the large deformation and self-contact behavior observed in porous UHTCs subjected to compressive strains of up to 30%, the FEM and MPM were considered the strongest candidates for use in this effort. The decision to proceed with the MPM rather than FEM was based on the following considerations: The FEM is a widely used and well-understood method for modeling elasto-plastic solids, but Jiang et al. point out that it "requires additional computational components in the case of large deformation, mesh distortion, fracture, self-collision, and coupling between multi-phase materials" [38]. Special solvers and strategies are often required to handle these other complex cases. The MPM discretizes a continuum body into a number of small Lagrangian material points, which are overlaid upon an Eulerian background mesh [27]. The material points carry all physical properties, or state variables, of the continuum whereas the Eulerian grid carries no permanent information.

At the beginning of each computational iteration, information is transferred from material points to the computational mesh, which is used as a scratchpad to determine an incremental solution of the equations of motion that is interpolated back to the material points. The MPM employs the FEM to perform the interpolation and background grid solving, though it avoids the aforementioned pitfalls of the FEM and is therefore successful in simulating self-collision and crack propagation without mesh entanglement or large deformation errors [28]. Acknowledging that the MPM may be more computationally expensive than the FEM for simple simulations, but offers numerous advantages for the simulations considered in this study, the MPM was selected. Simulations using the hexagonal RVE were performed by Povolny et al. to validate the performance of the MPM against the FEM in the elastic regime. Redundant simulations have not been performed during this research effort. Recent improvements of Povolny's code include adding temperature-dependent thermal and mechanical properties as direct inputs, thus allowing the properties of monolithic TiB_2 to be

developed based on data provided by Munro [32], which is discussed in section 5.1.

The MPM code solves a series of coupled heat transfer and elasticity equations, which were derived by Povolny et al. [28]. The governing equations and brittle damage model are repeated here to provide context for the simulations, but further details of the MPM algorithm covered extensively in [27, 28] are not presented. We begin with the governing differential equation for transient heat transfer with continuum damage, presented using indicial notation:

$$\rho C_p \dot{T} = (1-d)kT_{,kk} \tag{4.1}$$

where ρ is the mass density of the material, C_p is the specific heat at constant pressure, k is the thermal conductivity, T is the temperature field as a function of the Cartesian coordinate and time, and d is the continuum damage parameter. Conservation of linear momentum is given by

$$\sigma_{ij,j} + b_i = 0, \tag{4.2}$$

and serves as the basis for the equations of elasticity. Here σ_{ij} is the Cauchy stress tensor and b_i is the spatial body force. Note that inertial forces are considered negligible. Next, the constitutive relations are introduced to connect deformations to stresses, beginning with the displacement field:

$$u_i = x_i - X_i \tag{4.3}$$

where X_i is the reference coordinate. This allows for the definition of the deformation gradient:

$$F_{ij} = \frac{\partial x_i}{\partial X_j} \tag{4.4}$$

Seeking to employ the St. Venant-Kirchhoff constitutive model for hyperelastic materials

requires the definition of the Green-Lagrange strain:

$$E_{ij} = \frac{1}{2}(F_{ki}F_{kj} - \delta_{ij}) \tag{4.5}$$

where δ_{ij} is the Kronecker delta, and the 2nd Piola-Kirchoff stress tensor:

$$S_{ij} = JF_{ik}^{-1}\sigma_{kl}F_{jl}^{-1} \tag{4.6}$$

where $J = \det \mathbf{F}$. This stress tensor can be expanded to incorporate thermal and damage effects by assuming linear thermo-hyperelasticity supplemented with continuum damage [28]:

$$S_{ij} = (1-d)C_{ijkl}(E_{kl} - \alpha\Delta T\delta_{kl}) \tag{4.7}$$

where C_{ijkl} is the fourth-order stiffness tensor. Finally, the two-dimensional plane strain assumption employed in this study allows the computational domain of a transversely isotropic material to correspond directly to the plane of isotropy. Therefore, we can assume that the St. Venant-Kirchoff constitutive law takes the form:

$$S_{ij} = (1-d)[\lambda E_{kk}\delta ij + 2\mu E_{ij} - (3\lambda + 2\mu)\alpha\Delta T\delta_{kl}] \tag{4.8}$$

where λ and μ are the Lamé constants, α is the volumetric coefficient of thermal expansion, and ΔT is the change in temperature relative to a reference temperature of $T_{ref} = 293$ K [28]. A tensile-only modification of the Mazars damage evolution law for brittle materials is used to determine d, which can be expressed in tensile and compressive parameters, d_t and d_c, respectively [39]. The decomposition is given as:

$$d = \alpha_t d_t + (1-\alpha_t)d_c, \quad 0 \leq \alpha_t \leq 1 \tag{4.9}$$

where α_t is a scalar indicating the amount of tensile strain present in a material point. The damage law requires that both d_t and d_c monotonically increase, however the use of α_t allows the overall damage parameter d to decrease if a material point becomes loaded in compression. The self-contact initiated by compressive loading allows load transfer and re-establishes a conductive pathway. It was assumed that compressive strains produce no damage, which is reasonable considering that UHTCs exhibit exceptionally high compressive strengths relative to their tensile strengths [32]. This reduces the damage parameter to just $d = \alpha_t d_t$. The Mazars damage evolution law for d_t takes the form:

$$d_t(\tilde{\varepsilon}) = 1 - \frac{\tilde{\varepsilon}_0(1-A)}{\tilde{\varepsilon}} - A\exp(-B(\tilde{\varepsilon} - \tilde{\varepsilon}_0)), \quad 0 \leq d_t \leq 1 \tag{4.10}$$

where $\tilde{\varepsilon}$ is the equivalent strain, $\tilde{\varepsilon}_0$ is the damage initiation strain, A dictates the amount of residual stress, and B controls the damage evolution rate. As in [27], $A = 1$ (corresponding to zero residual stress after full damage) and $B = 500$ to emulate brittle failure for all simulations performed in this effort. Equations 4.1, 4.2, 4.8, and 4.10 represent the full set of governing differential equations, which are coupled in terms of temperature-induced volumetric strains and continuum damage that affects both thermal and mechanical solutions.

4.2 Effective Properties

Effective thermomechanical properties can be determined from the MPM code by employing the computational homogenization approach presented by Povolny et al. [28]. Determining the effective elastic constants in the plane strain simulations performed herein is accomplished by using the transversely isotropic version of the St. Venant-Kirchhoff law. The transversely isotropic stiffness tensor is written in Voigt notation as:

$$\begin{pmatrix} C_{11} & C_{12} & C_{13} & 0 & 0 & 0 \\ C_{12} & C_{11} & C_{13} & 0 & 0 & 0 \\ C_{13} & C_{13} & C_{33} & 0 & 0 & 0 \\ 0 & 0 & 0 & C_{44} & 0 & 0 \\ 0 & 0 & 0 & 0 & C_{44} & 0 \\ 0 & 0 & 0 & 0 & 0 & \frac{C_{11}-C_{12}}{2} \end{pmatrix} \tag{4.11}$$

where the 3-direction corresponds to the out-of-plane direction. Homogeneous boundary conditions can then be applied to the background grid of the RVE as described by the following equation:

$$(u_1, u_2) \cdot \hat{n} = (0, \varepsilon_{22}^{app} X_2) \cdot \hat{n} \quad \forall (X_1, X_2) \in \partial\Omega_{\text{grid}} \tag{4.12}$$

where X_1 and X_2 are the Cartesian reference position, u_1 and u_2 are the Cartesian displacement components, $\hat{n}$ is the oriented normal vector on the boundary of the background grid $\partial\Omega_{\text{grid}}$ and ε_{22}^{app} is the applied engineering strain [28]. By the average strain theorem, the volume-averaged engineering strain is then taken as ε_{22}^{app} directly, which generates a Green-Lagrange strain of:

$$E_{22}^{app} = \frac{1}{2}\left((1 + \varepsilon_{22}^{app})^2 + 1\right) \tag{4.13}$$

The Cauchy stress tensor components σ_{11} and σ_{22}, which are output by the MPM code, can be used to calculate the volume-averaged 2nd Piola-Kirchhoff stress tensor components $\langle S_{11} \rangle$ and $\langle S_{22} \rangle$ via Equation 4.6 in the absence of thermal strains. These components allow the in-plane elastic constants to be determined as [28]:

$$C_{11}^{eff} = \frac{\langle S_{11} \rangle}{E_{22}^{app}} \tag{4.14}$$

$$C_{12}^{eff} = \frac{\langle S_{22} \rangle}{E_{22}^{app}} \tag{4.15}$$

These two material constants are sufficient to determine the effective elastic and shear moduli, E^{eff} and G^{eff} [27]:

$$\mathrm{E}^{eff} = \frac{\left(C_{12}^{eff} - C_{11}^{eff}\right)\left(C_{12}^{eff} + 2C_{11}^{eff}\right)}{C_{12}^{eff} + C_{11}^{eff}} \tag{4.16}$$

$$\mathrm{G}^{eff} = \frac{\left(C_{12}^{eff} - C_{11}^{eff}\right)}{2} \tag{4.17}$$

Under the plane strain assumption, which allows the RVE domain to be considered isotropic, these moduli can be used in conjunction with Hooke's law to determine the effective Poisson's ratio ν^{eff}:

$$\nu^{eff} = \frac{C_{11}^{eff}}{C_{11}^{eff} + C_{12}^{eff}} \tag{4.18}$$

The second effective thermomechanical property of interest is the effective thermal conductivity k^{eff}, which is computed using Fourier's law of heat conduction:

$$\langle q_2 \rangle = -k^{eff}\frac{dT}{dx_2} \tag{4.19}$$

where $\langle q_2 \rangle$ is the volume-averaged heat flux in the 2-direction. The temperature gradient on the RHS can be approximated as:

$$\frac{dT}{dx_2} \approx \frac{\Delta T}{\Delta x_2} \tag{4.20}$$

where ΔT is the temperature difference between the top and bottom boundaries, which is prescribed to be very small (1 °C), and Δx_2 is the height of the RVE, which will vary depending on the length-scale interpretation of the RVEs. Rearranging Equation 4.19 and measuring $\langle q_2 \rangle$ from the MPM code output allows k^{eff} to be calculated as:

$$k^{eff} = \frac{-\langle q_2 \rangle}{\Delta T / \Delta x_2} \tag{4.21}$$

In addition to the effective elastic modulus and thermal conductivity, the effective coefficient

of thermal expansion α^{eff} was considered by Povolny et al. [28]. While this property was not calculated for the oxidized materials considered herein, it is of interest for future oxidation studies. Calculation of this property requires a two-step process where the RVE is first allowed to expand in response to a temperature rise, then the same temperature rise is prescribed in addition to an applied engineering strain. Further details of this calculation are given in [28].

Chapter 5

Baseline Hexagonal RVE Simulations

5.1 TiB_2 Material Properties & 1D Modeling

It is desired to add oxidation effects to an existing MPM tool. Since the literature lacks data directly linking oxidation behavior to mechanical damage, building a transient, chemistry-based oxidation model would not be an appropriate first step. Such a model may be useful for predicting oxide scale thickness, but it would not yield any information about material performance. An alternate initial approach is defining temperature-dependent material properties based on available experimental data. This captures the known high-temperature behavior of the material but does not account for oxidation effects explicitly. Regardless, several example problems were solved with increasing levels of complexity, which serve as the foundation for the final tool.

5.1.1 Temperature-Dependent Material Properties

Data for the variation in the material properties of fully dense TiB_2 with temperature, compiled by Munro [32], have been fit using the *Find Fit* function in *Wolfram Mathematica* [40]. Knowledge of the mechanical and thermal solver inputs for the existing MPM tool led to fitting functions for six material properties: elastic modulus, density, damage-initiation strain, specific heat, thermal conductivity, and thermal expansion coefficient. The temperature-

dependent functions are plotted against the data from which they were derived in Figure 5.1. For both elastic modulus and density, a 1st-order fit was selected due to their relatively linear behavior between room temperature and 2200 K:

$$E = 574.3 - 0.03164T \tag{5.1}$$

$$\rho = 4545 + 0.1269T \tag{5.2}$$

The damage initiation strain, defined in Chapter 5, was estimated by assuming that bulk TiB_2 exhibits brittle behavior that is characteristic of ceramic materials. This implies that the stress-strain response will remain linear until failure occurs, at which the stress equals the tensile strength σ_t. Therefore, the strain-to-failure can be expressed as:

$$\tilde{\varepsilon_0} = \frac{\sigma_t}{E} \tag{5.3}$$

By applying a 1st-order fit to the flexural strength (interpreted as tensile strength) data provided by Munro [32], a function for the damage initiation strain was derived:

$$\tilde{\varepsilon_0} = 6.619 \times 10^{-4} + 1.547 \times 10^{-7}T \tag{5.4}$$

Expressions for the specific heat and thermal conductivity were provided explicitly by Munro [32], both of which exhibit significant temperature dependency:

$$C_p = 976 - 426\exp[-0.008(T - 273)] + 0.21(T - 273) \tag{5.5}$$

$$k = 77.3 + 8270\exp[-0.002(T - 273)](T + 137)^{-1} \tag{5.6}$$

Finally, a 1st-order fit was selected for the thermal expansion coefficient:

$$\alpha = 7.007 \times 10^{-6} + 1.229 \times 10^{-9}T \tag{5.7}$$

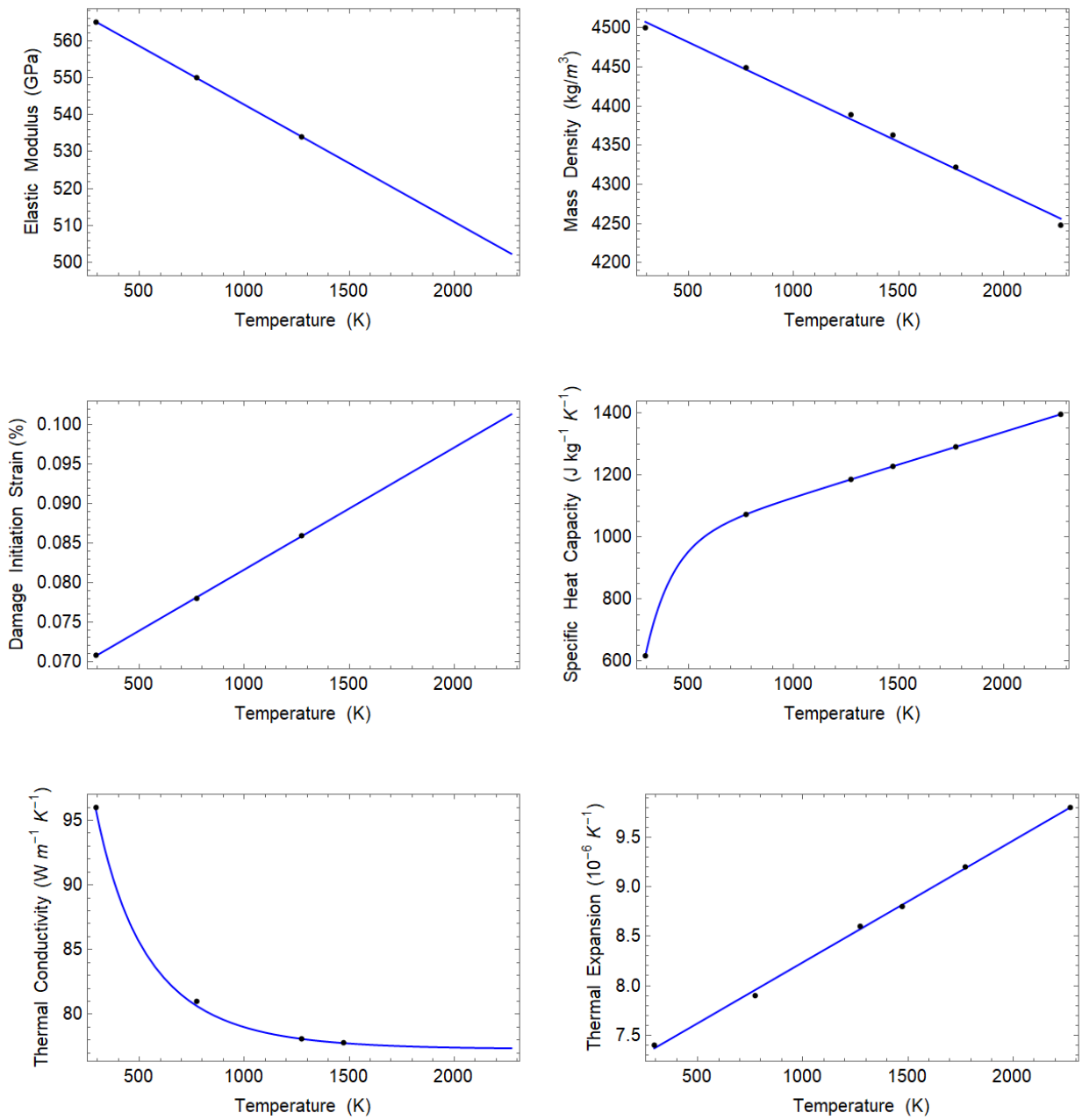

Figure 5.1: Temperature-dependent material properties for TiB_2. The data points represent experimental values from Munro [32] and the blue curves show the data fit used.

5.1.2 Solution for Uniaxial Bar with Uniform Temperature Distribution

As a first-pass implementation of the elastic modulus function, the governing differential equation for an axial bar was solved using boundary conditions consistent with the diagram shown in Figure 5.2 and a uniform temperature distribution. Details of the governing equation, along with essential and natural boundary conditions, are readily available in solid mechanics textbooks, such as that of J. N. Reddy [41]. The length, L, and cross-sectional area, A, of the bar were selected to be 1 m and 0.05 m^2, respectively, while the magnitude of the quadratic distributed load, p_0, is 10×10^3 N/m and the applied tip force, F_{tip}, is 5,000 N. This axial bar problem was solved at a range of temperatures and the elongation of the bar for each temperature is shown in Figure 5.3. As expected, the solutions show that the elongation increases as the temperature increases due to the reduction in stiffness at high temperatures.

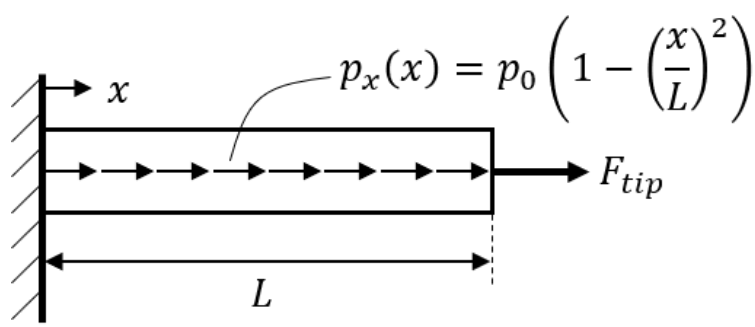

Figure 5.2: Load configuration for uniaxial bar problem with uniform temperature distribution

5.1.3 1D Finite Element Solution for Uniaxial Bar

Next, a non-uniform temperature distribution was investigated. The heat conduction and axial bar solutions were calculated using a 1D FEM approach, wherein the heat conduction

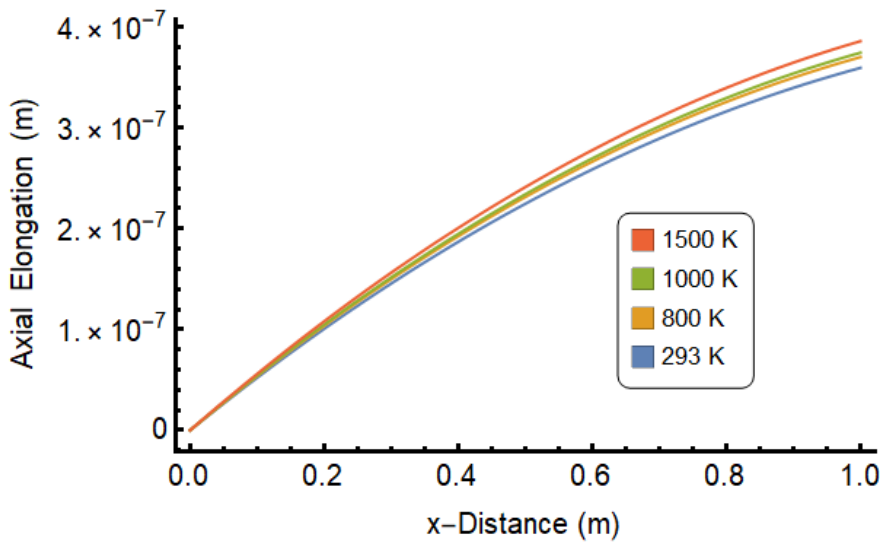

Figure 5.3: Elongation of the uniaxial bar over a range of uniform temperature distributions

problem was solved for each element, allowing the temperature-dependent elastic modulus to be determined across the domain. Details of the 1D FEM approach used are described by Reddy [41]. The thermal conductivity was assumed to vary with temperature as given by Equation 5.6, thus the heat conduction problem was solved iteratively until the temperature reached steady-state, as determined by a simple convergence criterion of $|\Delta T| \leq 10^{-8}$, where $|\Delta T|$ was computed only at $x = 0.1\,m$. If greater accuracy or computational efficiency is desired, a more elegant convergence criterion should be developed. The thermal conductivity in each element was determined by identifying the temperature at the midpoint of the element from the previous iteration. As shown alongside the point- and distributed-force boundary conditions in Figure 5.4, the left side of the bar has a fixed temperature of 273 K, while the right side is subjected to an applied heat flux of $115{\times}10^3\ W/m^2$, which raises the temperature of the right-most element to about 1500 K. Figure 5.5 shows the resulting temperature distribution over the axial bar, solved with 1000 linear elements.

Similar to the thermal conductivity, the elastic modulus in each element was determined by identifying the temperature at the midpoint of the element and plugging it into the elastic

modulus function, thus creating a piecewise constant function for elastic modulus, which is plotted against the left axis in Figure 5.5. The solution to this 1D FEM problem is plotted against the 1500°C uniformly-distributed temperature solution in Figure 5.6. As expected, the applied tip heat flux case shows much lower elongation, as more of the bar retains its low-temperature stiffness. This 1D FEM implementation of the elastic modulus and thermal conductivity functions does not provide a novel result, but proves that they can be effectively implemented within the FEM and eventually the MPM.

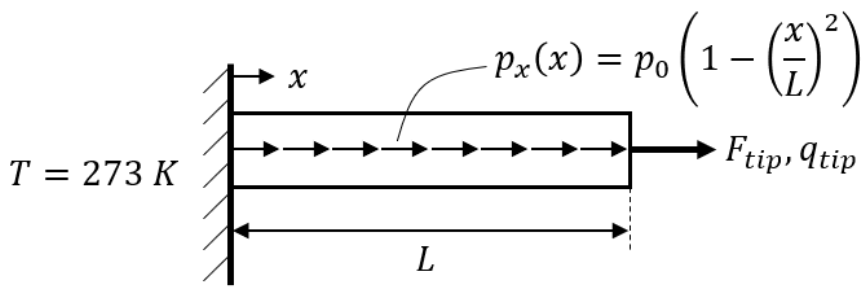

Figure 5.4: Load configuration for 1D FEM problem with applied heat flux and thermal boundary

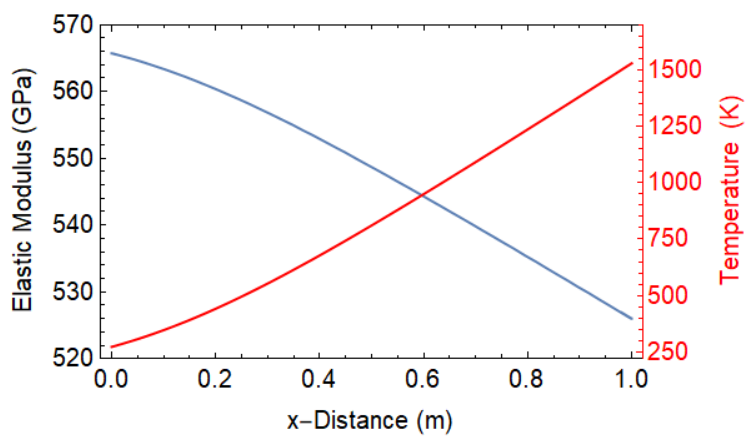

Figure 5.5: Temperature and Elastic Modulus distributions for 1D FEM solution with 1000 linear elements

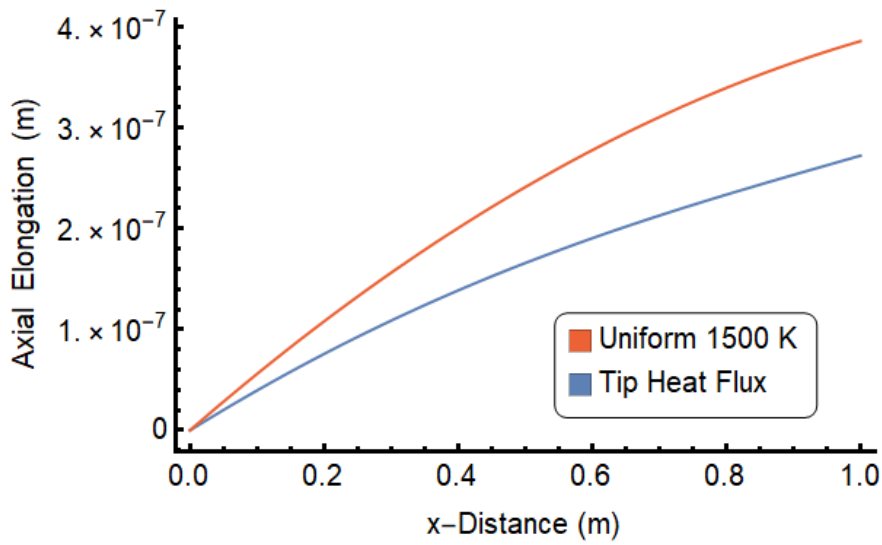

Figure 5.6: Elongation for the 1D FEM problem with an applied heat flux boundary condition compared against the uniform temperature solution

5.2 2D Plane Strain Simulations

With the FEM solution providing an understanding of the material response under simple 1D conditions, the next step was to implement the temperature-dependent material property functions using a better representation of the porous TiB_2 material system. Due to the advantages over FEM discussed in Chapter 4, the MPM code developed by Stefan Povolny was used for these simulations [42]. In this section, the hexagonal RVE and the mechanical and thermal boundary conditions applied to it are introduced. Then the results of room- and elevated-temperature simulations are discussed with emphasis on characterizing the thermomechanical response in the unoxidized state. This provides a useful baseline for assessing the response with oxidation effects present.

5.2.1 Hexagonal Representative Volume Element

A 2D hexagonal representative volume element (RVE) was selected as the domain over which to compute the effective properties of a porous UHTC. Commonly used for modeling carbon nanotube composites [43], the hexagonal RVE was selected because it is very close to transversely isotropic, corresponding explicitly to modeling the plane of isotropy. Hexagonal RVEs with volume fractions of 10%, 40%, and 70% macroporosity were selected for simulation, as shown in Figure 5.7. This range of porosity allows for the investigation of bulk vs geometric effects on response behavior, between which there is a known difference for porous materials [44]. To model the TiB_2 foam investigated by Povolny et al., pores across all three volume fractions have a radius of $r = 50\,\mu m$, which implies that the length-scale interpretation of the RVE is dependent on its level of macroporosity. In addition to the macroporosity, the input properties include 30% microporosity via rule of mixtures with air. This approach was shown by Povolny et al. to overpredict the effective properties significantly, but calibration of the input properties can not yet be performed due to lack of experimental data on oxidized UHTCs.

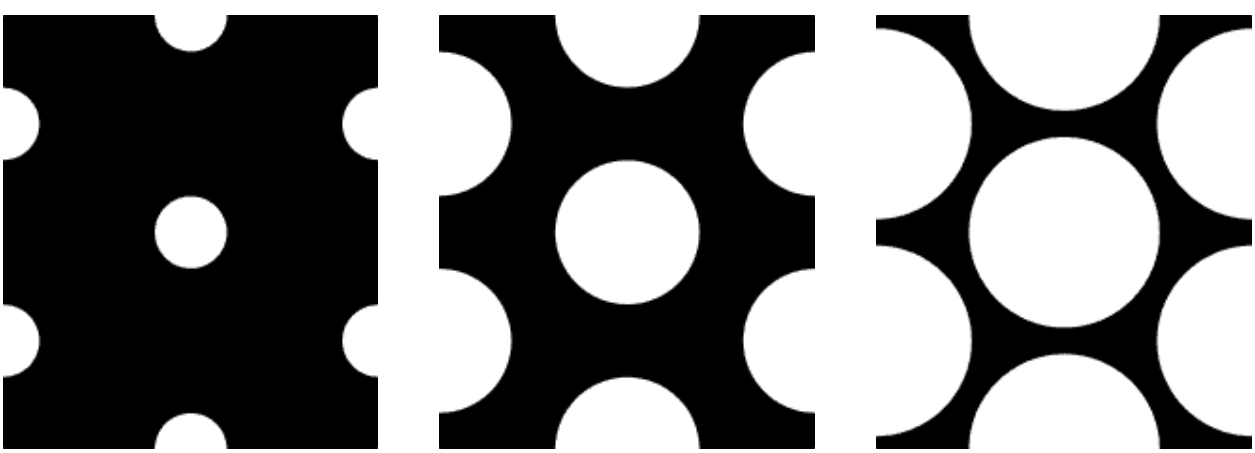

(a) 10% porosity (b) 40% porosity (c) 70% porosity

Figure 5.7: Hexagonal RVEs containing varying levels of macroporosity to represent TiB_2 foam

5.2.2 Simulation Boundary Conditions

The boundary conditions applied to the RVEs are shown in Figure 5.8 for room temperature and elevated temperature simulations. The homogeneous plane strain boundary conditions applied to the RVE correspond to a constrained uniaxial compression test, the value of which lies in being able to determine C_{11}^{eff} and C_{12}^{eff} directly. One key difference in the simulations is that the lateral and out-of-plane constraints on the RVE induce additional transverse stresses that would not be present in the unconstrained uniaxial compression tests. During the unconstrained tests, only a normal stress in the loading direction will develop. Another difference is that experimental unconstrained testing would be performed at a larger scale with less uniform porosity. Given that experimental data has not yet been generated for oxidized UHTCs with multiscale porosity, we are unable to compare against experimental results and it is therefore reasonable to proceed with these essential boundary conditions.

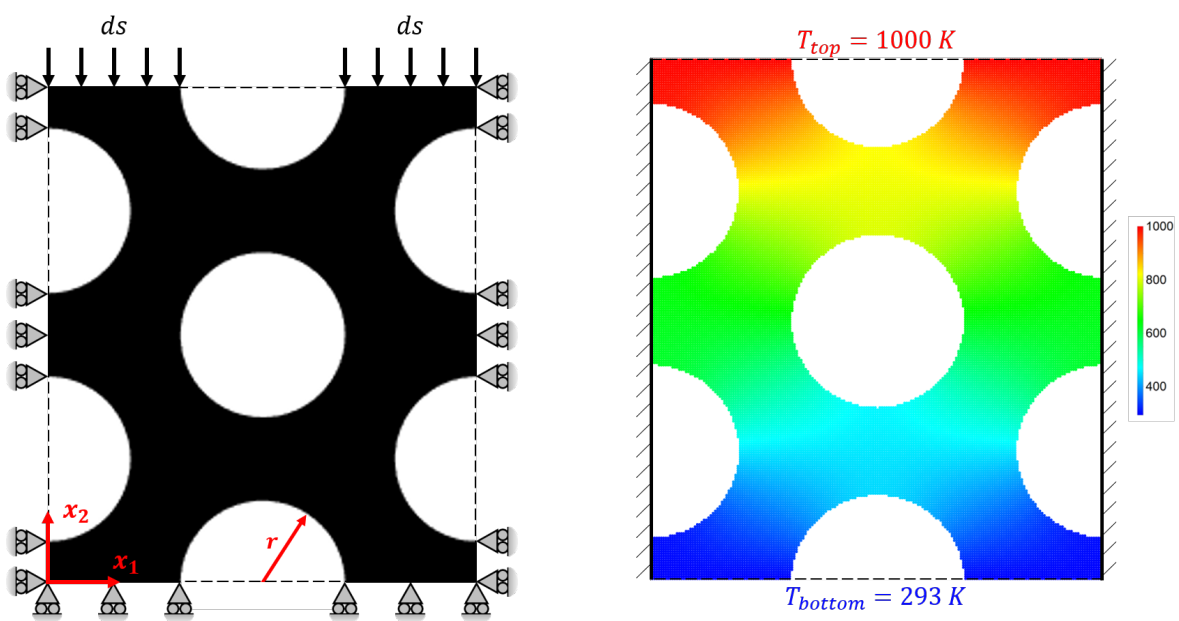

(a) Mechanical Boundary Conditions (b) Thermal Boundary Conditions

Figure 5.8: Mechanical (a) and thermal (b) boundary conditions applied to the hexagonal RVE (40% macroporosity shown). Dashed lines indicate the RVE domain. The boundary conditions are applied directly to the background grid (not shown).

The first series of simulations were performed at room temperature, while later simulations were subjected to two sets of thermal boundary conditions, the first of which being a 15 K/s ramp on the top boundary that reaches 1000 K at the end of the simulation. The second applied thermal load is a 42 K/s ramp on the top surface that reaches 1000 K when $t = t_f/3$, holds constant at 1000 K until $t = 2 \cdot t_f/3$, then decreases linearly back to room temperature. For all simulations on the hexagonal RVEs, the final time step of the simulation is $t_f = 50\ s$. For both sets of thermal boundary conditions, the bottom boundary is fixed at room temperature and the sides are thermally insulated, which results in the thermal gradient shown in Figure 5.8(b). Note that this thermal gradient evolves throughout the simulation and the gradient shown is a snapshot of the domain when the top boundary reaches 1000 K. Profiles of the applied thermal loads are shown in Figure 5.9.

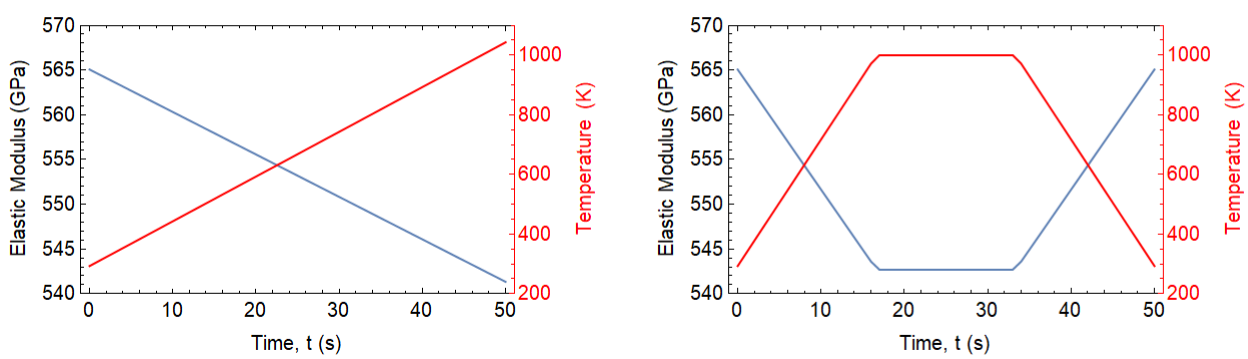

(a) Ramped Thermal Load (b) Cyclic Thermal Load

Figure 5.9: Profile of the thermal loads applied to the top boundary of the RVE. The red curve shows the temperature while the variation of elastic modulus is shown in the blue curve to provide context.

The temperature ramp of 15 K/s is reasonable for a hypersonic flight vehicle upon which this material system may be employed [45], but the 42 K/s ramp is physically unrealistic. The intent of applying this increased heating rate was to capture the difference in the material response when subjected to a heating and cooling cycle rather than heating alone. Thus, the

physical accuracy relative to the hypersonic flight environment is not critical. Furthermore, because this MPM implementation is quasi-static, the time-scale interpretation of the applied thermal load is only of importance if the heating rate must correspond to a certain strain rate, such as in modeling the flight profile of a hypersonic vehicle. In this case, the heating and strain rates were chosen independently to lower the computational cost while exploring the effects of thermal expansion. It is also assumed that the short high-temperature exposure duration does not allow enough time for oxidation to occur.

5.3 Compressive Loading of Hexagonal RVEs

The volume-averaged stress- and damage-strain responses of the hexagonal RVEs are shown in Figures 5.10 and 5.11 up to an applied compressive strain of 30% in 0.6% steps at room temperature. To establish a baseline for interpreting these results, the stress- and damage-strain curves for an RVE with 0% macroporosity (30% microporosity) are shown. As expected due to the tensile-only damage model being used, this RVE shows no damage accumulation, thus the stress increases in proportion to the applied strain. When macroporosity is introduced, the RVE is opened up to tension and the resulting damage ultimately leads to material failure, as shown by the compressive stress peaks. In the stress-strain curves shown, the stress begins to rise after these peaks but this is only a byproduct of the lateral constraints. As further strain is applied, the material is compressed into a region of decreasing volume, thus compacting the material and causing an increase in stress. This phenomenon would not exist in the mechanical tests that correspond to unconstrained compression.

In order to compare the effects of macroporosity (and later oxidation) on the mechanical response of multiscale porous TiB_2, four metrics are considered. The first metric is the effective elastic modulus, which is computed after the first strain step using Equation 4.16.

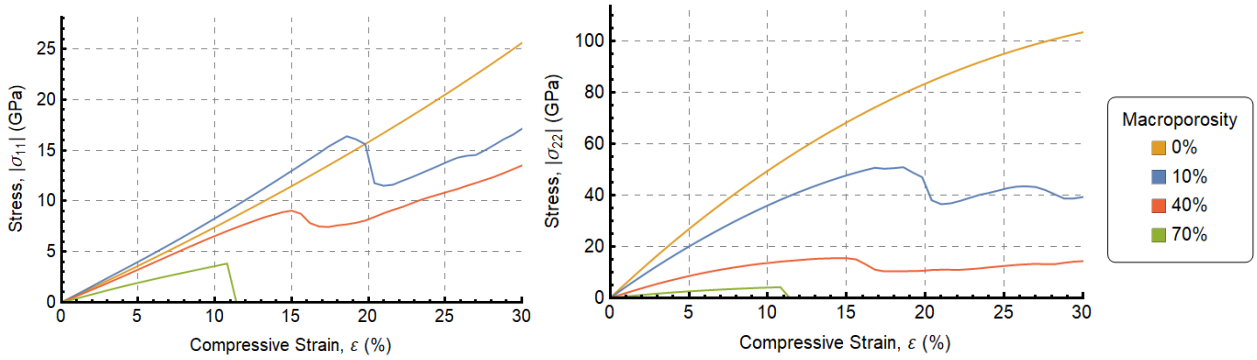

(a) Stress 11-Component (b) Stress 22-Component

Figure 5.10: Stress vs. compressive strain curves for hexagonal RVEs with 10%, 40%, and 70% macroporosity at room temperature. The 0% porosity curve is provided to establish a baseline for interpreting the mechanical response.

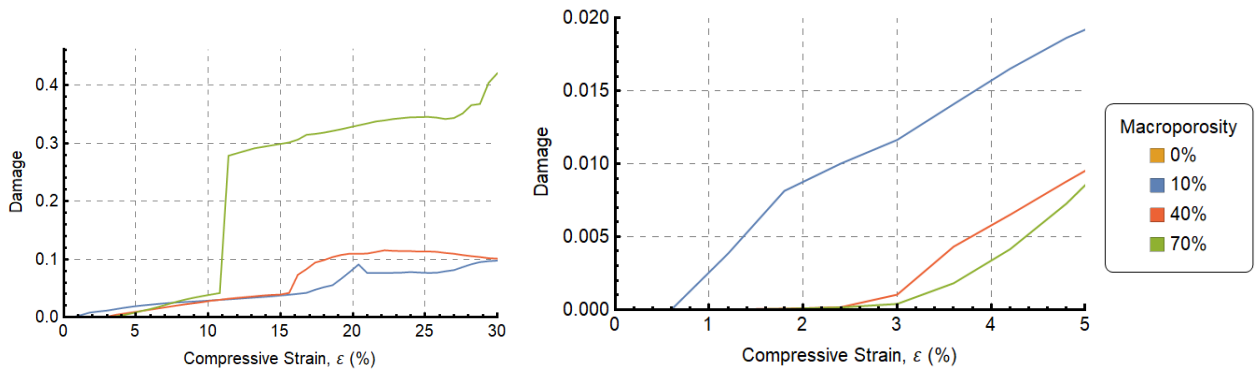

(a) Full Response (b) Initial Response

Figure 5.11: Damage vs. compressive strain curves for hexagonal RVEs with 10%, 40%, and 70% macroporosity at room temperature. The 0% porosity curve is provided to establish a baseline for interpreting the mechanical response.

For the hexagonal RVE, damage can be thought of as occurring at both the microscale and macroscale. At the microscale, the material comprising the struts of the RVE begin to damage at very low strain levels, as defined by the damage law and failure strain inputs. The strain value at which damage first occurs, called the *micro-damage initiation strain*, is the second metric used to compare the simulation results. While this metric is dependent on the damage initiation strain for the material, the values obtained for each macroporous RVE will be unique due to geometric effects. For oxidized RVEs, it will also be dependent on the

relative volume fractions of the phases. Note that simulations to determine the micro-damage initiation strain employed strain steps of 0.06% to achieve higher resolution.

At the macroscale, damage accumulates in the material until catastrophic failure occurs and the RVE is unable to carry additional load. It is of interest to know at what strain value this failure occurs, so we define the *macro-damage initiation strain* as the third metric. This strain value is measured by identifying the point at which the tangent modulus of σ_{22} first becomes negative. The fourth and final metric is the *compressive strength*, which is taken as the value of σ_{22} at the macro-damage initiation strain. While the stress may plateau or further increase beyond this point due to the homogeneous boundary conditions, the macro-damage initiation strain and corresponding compressive strength metrics heuristically quantify the load carrying capability of the material. All four metrics are presented in Table 5.1 for the room temperature simulations.

Table 5.1: Elastic and damage properties of hexagonal RVE snapshots with various levels of macroporosity at room temperature

Macroporosity (%)	Effective Elastic Modulus (GPa)	Micro-Damage Initiation Strain (%)	Macro-Damage Initiation Strain (%)	Compressive Strength (MPa)
10	419	0.3	16.8	50,748
40	167	0.6	14.4	15,562
70	31.6	0.78	10.8	4,224.7

From these data, it is apparent that these metrics vary greatly with macroporosity. Given an input elastic modulus of 565 GPa for TiB_2, the introduction of porosity leads to a decrease in effective stiffness ranging from 26% at 10% macroporosity to 94% with 70% macroporosity. This wide range of stiffness values can be attributed to the transition from bulk response to geometric response, which is confirmed by the increase micro-damage initiation strain. As a higher volume fraction of the RVE is opened up, the struts are able to bend and comply with the applied load, therefore increasing the strain at which damage first occurs,

as illustrated by the initial damage response in Figure 5.11(b). This is countered by the fact that these compliant RVEs have a lower overall tolerance for damage due to strut buckling, leading to the macro-damage initiation strain decreasing with an increase in macroporosity. This is apparent in Figure 5.11(a), wherein the volume-averaged damage in the 70% RVE increases to 0.3 after it reaches the macro-damage initiation strain, while the other two RVEs experience mild damage increases as they approach failure.

Consistent with the decrease in macro-damage initiation strain, the compressive strength is reduced for RVEs with higher porosity, though the magnitude of these values are not reasonable compared to the literature data. Noting that the published compressive strength for TiB_2 at room temperature is just 1,800 MPa [32], simulations for even the highest amount of porosity overpredict the strength by 134%. This highlights the affects of the lateral constraints, which induce a large degree of transverse stress that results in an overestimation of the strength capabilities of the material. While compressive stresses will be computed for the remaining simulations for relative comparison, their absolute magnitudes should not be interpreted as true representations of the unconstrained response.

A counter-intuitive observation was also made about the stress-strain response of the RVEs compared to the 0% porosity baseline. The lateral stress component, σ_{11}, for 10% porosity is shown to exceed the magnitude of this same component for 0% macroporosity. This is contrary to the established decreasing trend, so further investigation was needed. By plotting the principal stress contours at the macro-damage initiation strain for each RVE in Figure 5.12, we observe that stress concentrations occur along the left and right sides of the pores. For the 10% macroporosity RVE, the magnitude of these concentrations is at least 125 GPa, which leads to a higher volume averaged stress for the RVE compared to the 0% macroporosity RVE. The magnitude of the concentrations decrease significantly in the 40% and 70% RVEs, which is consistent with their shallower stress-strain responses.

Also shown in the 2nd principal stress contours in Figure 5.12 are the force chains where a majority of the load is carried by the RVE. These chains become very thin as the level of porosity is increased, leading to an overall lower load carrying capability that manifests itself in the decreasing values of macro-damage initiation strain and compressive strength. This is confirmed by observing the damage field contour plots.

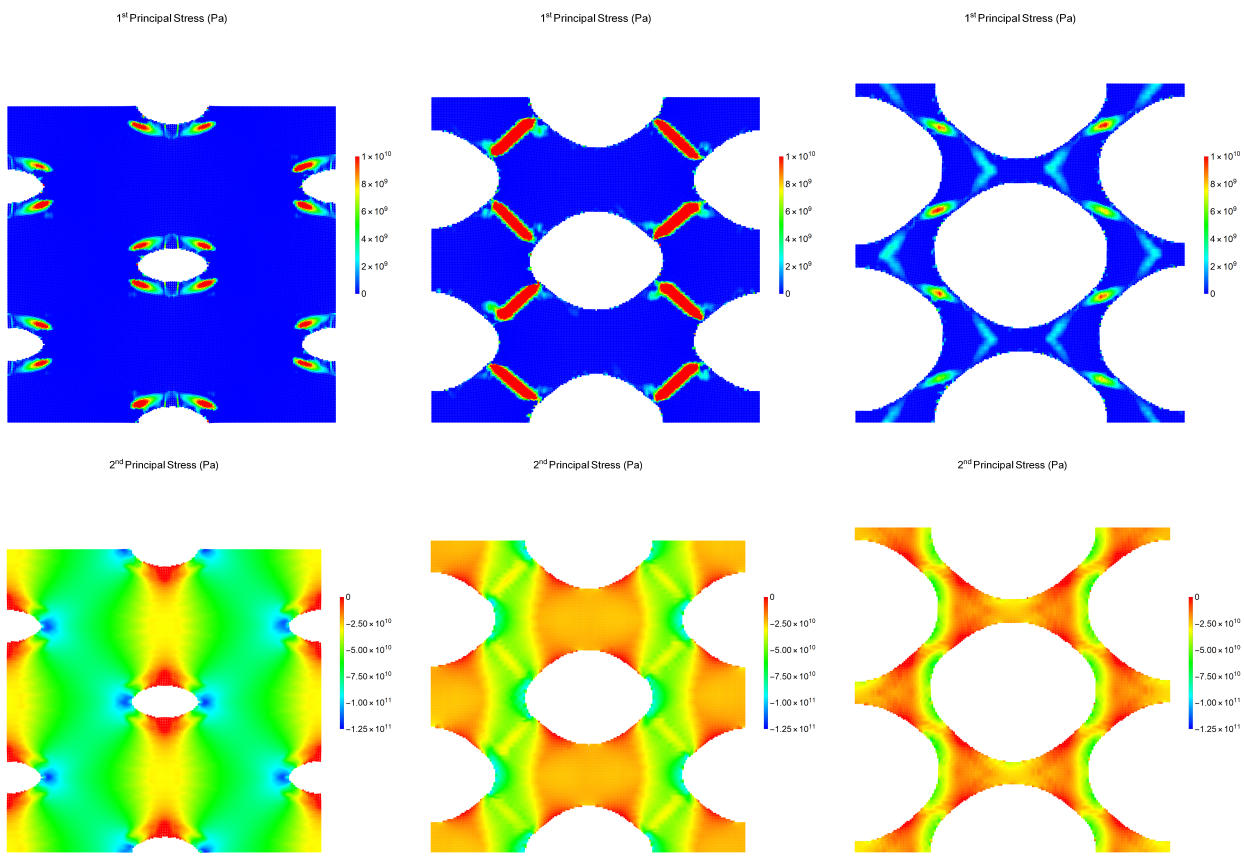

(a) 10% porosity (b) 40% porosity (c) 70% porosity

Figure 5.12: Contour plots of the principal stress fields at the corresponding macro-damage initiation strain of each baseline RVE. Stress contours adjusted to keep stress levels the same color.

To further explore the transition from bulk- to geometric-dominated behavior, the damage field contours for each RVE at three different strain levels have been plotted. Figure 5.13(a) shows the damage fields at the macro-damage initiation strain for each RVE, thus illustrating

where damage occurs immediately before failure. In the 10% macroporosity RVE, damage accumulates at the top and bottom of each pore, but the struts remain undamaged. This response is similar to what may be expected for a simple plate-with-hole RVE, especially considering the compressive stress concentrations shown in Figure 5.12. This indicates that the 10% macroporosity result is dominated by the bulk properties of the material due to the thickness of its struts. In the 40% and 70% macroporosity RVEs, damage instead accumulates in shear bands across the struts, behavior that is reasonable given the approximately 60° orientation of the struts relative to the applied load. These shear bands are oriented at approximately 45° relative to the global coordinate system in the 40% macroporosity RVE, but this orientation changes in the thinner struts of the 70% macroporosity RVE.

Figure 5.13(b) shows the damage fields at one load step beyond the macro-damage initiation strain for each RVE. For this increase in strain, the 10% and 40% macrorporous RVEs show only a slight increase in the overall damage, while the 70% macroporosity RVE fails in a manner consistent with the sharp jump in damage shown in Figure 5.11. This sudden catastrophic failure is caused by weakening of the struts due to damage hot spots on the edges of the pores and the through-thickness shear bands seen in Figure 5.13(a). These damaged regions effectively reduce the stiffness of the struts and cause the buckling shown in Figure 5.13(b). Finally, the damage fields were plotted at 21% applied engineering strain for each RVE in Figure 5.13(c) to show the relative failure behavior. The 10% RVE fails in a brittle fashion through the struts, while the 40% RVE fails along several of the previously identified shear bands.

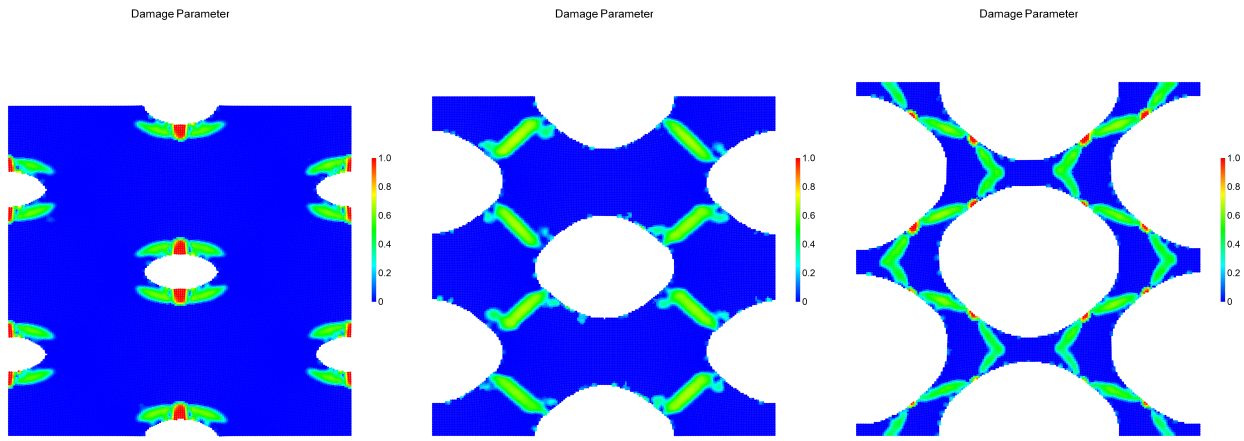

(a) Damage contours at respective macro-damage initiation strains

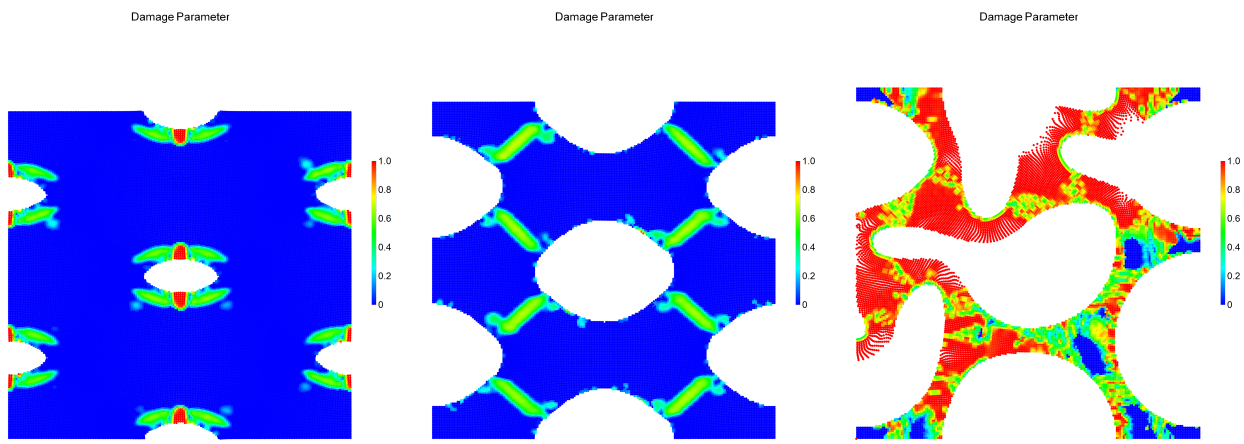

(b) Damage contours after one load step beyond the respective macro-damage initiation strains

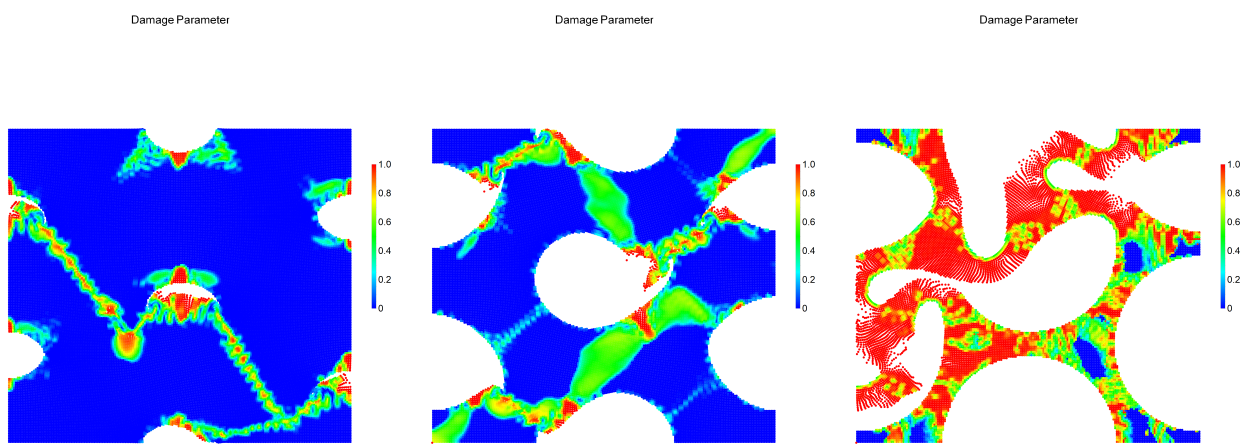

(c) Damage contours at 21% applied compressive engineering strain

Figure 5.13: Damage field contour plots for each RVE showing the response at (a) the corresponding macro-damage initiation strain, (b) one load step beyond the macro-damage initiation strain, and (c) 21% applied engineering strain

5.3.1 Effects of Ramped Thermal Loading

The effects of thermal expansion described in Section 4.1 were introduced by applying the ramped thermal load as defined in Figure 5.9(a) to the hexagonal RVEs of varying porosity. To isolate the stress due to thermal expansion, simulations were performed wherein the RVE was fully constrained then subjected to the ramped thermal load without any applied engineering strain. The corresponding stress-time curves are shown in Figure 5.14. Both stress components increase proportionally with the thermal load for all RVEs and, as expected for these single-phase RVEs, no damage developed throughout the simulation.

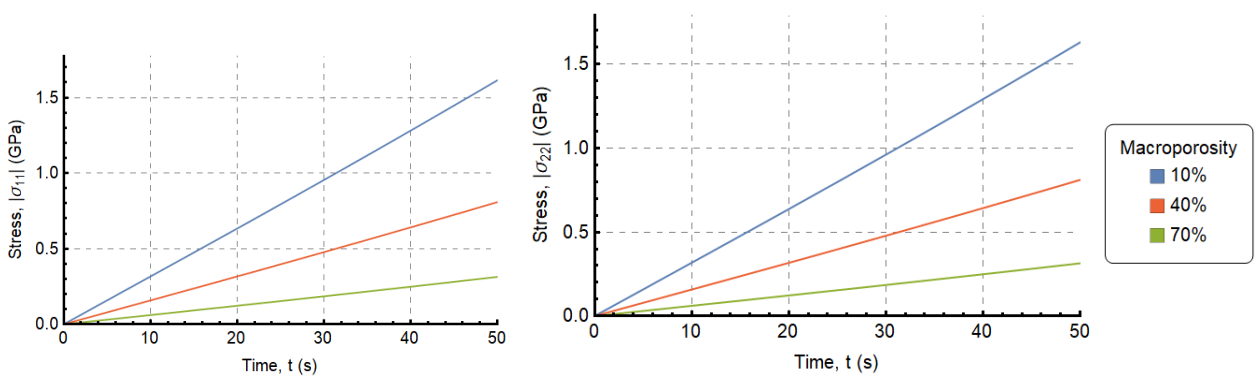

(a) Stress 11-Component (b) Stress 22-Component

Figure 5.14: Compressive stress vs. time for hexagonal RVEs with 10%, 40%, and 70% macroporosity subjected to the ramped applied thermal load and no applied engineering strain.

With this understanding of how the RVEs behave due to constrained thermal expansion, the ramped thermal load was applied to compressive strain simulations. The stress-strain response for these simulations is plotted against the room temperature (RT) simulation response in Figure 5.15. These plots indicate an increase in the magnitude of σ_{11} that is on the order of the thermal stress contribution. For σ_{22}, the thermal expansion takes a smaller role, as the ramped thermal load stress-strain curves are only slightly greater in magnitude than the room temperature curves before failure. The damage-strain curves in Figure 5.16

show that as the RVE is heated and the damage-initiation strain increases according to Equation 5.4, the volume-averaged damage in the RVE is lower than that of the room temperature simulation.

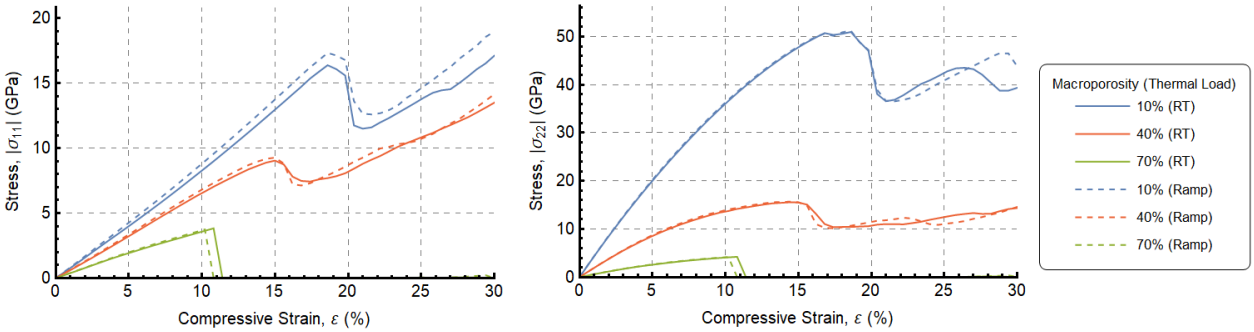

(a) Stress 11-Component (b) Stress 22-Component

Figure 5.15: Stress vs. compressive strain curves for hexagonal RVEs with 10%, 40%, and 70% macroporosity with the ramped applied thermal load

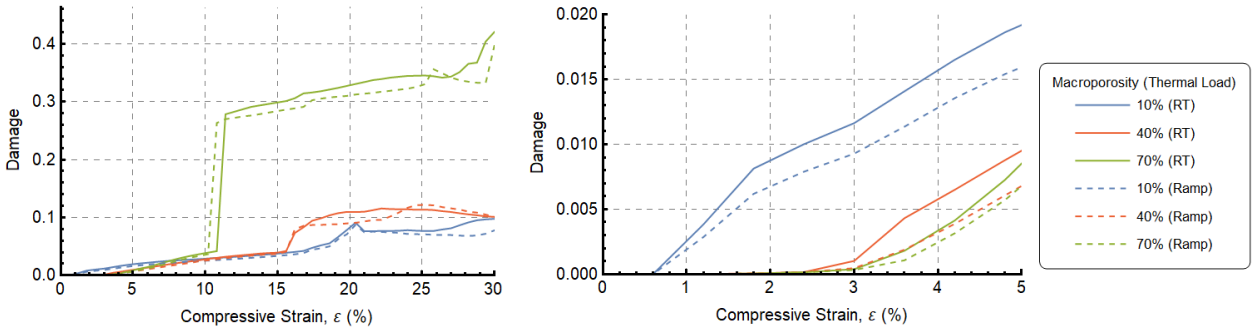

(a) Full Response (b) Initial Response

Figure 5.16: Damage vs. compressive strain curves for hexagonal RVEs with 10%, 40%, and 70% macroporosity with the ramped applied thermal load

To further compare the responses, the elastic and damage metrics for the ramped thermal load simulations are presented in Table 5.2. The apparent effective elastic modulus for the 10% and 40% RVEs increased by 2 GPa and 1 GPa, respectively, which is attributed to the increase in stress due to thermal expansion at the first time step, where the effective stiffness is calculated. Note that the effective elastic modulus is dubbed "apparent" due to the introduction of these thermal stresses. Although the input elastic modulus decreases

gradually with temperature, most of the RVE domain is still at room temperature at the first time step, thus the thermal stress is thought to dominate any small change in elastic modulus at the top of the RVE during the first strain step. The thermal expansion is deemed to have little affect on the stiffness of the 70% RVE because the effective stiffness remains unchanged from the room temperature simulation.

Table 5.2: Elastic and damage properties of hexagonal RVE snapshots with various levels of macroporosity with the ramped applied thermal load

Macroporosity (%)	Effective Elastic Modulus (GPa)	Micro-Damage Initiation Strain (%)	Macro-Damage Initiation Strain (%)	Compressive Strength (MPa)
10	421	0.24	16.8	50,634
40	168	0.54	14.4	15,681
70	31.6	0.72	10.2	4,174.7

The micro-damage initiation strain decreased by 0.6% for all three RVEs. This implies that although the damage initiation strain increases with temperature, the strain due to combined thermomechanical loading dominates in the initial strain steps, when most of the RVE domain is still at room temperature. After the micro-damage initiation strain is reached, the slope of the volume-averaged damage curve is less than that of the room temperature simulation, which leads to higher macro-damage initiation strains except in the case of the 70% RVE. This highly porous RVE begins to fail on the macroscale at 0.6% lower applied strain, thereby highlighting the complexities associated with using temperature dependent properties in conjunction with a thermal gradient. While the damage initiation strain increases in the upper third of the RVE throughout the simulation, so does the thermal expansion coefficient, thus leading to higher thermal stresses. Simultaneously, the stiffness in that region is reduced.

This is confirmed by plotting the temperature and damage fields at the macro-damage initiation strain, as shown in Figure 5.17. Comparing the damage contour to Figure 5.13(a),

the RVE subjected to ramped thermal loading shows similar behavior overall, but larger damage hot spots are present near the warmer top boundary, while the damage intensity is reduced near the cooler bottom boundary. The lower macro-damage initiation strain is the result of the stiffness reduction leading to strut buckling at a lower strain level coupled with increasing thermal stresses due to the higher thermal expansion coefficient, despite the material being capable of withstanding greater strains before damage initiation.

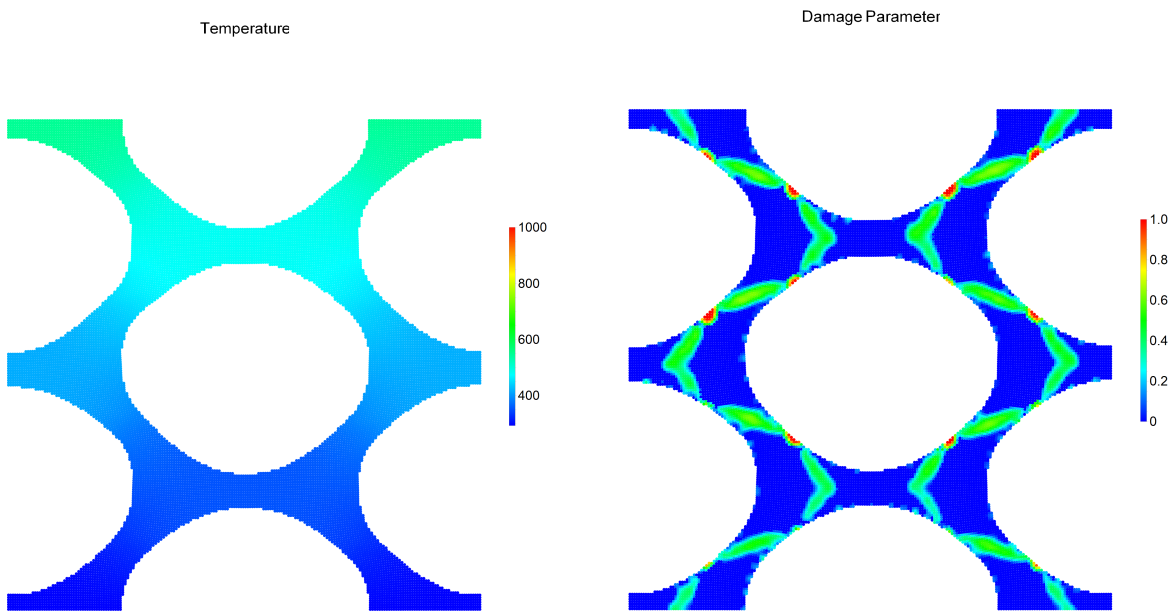

Figure 5.17: Contour plots of temperature and damage parameter fields for the hexagonal RVE with 70% macroporosity subjected to ramped thermal loading and 10.2% compressive strain. Snapshots represent the field parameters when $t = 18s$.

The compressive strength for the 10% and 70% macroporosity RVEs decreased by 0.2% and 1.2%, respectively, due to the applied thermal load. For the 10% RVE, this can be attributed to the thermal expansion having a larger effect on RVEs with less porosity, as was apparent in the effective elastic modulus results. The lower compressive strength of the 70% RVE is due to its lower macro-damage initiation strain value. Figure 5.16(a) shows that the damage before and after failure for the 40% RVE is noticeably lower than in the room temperature simulation, which leads to an increase of 0.7% in compressive strength.

This result is reasonable given that the heated regions of the RVE have an increased damage initiation strain. Although the variation in the elastic and damage metrics due to ramped thermal loading is small, the mechanics behind these variances indicate the complexity of the thermomechanical modeling being performed.

5.3.2 Effects of Cyclic Thermal Loading

To assess the effects of thermal expansion due to a heating and cooling cycle, the cyclic thermal load in Figure 5.9(b) was applied to the hexagonal RVEs. As with the ramped thermal load, simulations were performed on fully constrained RVEs subjected to the cyclic thermal profile without any applied engineering strain. The corresponding stress-time curves are shown in Figure 5.18. Both stress components increase proportionally with the thermal load for all RVEs, plateau when the temperature reaches 1000 K, then return to zero as the top boundary is cooled. No damage developed at low strain levels, but a very small degree of damage, roughly 5×10^{-6}, accumulated in the 10% macroporosity RVE near the end of the simulation. This is discussed in further detail within Appendix A, but was ultimately deemed numerical noise.

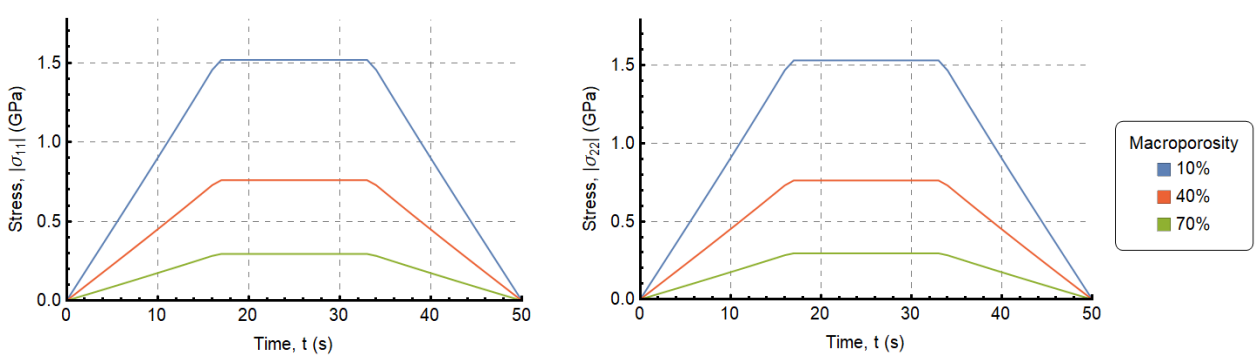

(a) Stress 11-Component (b) Stress 22-Component

Figure 5.18: Compressive stress vs. time for hexagonal RVEs with 10%, 40%, and 70% macroporosity subjected to the cyclic applied thermal load and no applied engineering strain.

With this understanding of how the RVEs behave due to constrained thermal expansion under cyclic thermal loading, thermomechanical simulations were performed. The stress-strain response is plotted against the room temperature and ramped thermal load responses in Figure 5.19. The stress-strain behavior could be described as an amplification of the mechanical response due to the ramped thermal load. Although the constitutive law is not rate dependent, the small increase in temperature at the first time step causes an increase in thermal stress due to the increasing thermal expansion coefficient within the regions of elevated temperature. The damage-strain curves in Figure 5.20 show that the application of cyclic thermal loading causes earlier failure in RVEs with 40% and 70% macroporosity.

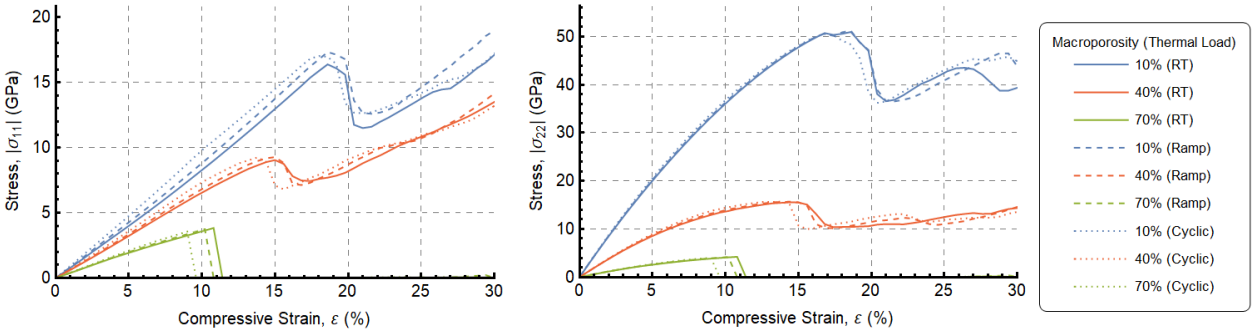

(a) Stress 11-Component (b) Stress 22-Component

Figure 5.19: Stress vs. compressive strain curves for hexagonal RVEs with 10%, 40%, and 70% macroporosity with the cyclic applied thermal load

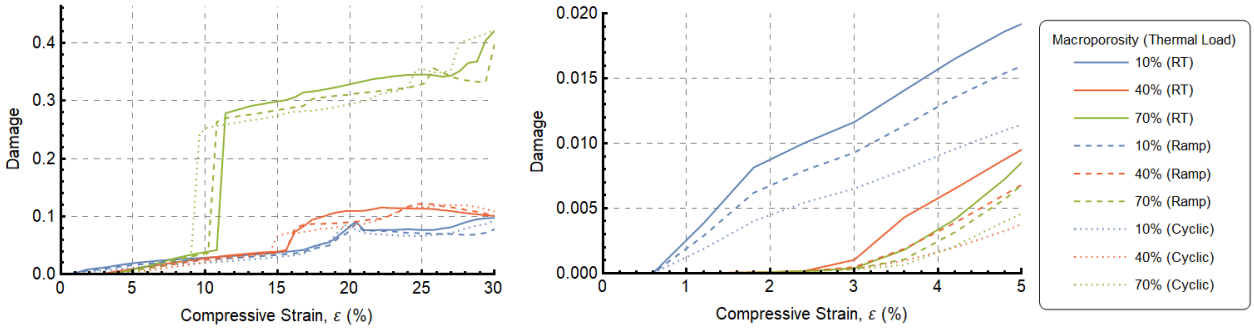

(a) Full Response (b) Initial Response

Figure 5.20: Damage vs. compressive strain curves for hexagonal RVEs with 10%, 40%, and 70% macroporosity with the cyclic applied thermal load

The elastic and damage metrics for the cyclic thermal load simulations are presented in Table 5.3. Compared to the ramped thermomechanical loading simulations, the apparent effective elastic modulus for the 10% and 40% RVEs increased by 4 GPa and 1 GPa, respectively, which is attributed to the higher temperature at the first time step leading to an increase in thermal stress that dominates over the slightly decreased elastic modulus at the top of the RVE. This increased heating rate has a minimal impact on the effective elastic modulus of the 70% RVE, which increased by just 0.1 GPa.

Table 5.3: Elastic and damage properties of hexagonal RVE snapshots with various levels of macroporosity with the cyclic applied thermal load

Macroporosity (%)	Effective Elastic Modulus (GPa)	Micro-Damage Initiation Strain (%)	Macro-Damage Initiation Strain (%)	Compressive Strength (MPa)
10	425	0.24	16.8	50,542
40	169	0.48	13.8	15,715
70	31.7	0.66	9.0	4,048.3

The micro-damage initiation strain decreased by 0.6% and 0.12% relative to the ramped thermal load simulations for the 40% and 70% macroporosity RVEs, respectively. This further confirms that the strain due to combined thermomechanical loading dominates in the initial strain steps, when most of the RVE domain is still at room temperature. After the micro-damage initiation strain is reached for all three RVEs, the slope of the volume-averaged damage curve is less than that of the ramped thermal load simulations, which leads to a higher macro-damage initiation strain for the 10% RVE, but not the 40% and 70% RVEs. For the 70% RVE, this is attributed to the stiffness reduction in the upper region of the RVE leading to strut buckling at lower strain levels and the increase in thermal stresses due to a higher thermal expansion coefficient.

Since shear, rather than buckling, is the primary failure mode for the 40% RVE as shown in 5.13(c), the increased temperature at the first time step is expected to have a different

effect compared to the 70% RVE. Contour plots for the temperature and damage fields just after the macro-damage initiation strain is reached and failure occurs are shown in Figure 5.21. It is inferred through the temperature plot that the damage initiation strain in the upper region is greater than in the lower region. When coupled with the increased thermal stresses present in the upper region, we see that the RVE transitions from failing in the upper and lower struts to failing only in the lower two struts. Therefore, it makes sense that the macro-damage initiation strain is lower than in the ramped thermal load case for the 40% RVE.

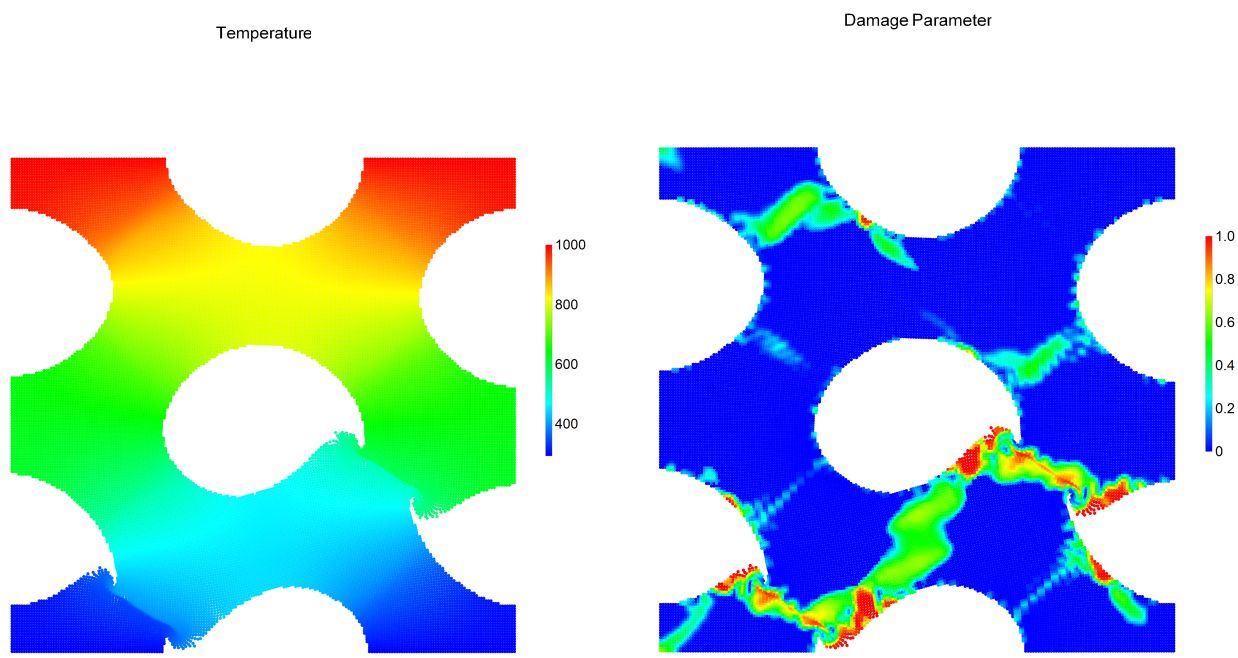

Figure 5.21: Contour plots of temperature and damage parameter fields for the hexagonal RVE with 40% macroporosity subjected to ramped thermal loading and 15% compressive strain. Snapshots represent the field parameters when $t = 26s$.

The compressive strength for the 10% and 70% macroporosity RVEs decreased by 0.2% and 3%, respectively, due to the applied cyclic thermal load. Figure 5.20(a) shows that the damage in the 40% RVE after reaching the macro-damage initiation strain is lower than both the room temperature and ramped thermal load simulations, which leads to an increase of

0.2% in compressive strength. This marginal increase is reasonable given that the heated regions of the RVE have an increased damage initiation strain and it occurs at a slightly lower strain value than in the previous simulations.

5.3.3 Compressive Loading Takeaways

Compressive and thermal loading of the unoxidized hexagonal RVEs has established a baseline for interpreting the behavior of these same RVEs after being oxidized to varying degrees. The room temperature simulations allowed for the effects of macroporosity to be identified, namely the transition from bulk- to geometric-based response behavior. It was concluded that increasing the porosity of the RVE reduces the elastic modulus, macro-damage initiation strain, and compressive strength of the RVE, but the additional bending allowed by the geometric configuration of a highly porous RVE delays damage initiation slightly.

The effects of ramped and cyclic applied thermal loads were then studied for constrained RVEs with no mechanical load, as well as for RVEs subjected to 30% applied compressive strains. Bar charts showing the elastic and damage metrics for each thermal load are shown in Figure 5.22. It was shown that temperature dependencies of the elastic modulus, damage initiation strain, and thermal expansion coefficient, combined with the thermal gradient across the RVE, leads to a complex response that affects RVEs of varying porosities in different ways. In general, the largest affect of increasing the heating rate was the reduction of the macro-damage initiation strain for the 40% and 70% RVEs.

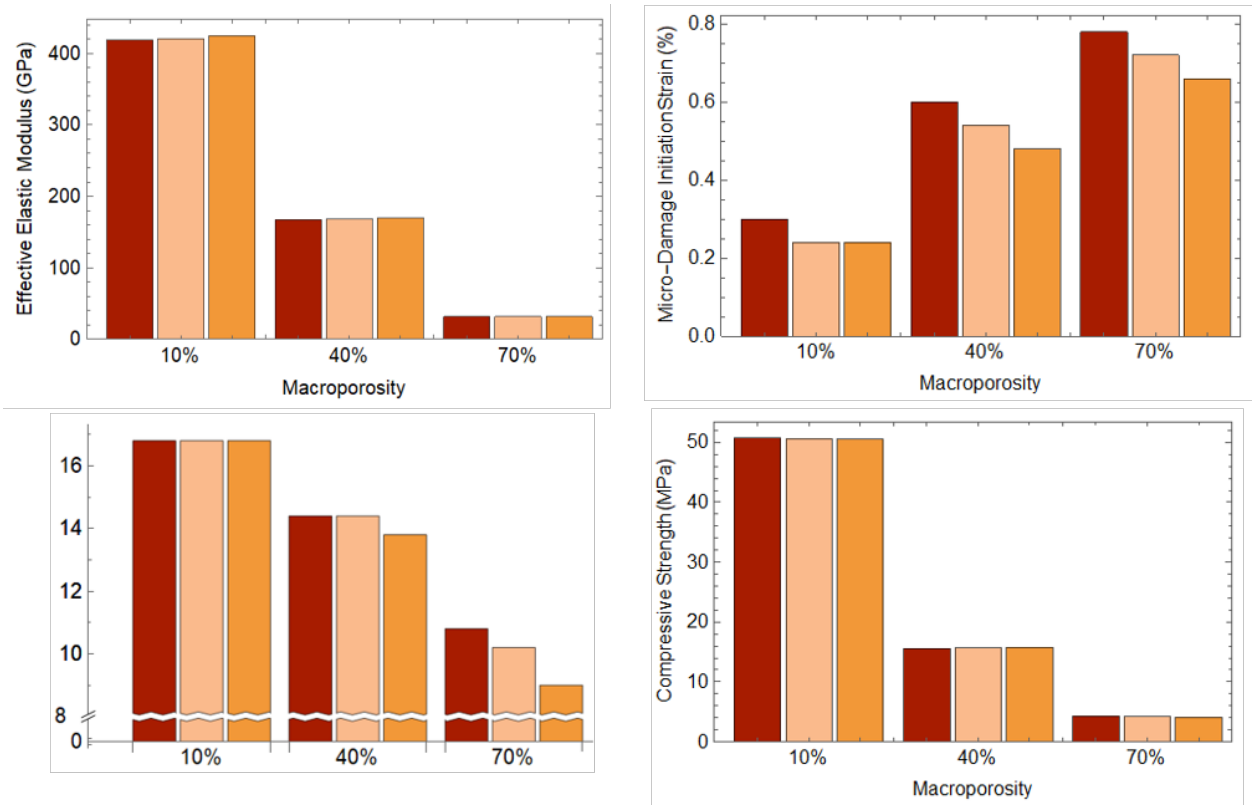

Figure 5.22: Comparison of the elastic and damage metrics for the unoxidized hexagonal RVEs subjected to each applied thermal load.

5.4 Effective Thermal Conductivity of Hexagonal RVEs

In addition to the mechanical response, the effective thermal conductivity was determined for each RVE at room temperature (293 K) and 1000 K via Equation 4.21. The thermal conductivity results are presented in Table 5.4 and show significant dependence on the level of porosity present. The rule of mixtures was then used as a point of comparison in both temperature regimes. Note that both the simulation and rule of mixtures results include 30% microporosity in addition to the specified macroporosity. The table quantitatively shows that the rule of mixtures matches the simulation better at lower percentages of macroporosity, overpredicting the simulation values by 9.6%. The rule of mixtures is less successful in matching the simulation results as macroporosity increases because it overpredicts the ther-

mal conductivity by 28% and 43% for the 40% and 70% macroporosity RVEs, respectively. Despite the worsening approximation for higher porosities, the consistent overprediction implies that the rule of mixtures could serve as a reasonable upper bound for estimating the thermal conductivity of a porous UHTC.

Table 5.4: Effective thermal conductivity of hexagonal RVE snapshots with various levels of macroporosity [Units: $W/(m-K)$]

Macroporosity	Room Temperature		1000 K	
(%)	Simulation	Rule of Mixtures	Simulation	Rule of Mixtures
10	54.7	60.5	45.0	49.8
40	28.7	40.3	23.6	33.2
70	11.5	20.1	9.49	16.7

To investigate the correlation between damage and thermal conductivity, compressive simulations were performed in the two temperature regimes. The resulting variation in thermal conductivity presented in Figure 5.23 shows that there is no discernible difference in the thermal conductivity behavior at 1000 K. For all levels of macroporosity, the magnitude decreases gradually beyond the micro-damage initiation strain, which is to be expected. Due to the strut-shearing failure in the 10% and 40% macroporosity RVEs, there is only a small drop when catastrophic failure occurs. In the 70% RVE, the thermal conductivity drops off sharply when the struts buckle and most of the RVE becomes completely damaged (see Figure 5.13). Towards the end of the applied load, all three RVEs see a slight increase in thermal conductivity as more self-contact occurs. These simulations confirm that the damage model affects thermal conductivity in an intuitive way.

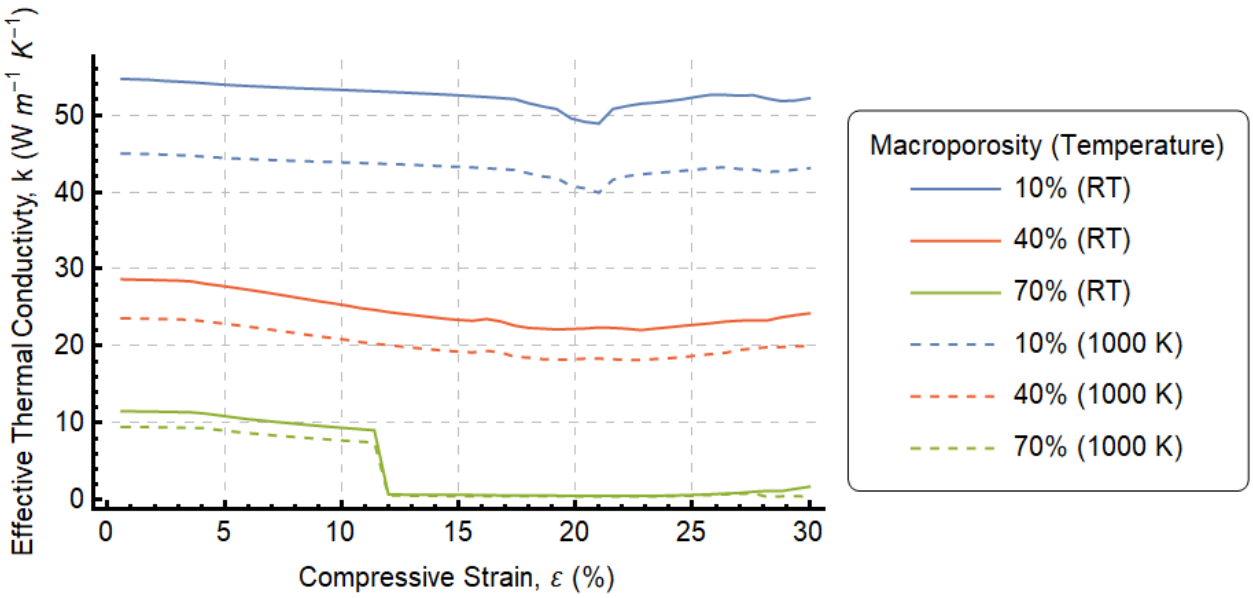

Figure 5.23: Variation in effective thermal conductivity with applied compressive load for varying levels of macroporosity

Chapter 6

Oxidation Model Implementation in the MPM

Due to the theoretical and computational challenges discussed in Chapter 3 that preclude the integration of a diffusion-based oxidation model within the existing MPM code, an alternate technique was used to model oxidation effects in porous ultra-high temperature ceramics. This chapter introduces the concept of snapshot oxidation modeling, wherein simulations are performed on an RVE with a predefined level of oxidation, which does not vary with simulation time. Oxide layers ranging from 5 to 50 µm were applied to the hexagonal RVEs of all three macroporosities, then thermomechanical simulations were performed to determine the oxide layer's impact on the material response. The results of these simulations are discussed, then the snapshot technique is applied to a large porous RVE derived from a CT image of TiB_2 foam.

6.1 Snapshot Oxidation Model

6.1.1 Oxide Layer Thickness

To characterize the effects of oxidation in porous ultra-high temperature ceramics without implementing a diffusion-based oxide layer growth solver within the MPM code, a snapshot

oxidation approach was employed. The general principle of snapshot modeling is that rather than evolving the oxide layer over time, RVEs are prescribed with an oxide layer of a certain thickness based on being exposed to air at high temperatures for a given duration. As shown in Chapter 3, the oxidation products present in the oxide scale may be solid or liquid depending on the exposure temperature, so to bound the problem and eliminate the need for considering the liquid phase, it was assumed that the oxidation for all snapshots would occur at 1200°C. It was shown experimentally by Koh et al. that the liquid B_2O_3 phase is not present at this temperature because B_2O_3 evaporates immediately upon formation at the oxide-substrate interface [29]. Therefore, the oxide layer is composed of a single solid phase, TiO_2, resulting in a final two-phase system with TiB_2 as the substrate material. It was assumed that the 30% microporosity present in the substrate carries over to the oxide phase.

The oxide layers were selected based on the dimensions of the hexagonal RVE with 40% macroporosity, which has has a pore radius of $r = 50$ µm, leading to a bottom edge length of 260.8 µm. To capture the full range of oxidation in this RVE without creating an excessive case log, oxide thicknesses were selected to be $t_{ox} = 5$, 10, 15, 30, 50 µm, where the 50 µm layer fully oxidizes the RVE. Given that the RVE represents an interior region within a larger domain, the oxide layer was only applied to the pore surfaces, which are directly exposed to the oxygen-rich atmosphere. To be consistent across the remaining hexagonal RVEs, the pores were kept at a constant radius of $r = 50$ µm, which corresponds to bottom edge lengths of 521.6 µm and 197.1 µm for 10% and 70% macroporosity RVEs, respectively. Due to this difference in length scales between the RVEs, the oxide layer thicknesses make up different volume fractions of each RVE depending on the fraction of macroporosity. The volume fractions of TiO_2 for oxidized hex snapshots with 10%, 40%, and 70% macroporosity are given in Table 6.1.

Table 6.1: Volume fractions of TiO_2 for oxidized hex snapshots with 10%, 40%, and 70% macroporosity.

Oxide Thickness	Volume Fraction of TiO_2 (%)		
(μm)	10% Macroporosity	40% Macroporosity	70% Macroporosity
5	2.12	8.44	14.8
10	4.41	17.6	26.7
15	6.91	27.6	30.0
30	15.6	57.2	30.0
50	30.0	60.0	30.0

Hexagonal RVE snapshots containing 10%, 40%, and 70% macroporosity with the five oxide layers applied, referred to as *hex snapshots*, are shown in Figures 6.1, 6.2, and 6.3, respectively. Note from Figure 6.3(d) that the 70% macroporosity RVE is fully oxidized when $t_{ox} = 15$ µm. Thus the 70% macroporosity RVEs corresponding to $t_{ox} = 30$ µm and $t_{ox} = 50$ µm provide no additional insight into the oxidation behavior, so simulations were not run for these combinations of macroporosity and oxide layer thickness.

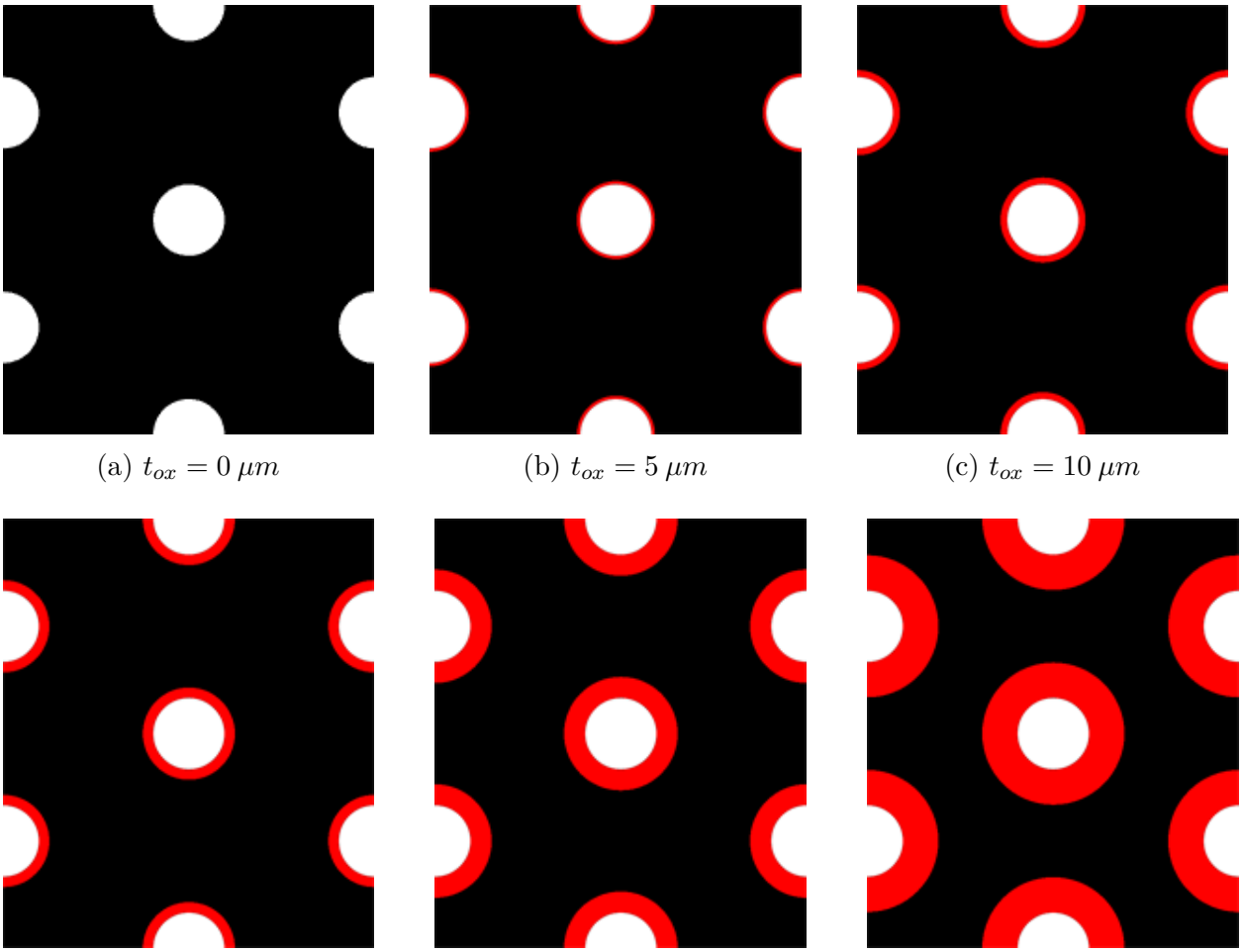

(a) $t_{ox} = 0\ \mu m$ (b) $t_{ox} = 5\ \mu m$ (c) $t_{ox} = 10\ \mu m$

(d) $t_{ox} = 15\ \mu m$ (e) $t_{ox} = 30\ \mu m$ (f) $t_{ox} = 50\ \mu m$

Figure 6.1: Oxidized Hexagonal RVE Snapshots with 10% macroporosity

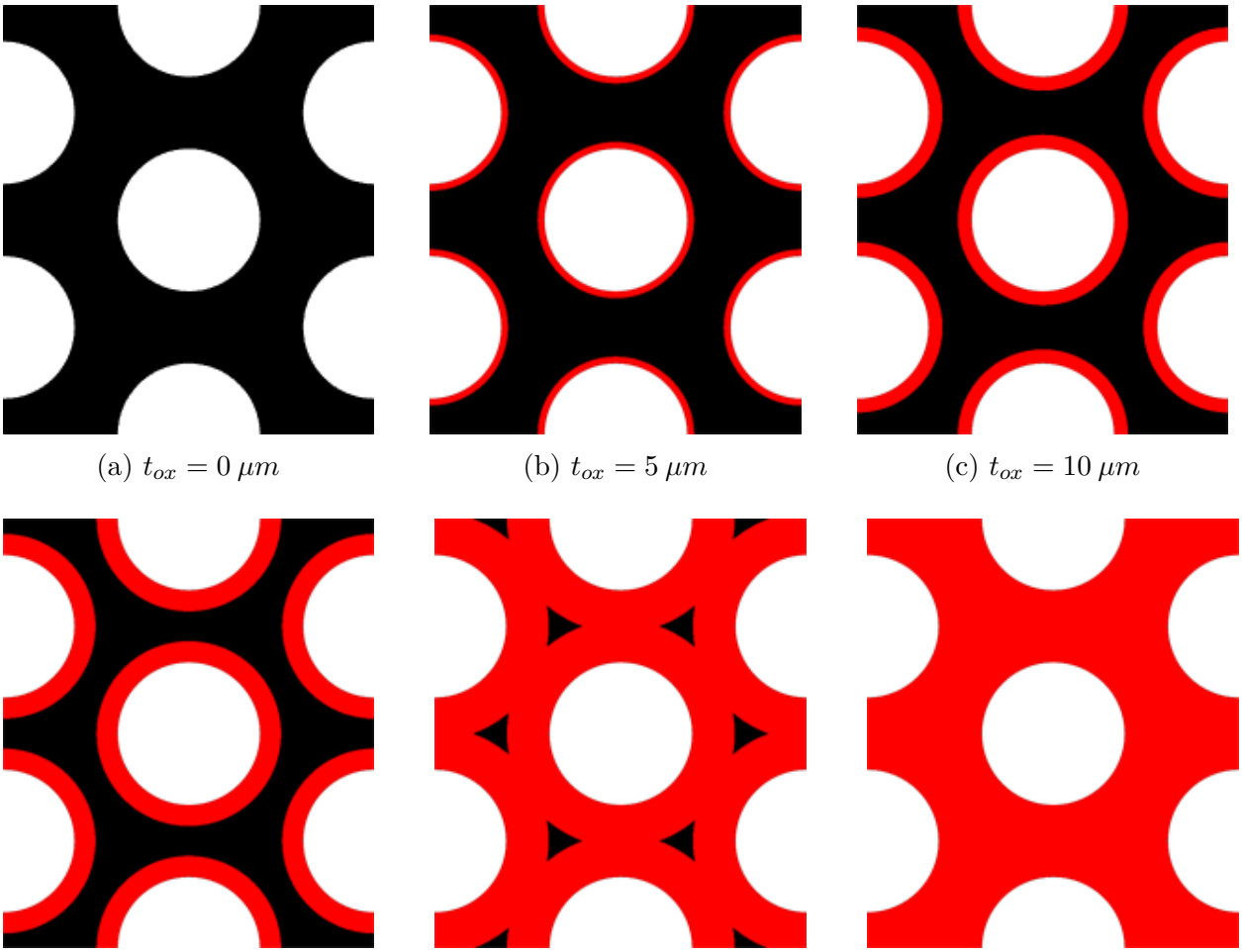

(a) $t_{ox} = 0\ \mu m$ (b) $t_{ox} = 5\ \mu m$ (c) $t_{ox} = 10\ \mu m$

(d) $t_{ox} = 15\ \mu m$ (e) $t_{ox} = 30\ \mu m$ (f) $t_{ox} = 50\ \mu m$

Figure 6.2: Oxidized Hexagonal RVE Snapshots with 40% macroporosity

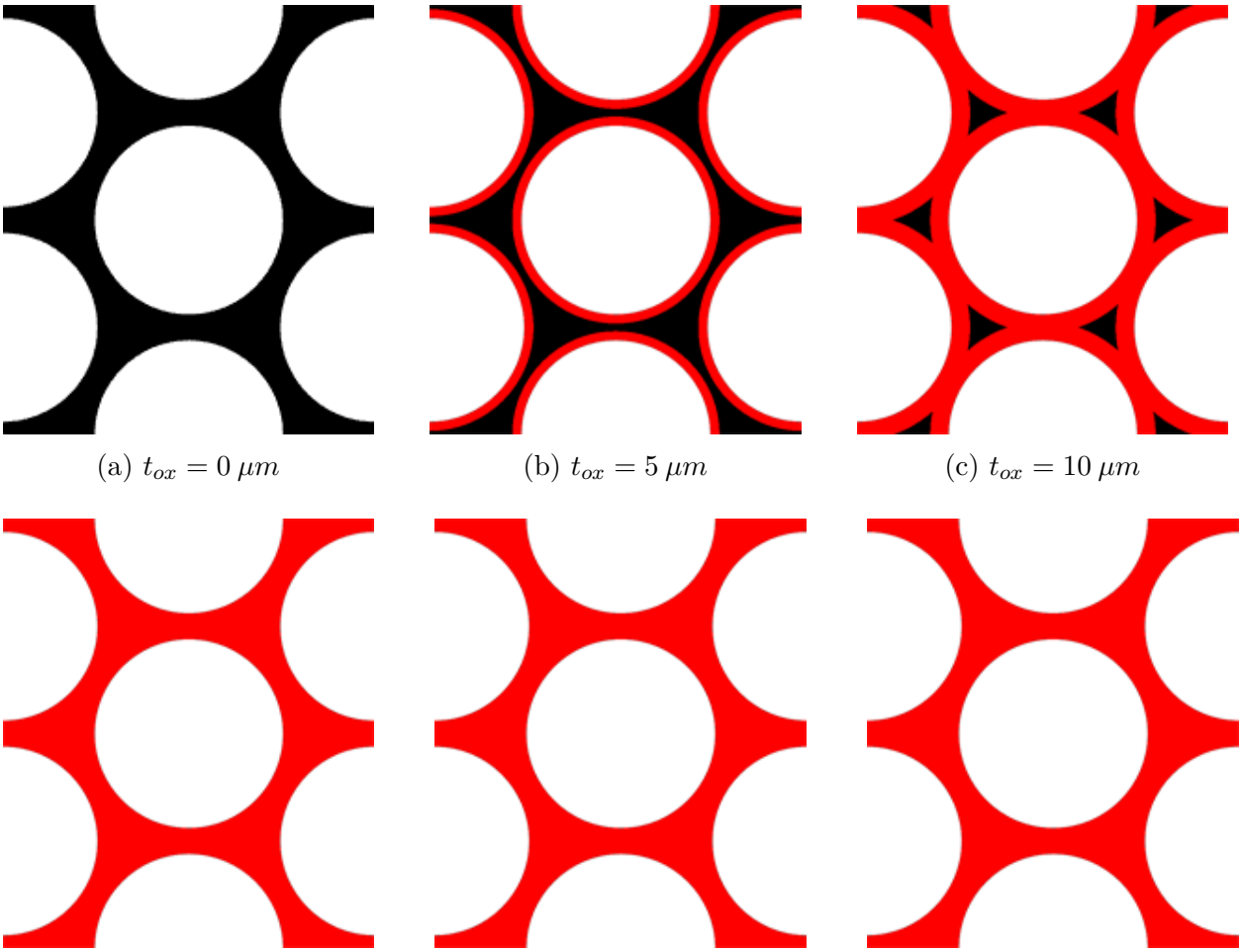

(a) $t_{ox} = 0\ \mu m$ (b) $t_{ox} = 5\ \mu m$ (c) $t_{ox} = 10\ \mu m$

(d) $t_{ox} = 15\ \mu m$ (e) $t_{ox} = 30\ \mu m$ (f) $t_{ox} = 50\ \mu m$

Figure 6.3: Oxidized Hexagonal RVE Snapshots with 70% macroporosity

To correlate the snapshot oxide layer thicknesses to exposure time, an oxide growth model found in the literature was considered. Seeking to match the experimental model from Koh et al. [29], Parthasarathy et al. used their oxide growth model to predict the oxide layer thickness with respect to time for TiB_2 exposed to air at 800 and 1200°C [11]. While their model showed good agreement with experimental data at 800°C, the prediction at 1200°C was less successful. Regardless, the authors concluded that the growth behavior was a reasonable estimate. Numerical data were not provided, so the oxide layer vs. exposure time plot presented in Parthasarathy et al. was sampled at 21 points and fit to the form of Equation 3.4 using *Find Fit* in *Wolfram Mathematica* [40]. The resulting oxide growth curve is shown in Figure 6.4. From this fit, it was determined that the selected oxide thicknesses correspond to exposure times of roughly 1, 4, 8, 32 and 87 minutes for t_{ox} = 5, 10, 15, 30, and 50 µm, respectively.

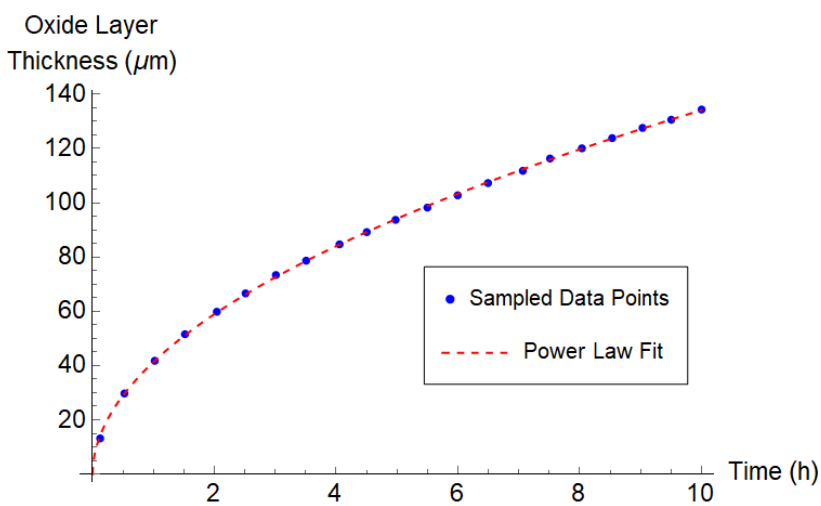

Figure 6.4: Oxide thickness vs. exposure time for TiB_2 exposted to air at 1200°C. Derived from oxidation model developed by Parthasarathy et al. [11]

6.1.2 Two-Phase Temperature-Dependent Material Properties

Modifications to the MPM code were made to accommodate this two-phase material system, specifically in terms of domain discretization and input properties. Formerly, the MPM code accepted binarized images of the desired mesh and converted any white pixels to material points, then constructed the background grid such that each element contained at least two material points. Thus the mesh fineness and number of material points is dependent upon the resolution of the mesh image. This input procedure was modified by instead importing grayscale images to specify the material domain. All white pixels are flagged as TiB_2, while any non-binary (gray) pixels are tagged as TiO_2. This method allows grayscale versions of the hex snapshot images from the previous figures to be used as input files directly. In addition to the modifications required to accept two-phase meshes, an input deck for the second phase material properties was added. The remainder of this subsection discusses the formulation of the TiO_2 input properties.

Physically, the hex snapshot simulations can be thought of as assessing the thermomechanical behavior of a specimen which was oxidized to a certain extent prior to testing. Essentially, the material is oxidized in a furnace, then removed and brought to room temperature before the thermomechanical loads are applied. As such, the RVEs begin with the substrate and oxide phases having the room temperature material properties of TiB_2 and TiO_2, respectively. With the exception of Poisson's ratio, all TiB_2 input properties have temperature dependence as defined in Section 5.1.1. Temperature dependencies for all input properties of TiO_2 were not readily available in the literature, but temperature-dependent functions for the elastic modulus, density, specific heat, and thermal expansion coefficient from room temperature to 1800 K were defined based on data compiled by Isaak et al. [46]. In similar fashion to the properties of TiB_2, *Find Fit* in *Wolfram Mathematica* [40] was used to define the following fitting functions:

$$E = 279.2 - 0.03953T \tag{6.1}$$

$$\rho = 4292 + 0.1342T \tag{6.2}$$

$$C_p = 492.6 + 0.8319T - 5.105 \times 10^{-4}T^2 + 1.186 \times 10^{-7}T^3 \tag{6.3}$$

$$\alpha = 5.874 \times 10^{-6} + 4.064 \times 10^{-8}T - 1.864 \times 10^{-11}T^2 + 4.602 \times 10^{-15}T^3 \tag{6.4}$$

These fits are plotted against their respective data points and the corresponding fits for TiB_2 in Figure 6.5. It should be acknowledged that although a 2nd-order fit of the mass density of TiO_2 would be more accurate than the 1st-order fit used, the linear fit does not depart significantly from the data within the specified temperature range. An observation of high importance for the thermomechanical simulations performed herein is that the thermal expansion coefficient of TiO_2 is notably more sensitive to temperature increases than that of TiB_2. Thus the stresses that develop due to the thermal expansion mismatch are expected to cause an increase in damage throughout the RVEs. Aside from the thermal expansion coefficient, the other oxide phase input properties exhibit similar temperature-dependent behavior to the TiB_2 substrate.

Table 6.2 summarizes the room temperature input property values for each dense, fully sintered material, including those for which temperature-dependent functions could not be developed. These tabulated properties were then modified to have 30% microporosity incorporated via rule of mixtures with air. The damage initiation strain for TiO_2 was determined using Equation 5.3 with the elastic modulus given by Isaak et al. [46] and the tensile strength provided by AZo Materials [47]. The thermal conductivity and Poisson's ratio of TiO_2 were also taken from AZo Materials. The final input parameter was the Weibull modulus, which had a value of 11 for TiB_2 [32]. This statistical parameter was used to form a Weibull

distribution which perturbs $\tilde{\varepsilon_0}$ to capture the variability of defect locations within brittle materials and to reduce mesh-dependence in the results [48]. Based on guidance from Stefan Povolny, it was assumed that TiO_2 maintained the same Weibull modulus as TiB_2.

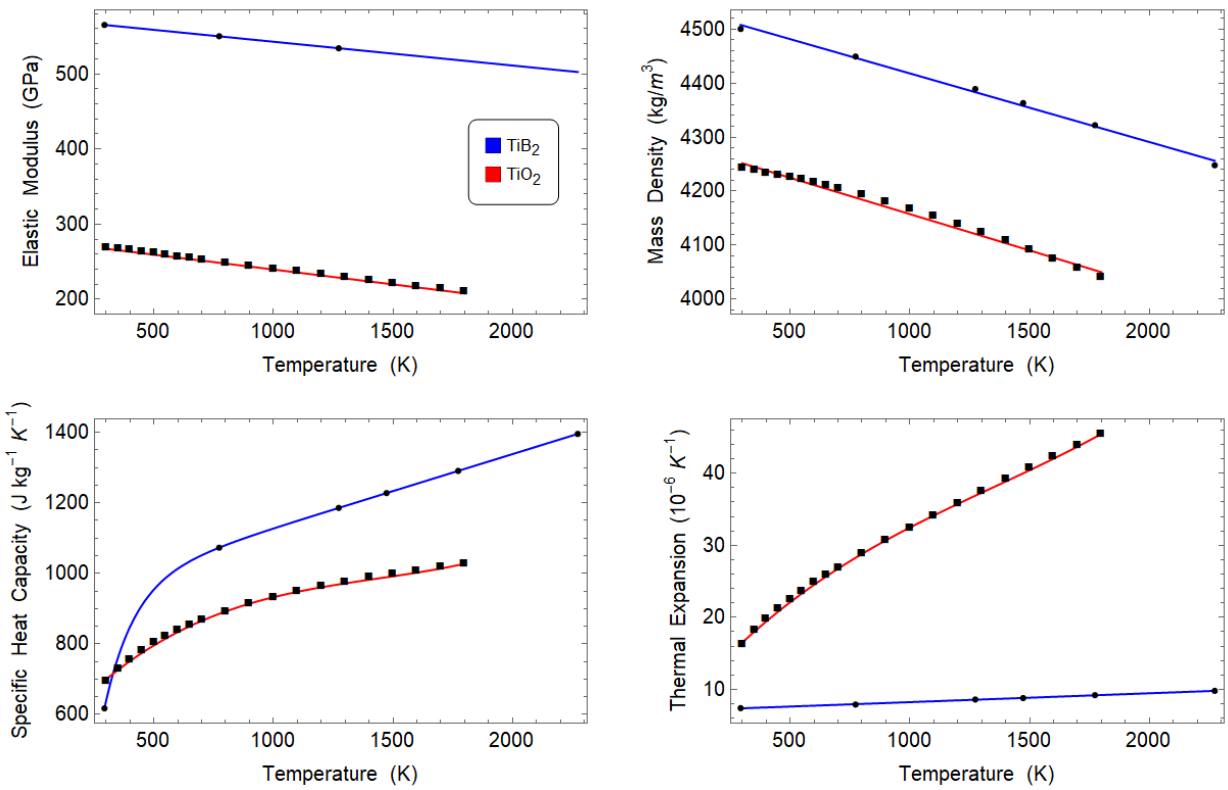

Figure 6.5: Temperature-dependent material properties for TiO_2 shown with previously established functions for TiB_2. The data points represent experimental values from Munro [32] and Isaak et al. [46] for TiB_2 and TiO_2, respectively. The blue and red curves show the data fit used for TiB_2 and TiO_2, respectively.

Table 6.2: Room temperature material properties for dense, fully sintered TiB_2 and TiO_2

Property	Value for TiB_2	Value for TiO_2
E (GPa)	565	268
ρ (kg/m^3)	4500	4240
$\tilde{\varepsilon_0}$ (%)	0.071	0.131
C_p (J/kg-K)	617	692
k (W/m-K)	96	8.1
α (1/K)	7.4×10^{-6}	16.1×10^{-6}
ν	0.108	0.28

The thermal profiles to be used for the hex snapshot simulations are identical to those used for the baseline hexagonal RVE simulations. For completeness, the thermal profiles are shown again in Figure 6.6, now with the addition of the elastic modulus of TiO_2.

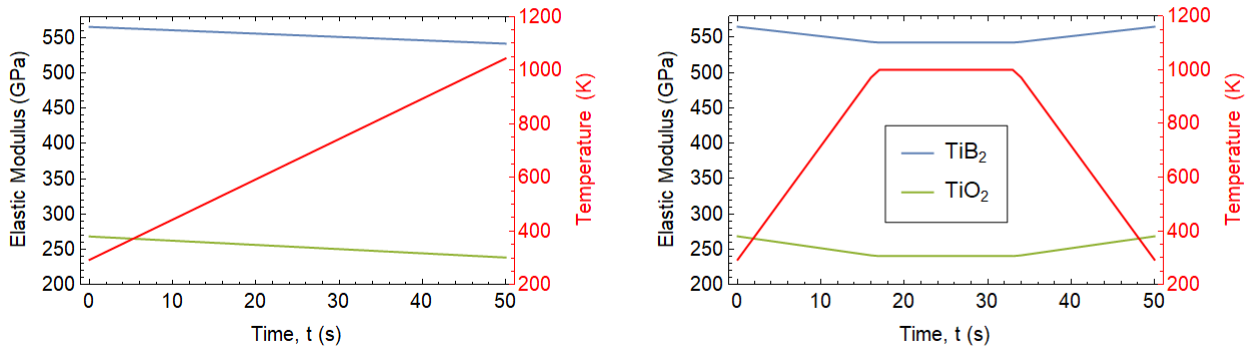

(a) Ramped Thermal Load

(b) Cyclic Thermal Load

Figure 6.6: Profile of the thermal load applied to the top boundary of the hexagonal RVE. The red curve shows the temperature while the variation of elastic moduli of each phase is shown to provide context.

6.2 Compressive Loading of Hex Snapshots

Since the snapshot oxide layer thicknesses were selected to show the full range of oxidation states for the hexagonal RVE with 40% macroporosity, this RVE was the focus of the initial set of simulations. An understanding of the mechanical response of this RVE at room temperature and under applied thermal loads was investigated before exploring the response of 10% and 70% macroporosity hex snapshots.

6.2.1 Mechanical Response of Hex Snapshots with 40% Porosity

The volume-averaged stress- and damage-strain curves for the hex snapshot with 40% macroporosity is shown in 6.7 and 6.8, respectively, up to an applied compressive strain of 30% in 0.6% steps at room temperature. In a qualitative sense, these curves demonstrate that thicker oxide layers reduce the slopes of the σ_{11} and σ_{22} curves, along with decreasing the compressive strength of the RVE while prolonging catastrophic failure to higher strain levels. Of particular interest is that the stress and damage responses for the 30 and 50 µm snapshots are nearly identical, implying that the percolation of the oxide contributes significantly to the overall response. These observations are quantified using the four previously defined metrics and have been tabulated in Table 6.3.

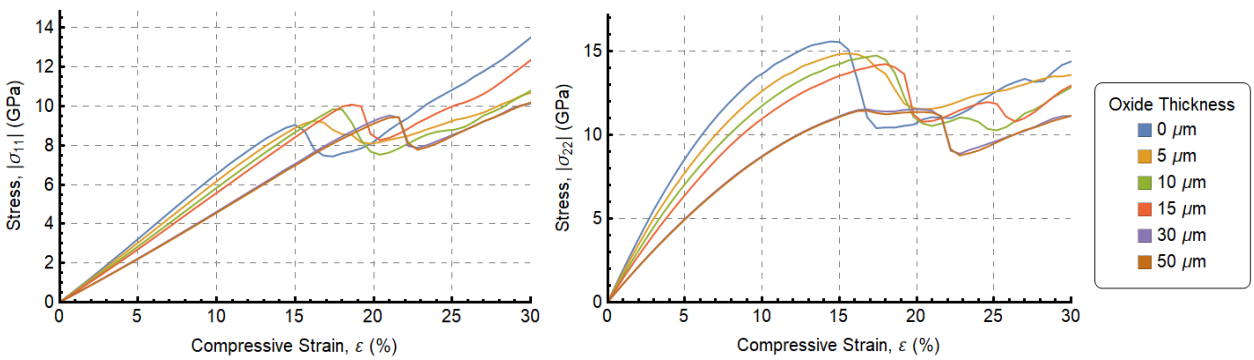

(a) Stress 11-Component (b) Stress 22-Component

Figure 6.7: Stress vs. compressive strain curves for hexagonal RVEs with 40% macroporosity at varying levels of oxidation.

The effective elastic modulus of the RVE is reduced by about 11% with each 5 µm increment, up to 15 µm, which equates to 2.2% per µm of oxide. The final stiffness reduction for the fully oxidized RVE is 48.8%, which is very close to the 52% reduction in the input elastic modulus for TiO_2 relative to TiB_2. As the oxide layer increases, there is a gradual increase in the micro-damage initiation strain from 0.6% to 1.32% until the oxide layer percolates at 30 µm, where the value drops to 1.2%. Prior to oxide percolation, the micro-damage initiation

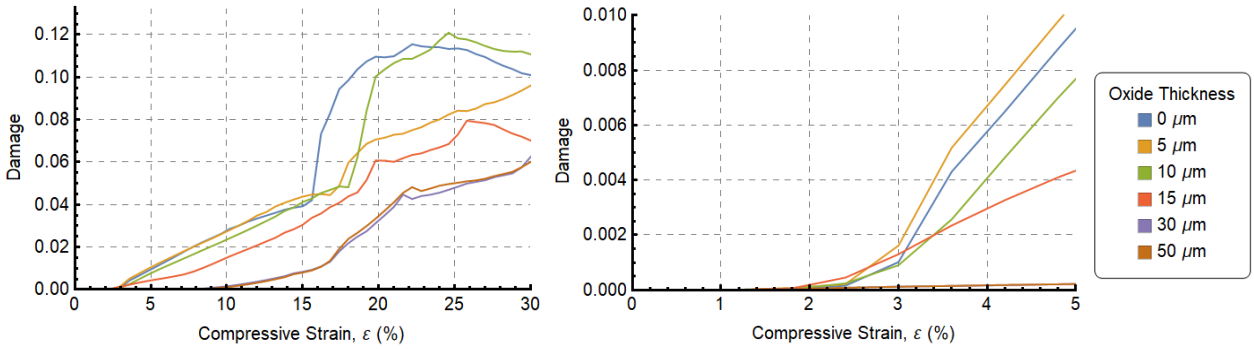

(a) Full Response (b) Initial Response

Figure 6.8: Damage vs. compressive strain curves for hexagonal RVEs with 40% macroporosity at varying levels of oxidation.

Table 6.3: Elastic and damage properties of hexagonal RVE snapshot with 40% macroporosity at room temperature at various levels of oxidation

Oxide Thickness (μm)	Effective Elastic Modulus (GPa)	Micro-Damage Initiation Strain (%)	Macro-Damage Initiation Strain (%)	Compressive Strength (MPa)
0	167	0.6	14.4	15,562
5	150	0.84	15.6	14,841
10	133	1.26	17.4	14,724
15	117	1.32	18	14,207
30	86.5	1.2	16.8	11,510
50	85.8	1.2	16.8	11,424

strain increases with thickness because a larger percentage of the volume becomes TiO_2, for which $\tilde{\varepsilon_0}$ is nearly double that of TiB_2. To understand why the micro-damage initiation strain of the RVE drops at 30 µm, Figure 6.9 provides contour plots of the 2nd principal stress fields for 15 and 30 µm hex snapshots. These indicate that the 15 µm snapshot benefits from the increased $\tilde{\varepsilon_0}$ associated with the TiO_2 phase, while the TiB_2 phase carries most of the compressive load. When the TiB_2 is reduced to the small triangular regions shown in the 30 µm snapshot, it no longer contributes significantly to the load-carrying capacity of the RVE, thus damage occurs slightly sooner.

Similar behavior is observed in the macro-damage initiation strain, which increases from

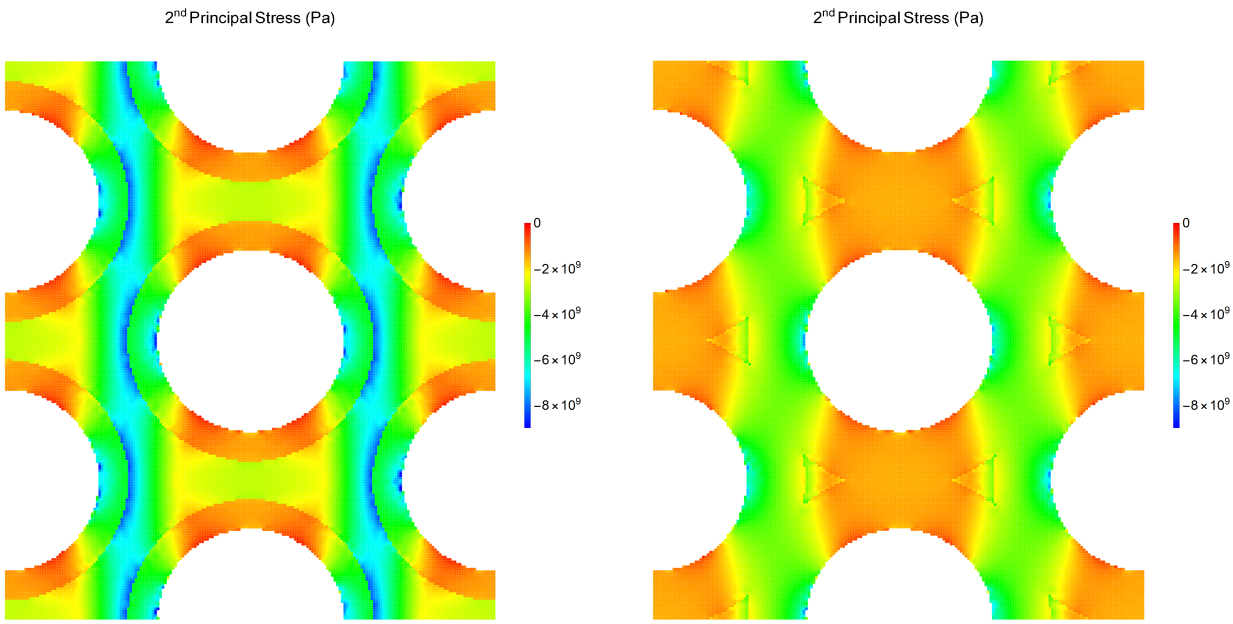

(a) $t_{ox} = 15\ \mu m$ (b) $t_{ox} = 30\ \mu m$

Figure 6.9: Contour plots of the 2nd principal stress fields for hex snapshots of $t_{ox} = 15$ µm (a) and $t_{ox} = 30$ µm (b) at their respective micro-damage initiation strains.

14.4% to 18% for the 15 µm snapshot, then drops to 16.8% for the 30 and 50 μm snapshots. The magnitude of the compressive strength is not reflective of the unconstrained material response, again due to the nature of the simulation boundary conditions, but the decreasing trend with increasing oxide layer thickness is expected. To further explore the decrease in macro-damage initiation strain for the 30 and 50 µm snapshots, the damage field contours at the macro-damage initiation strains of each snapshot RVE are shown in Figure 6.29. As observed in Section 5.3, damage accumulates in the form of shear bands through the thickness of the struts. The addition of the oxide layer introduces fully damaged hot spots that form on the surface of the pores. As the oxide layer is increased, these hot spots diminish and the shear bands decrease in size, with most of the damage occurring in the TiB_2 portion of the strut.

Upon percolation of the oxide layer, the magnitude of damage in the struts is reduced from

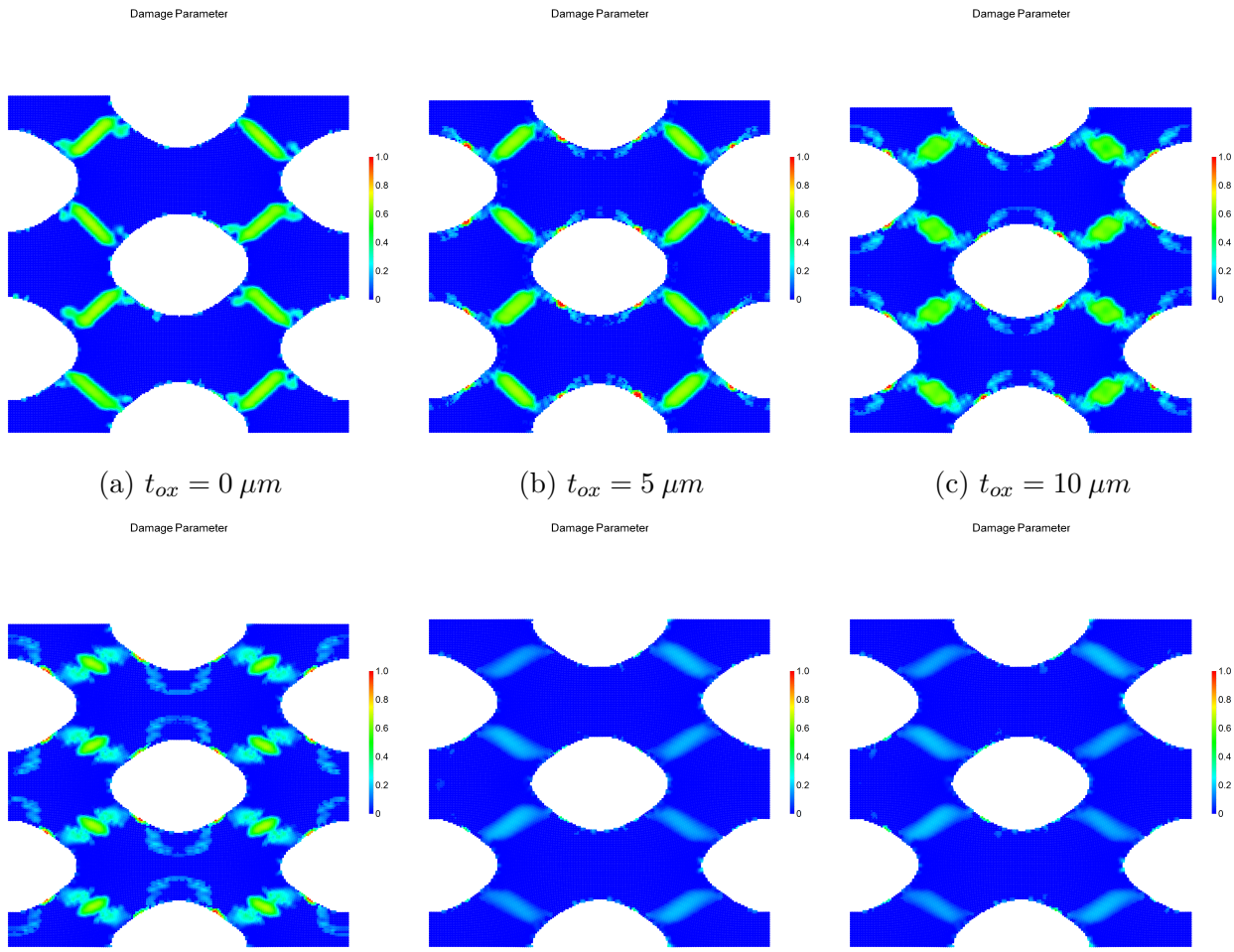

(a) $t_{ox} = 0\ \mu m$ (b) $t_{ox} = 5\ \mu m$ (c) $t_{ox} = 10\ \mu m$

(d) $t_{ox} = 15\ \mu m$ (e) $t_{ox} = 30\ \mu m$ (f) $t_{ox} = 50\ \mu m$

Figure 6.10: Damage field contour plots for hex snapshot with 40% macroporosity showing the room temperature response at the corresponding macro-damage initiation strain with varying levels of oxide layer thickness

0.6 to 0.3, which is consistent with the trend established so far. Referring back to Figure 6.7(b), the general behavior of the 30 and 50 µm snapshots is different than that of the thinner oxide layer snapshots in that it reaches the macro-damage initiation strain, but σ_{22} plateaus until the RVEs finally experience macroscale failure at 21% applied strain. With this observation, it can be concluded that the 30 and 50 µm snapshots experience peak compressive loading at at a lower strain value than the other snapshots, but macroscale failure does not occur until the applied strain reaches 21%. The damage contours at this

strain level are shown in Figure 6.11, wherein damage is concentrated along the surface pores and in shear bands across the upper struts. The unsymmetrical location of the damaged regions is likely due to the Weibull distribution being used.

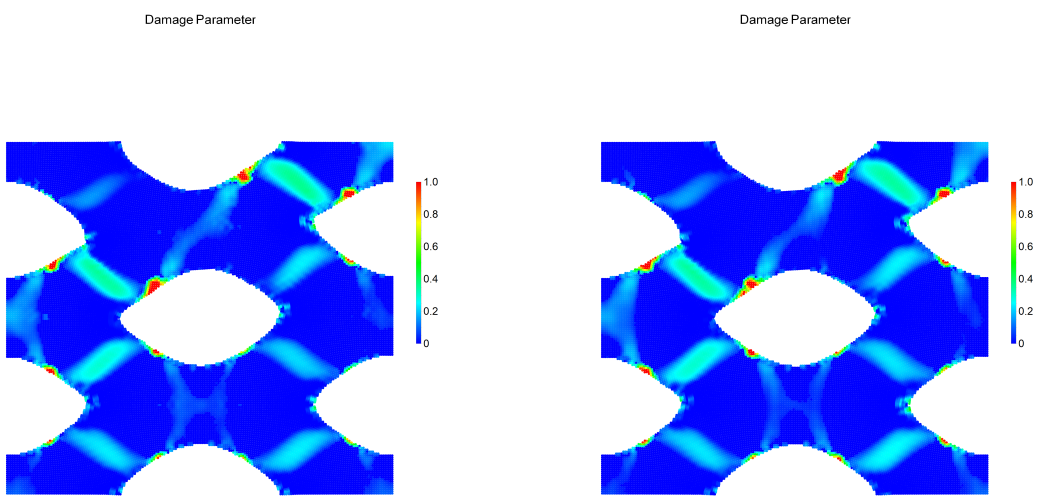

(a) $t_{ox} = 30\ \mu m$ (b) $t_{ox} = 50\ \mu m$

Figure 6.11: Damage field contour plots for RVEs with oxide layers of (a) 30 µm and (b) 50 µm subjected to 21% applied compressive strain

To conclude the room temperature compressive simulation results for the 40% macroporosity hex snapshots, Figure 6.12 shows contour plots of the damage fields at 22.8% applied strain, where each snapshot RVE has experienced macroscale failure. In general, regardless of the level of oxidation, shear failure in the struts remains the predominant failure mechanism for RVEs of this macroporosity level. It should be noted, however, that the 30 and 50 µm snapshots experience significant damage only in the upper struts, rather than across the entire RVE. This is consistent with the notably lower volume-averaged damage response seen in these two RVEs. It should also be mentioned that the small region of remaining TiB_2 in the 30 µm snapshot RVE has very little contribution to the overall response considering that the damage contour is nearly identical to that of the 50 µm snapshot.

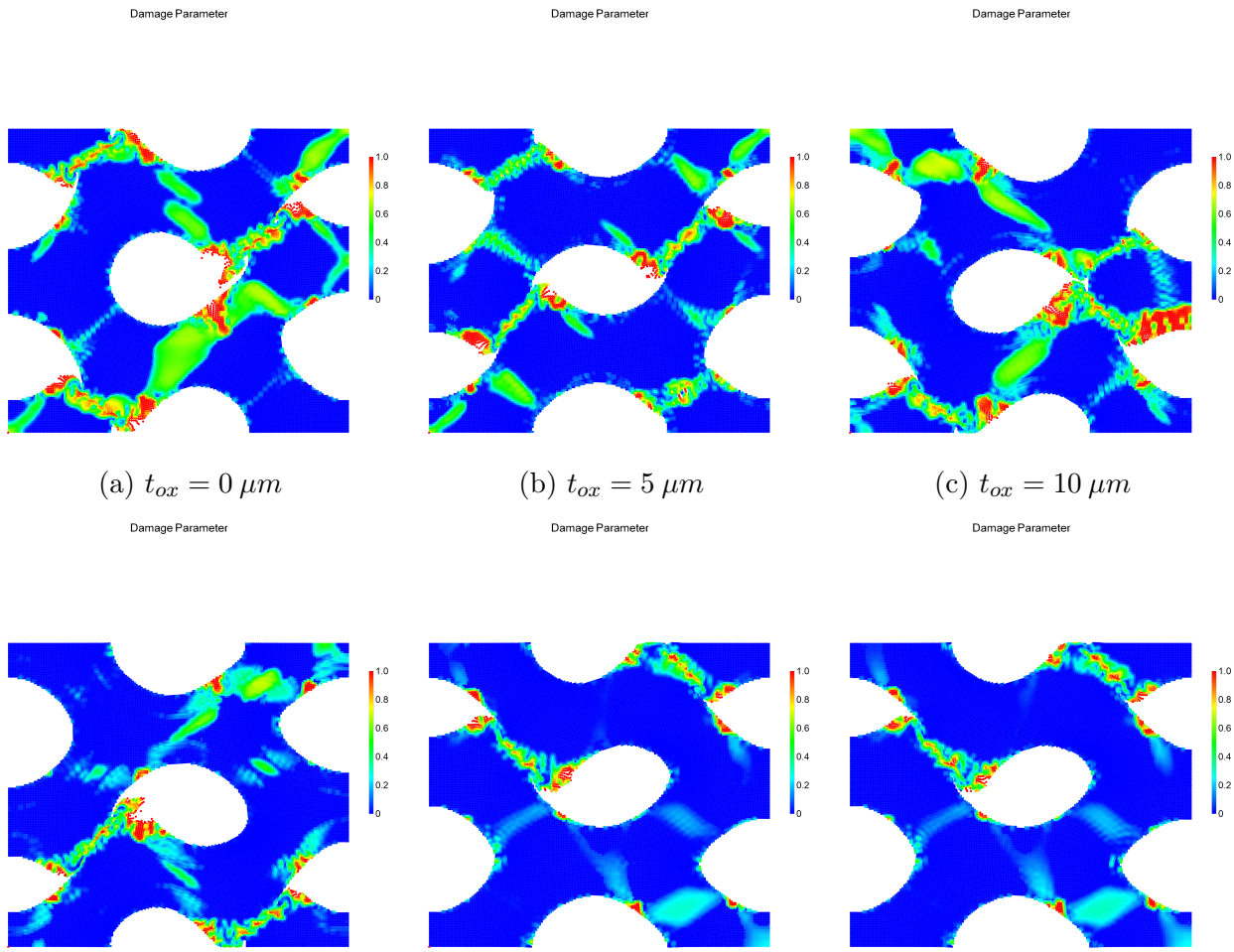

(a) $t_{ox} = 0\ \mu m$ (b) $t_{ox} = 5\ \mu m$ (c) $t_{ox} = 10\ \mu m$

(d) $t_{ox} = 15\ \mu m$ (e) $t_{ox} = 30\ \mu m$ (f) $t_{ox} = 50\ \mu m$

Figure 6.12: Damage field contour plots for hex snapshot with 40% macroporosity showing the room temperature response at 22.8% applied compressive strain with varying levels of oxide layer thickness

Effects of Ramped Thermal Loading

The effects of thermal expansion were introduced by applying the ramped thermal load as defined Section 5.2.2 to the 40% macroporosity hex snapshots. To isolate the stress due to thermal expansion, simulations were performed wherein the RVE was fully constrained then subjected to the ramped thermal load without any applied engineering strain. The corresponding stress-time curves are shown in Figure 6.13. Both stress components increase

proportionally with the thermal load for all snapshots, as in the unoxidized hexagonal RVEs, however the magnitude of each stress component at any given time increases with the oxide layer thickness. This is due to the thermal expansion coefficient of TiO_2 increasing as the temperature rises in the upper half of the RVE. A notable deviation from the response of the unoxidized hexagonal RVEs due to constrained thermal loading is that the volume averaged damage is nonzero in RVEs with both phases present, which is consistent with the mismatch in thermal expansion coefficients of the two materials. Figure 6.14 shows that the most damage accumulates in the 5 µm snapshot, while the 30 µm snapshot shows the least amount of volume-averaged damage.

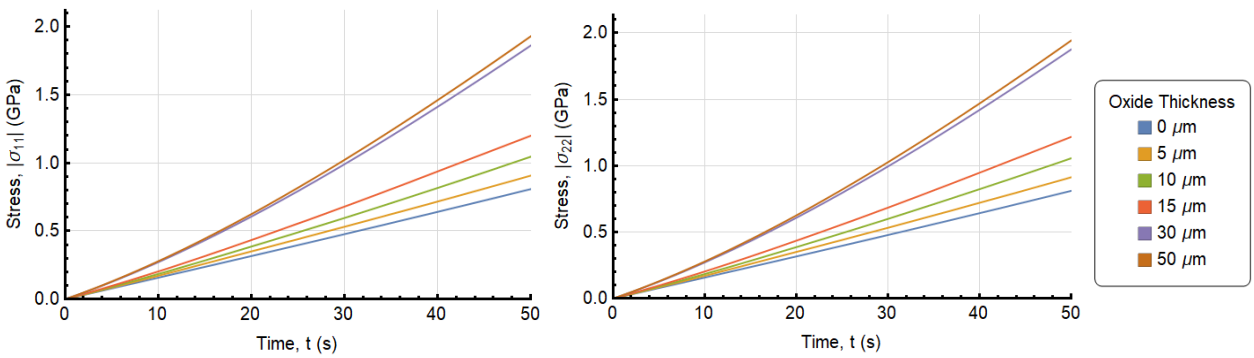

(a) Stress 11-Component (b) Stress 22-Component

Figure 6.13: Compressive stress-time curves for hexagonal RVEs with 40% macroporosity subjected to the ramped thermal load at varying levels of oxidation.

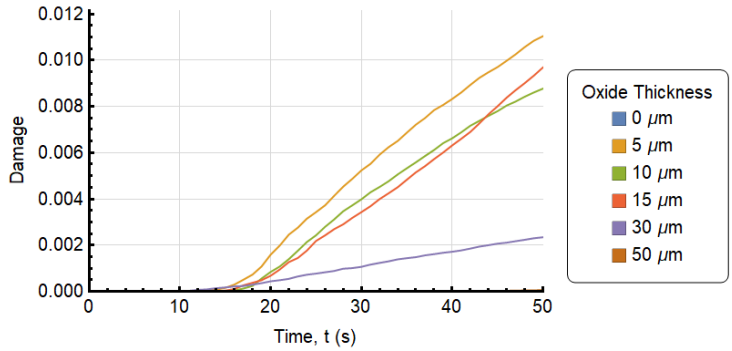

Figure 6.14: Damage-time curves for hexagonal RVEs with 40% macroporosity subjected to the ramped thermal load at varying levels of oxidation.

To understand where the damage due to thermal expansion occurs in the two-phase RVEs, the damage field contour plots corresponding to $t = 49\ s$ are shown in Figure 6.15. The contours for the 0 and 50 µm snapshots are omitted because no damage occurs in these RVEs given that they are comprised of entirely TiB_2 and TiO_2, respectively. Consistent with the temperature distribution shown in Figure 5.8(b), the greatest thermal expansion and thus the most damage occurs in the upper portions of each RVE, typically along the phase interfaces surrounding each pore. The magnitude of the damage follows a similar trend to the room temperature compressive strain simulations in that the average damage decreases for RVEs with thicker oxide layers. This can again be attributed to the increase in damage initiation strain associated with the oxide phase material and the reduction in the size of the phase interface regions.

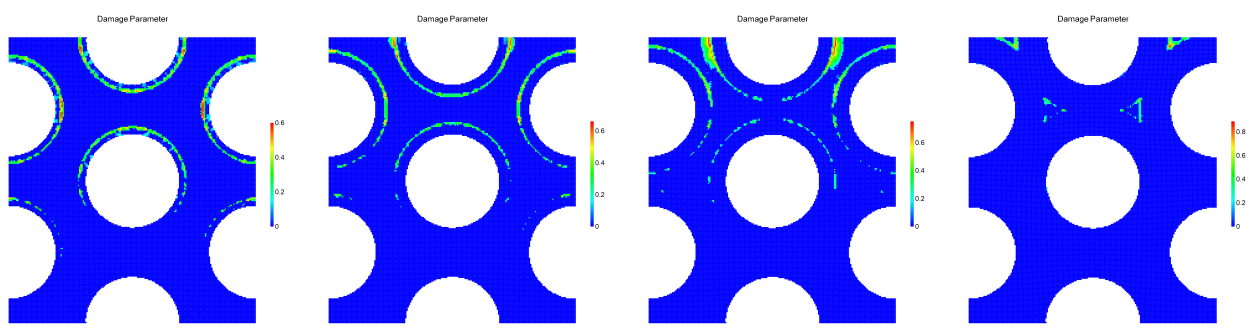

(a) $t_{ox} = 5\ \mu m$ (b) $t_{ox} = 10\ \mu m$ (c) $t_{ox} = 15\ \mu m$ (d) $t_{ox} = 30\ \mu m$

Figure 6.15: Damage field contour plots for hex snapshots with 40% macroporosity showing the response at $t = 49s$ with a ramped thermal load and no applied engineering strain

With this understanding of how the hex snapshots behave due to constrained thermal expansion, the ramped thermal load was applied to compressive strain simulations. The stress-strain response for these simulations is plotted against the room temperature (RT) simulation response in Figure 6.16. These plots indicate an increase in the magnitude of σ_{11} over the room temperature simulations as the oxide layer is increased, while the difference in magnitude of σ_{22} qualitatively appears to be constant for all snapshots. This implies that the

thermal expansion manifests itself in σ_{11} more than in σ_{22}. The damage-strain curves in Figure 6.17 show that significant deviation from the room temperature response is only seen after macroscale failure occurs, which is due to the complex combination of thermal and mechanical loading.

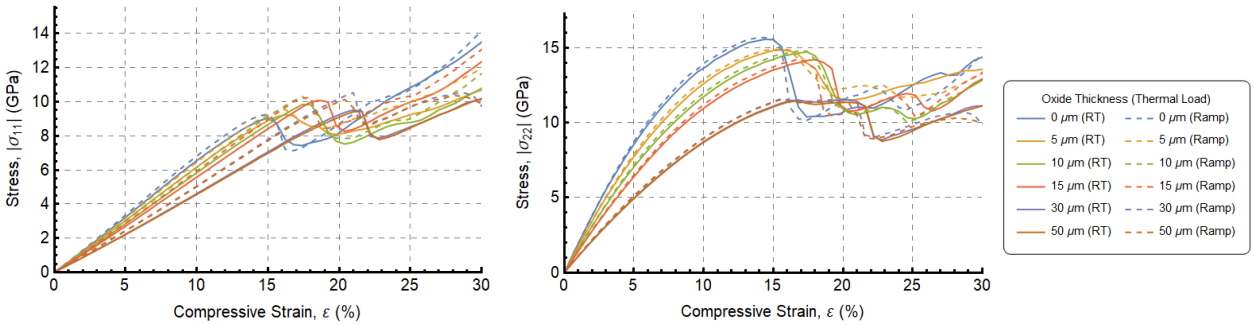

(a) Stress 11-Component (b) Stress 22-Component

Figure 6.16: Stress vs. compressive strain curves for hexagonal RVEs with 40% macroporosity subjected to the ramped thermal load at varying levels of oxidation.

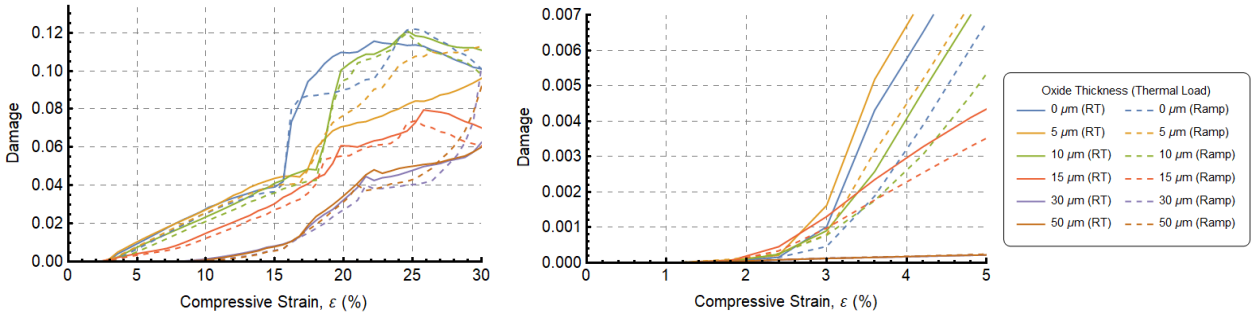

(a) Full Response (b) Initial Response

Figure 6.17: Damage vs. compressive strain curves for hexagonal RVEs with 40% macroporosity subjected to the ramped thermal load at varying levels of oxidation.

To further compare the responses, the elastic and damage metrics for the ramped thermal load simulations are presented in Table 6.4. With the exception of the 10 µm snapshot, the effective elastic modulus increased by about 1 GPa due to the ramped thermal load, which is consistent with the unoxidized RVEs. In the 0 µm snapshot, the ramped thermal load only decreases the micro-damage initiation strain by 10%, while the oxidized snapshot micro-damage initiation strains are reduced by an average of 30% due to the additional damage

caused by the thermal expansion mismatch. For RVEs with oxide layers of 15 µm or greater, the macro-damage initiation strain is 6 to 7% lower than in the room temperature simulations. For simulations with increasing oxide layer thickness, the corresponding increase in compressive strength ranges from 0.34% to 1.2% for the 5 and 50 µm snapshots, respectively. Of these four metrics, the micro- and macro-damage initiation strains of the oxidized RVEs are affected the most by the ramped thermal load, while there is only a marginal increase in the effective stiffness and compressive strength due to thermal expansion and the homogeneous boundary conditions.

Table 6.4: Elastic and damage properties of 40% hexagonal RVE snapshots with the ramped thermal load applied at various levels of oxidation

Oxide Thickness (μm)	Effective Elastic Modulus (GPa)	Micro-Damage Initiation Strain (%)	Macro-Damage Initiation Strain (%)	Compressive Strength (MPa)
0	168	0.54	14.4	15,681
5	151	0.60	15.6	14,891
10	133	0.78	17.4	14,778
15	118	0.84	16.8	14,249
30	87.1	0.90	15.6	11,608
50	86.4	0.96	15.6	11,562

Effects of Cyclic Thermal Loading

Next, the effects of thermal expansion due to a heating and cooling cycle were investigated by applying the cyclic thermal load as defined Section 5.2.2 to the 40% macroporosity hex snapshots. The stress-time curves corresponding to constrained thermal expansion induced by this thermal profile are shown in Figure 6.18. Similar to the response to ramped thermal loading, the magnitude of each stress component at any given time increases with the oxide layer thickness. The volume-averaged damage vs. time curves in Figure 6.19(a) show that the damage behavior is similar to that of the ramped thermal case when $t < 33\ s$, then it

plateaus from $33 < t < 66\,s$ before beginning to decrease as the top boundary is cooled. This cooling causes damaged regions, previously in tension, to be loaded in compression and thus the tensile damage scalar α_t effectively reduces the damage present in the material. It is important to note that the tensile damage state of these material points is retained within the damage parameter d_t, should the material point be loaded in tension again at a later point in the simulation. This is consistent with the assertion that damage must monotonically increase. Figure 6.19(b) shows the volume-averaged tensile damage vs. time curves, thus confirming that compression of damaged regions causes the total damage parameter to decrease while the level of tensile damage is retained.

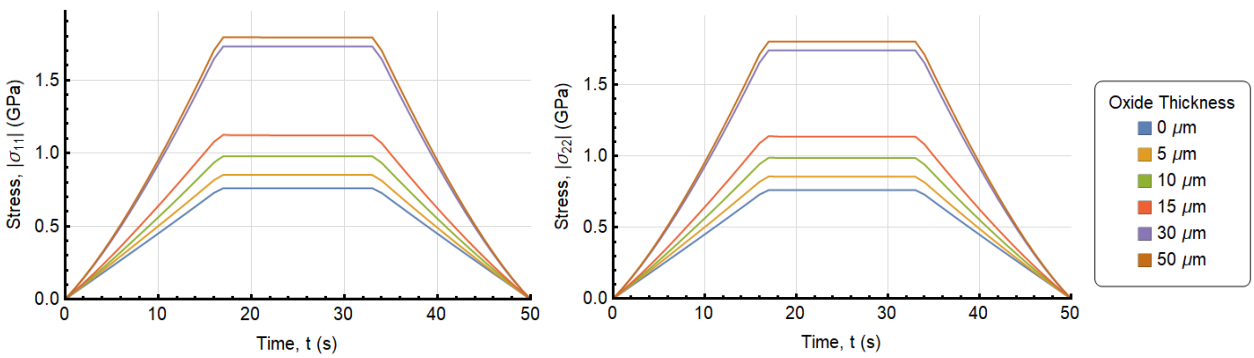

(a) Stress 11-Component (b) Stress 22-Component

Figure 6.18: Compressive stress-time curves for hexagonal RVEs with 40% macroporosity subjected to the cyclic thermal load at varying levels of oxidation.

Irregular behavior is observed in the final time steps of the cyclic thermal load simulations where the damage suddenly increases. The left column of Figure 6.20 shows the damage field contours for 5 µm (a) and 50 µm (b) snapshots just before this damage spike ($t = 48\,s$), while the right column shows the damage fields at the end of the simulation ($t = 50\,s$). Aside from two small damage hot spots on the left and right sides of the central upper pore surface and an increase of the damage at the oxide-substrate interfaces, there does not appear to be any discernible difference in the damage fields between 48 and 50 s for the 5 µm snapshot. The spike is less sharp for the 50 µm snapshot and the damage is attributed to some level

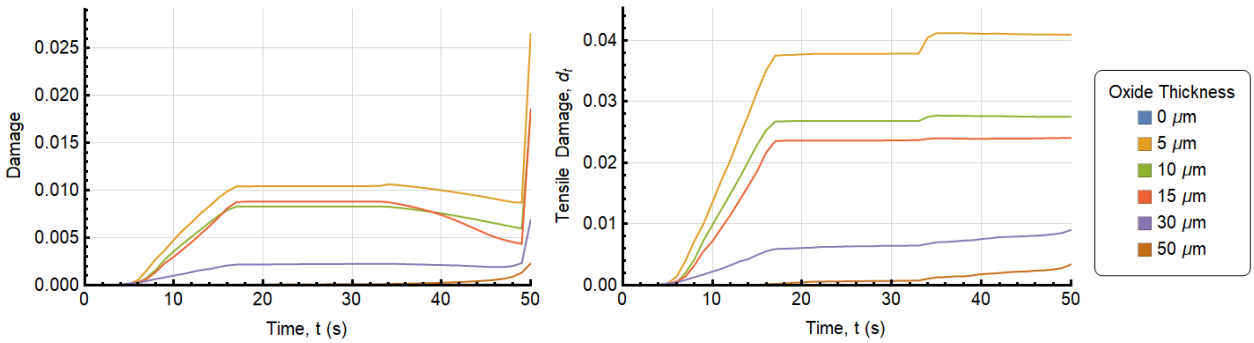

(a) Damage Parameter (b) Tensile Damage Parameter

Figure 6.19: Damage (a) and tensile damage (b) vs. time curves for hexagonal RVEs with 40% macroporosity subjected to the cyclic thermal load at varying levels of oxidation.

of tensile strain occurring at the pore edges due to the increased thermal expansion of the oxide phase followed by shrinking that results from the cooling cycle. While this damage behavior is not well understood, its affect in the overall response of the RVE is minimal due to its magnitude of just 3%.

Simulations were then performed for the 40% macroporosity hex snapshot under combined cyclic thermal loading and applied compressive strain. The volume-averaged stress-strain and damage-strain curves are shown in Figures 6.21 and 6.22, respectively. Prior to reaching the macro-damage initiation strain, the stress and damage responses are qualitatively similar to the room temperature simulation results. Following macroscale failure, the damage response varies significantly. Damage in the 5, 30 and 50 µm snapshots climbs after macroscale failure occurs, while the damage in the 10 and 15 µm snapshots decreases instead. This difference in behavior is attributed to the interaction of the mechanical and thermal loads, wherein the thermal stresses are decreased while the applied engineering strain continues to increase.

The elastic and damage comparison metrics for the cyclic thermal load simulations are presented in Table 6.5. The general nature of the changes in the elastic modulus, micro-damage initiation strain, and compressive strength relative to the room temperature simulations is

similar to the changes observed due to ramped thermal loading, therefore a detailed discussion of these data would be redundant. However, it should be noted that the macro-damage

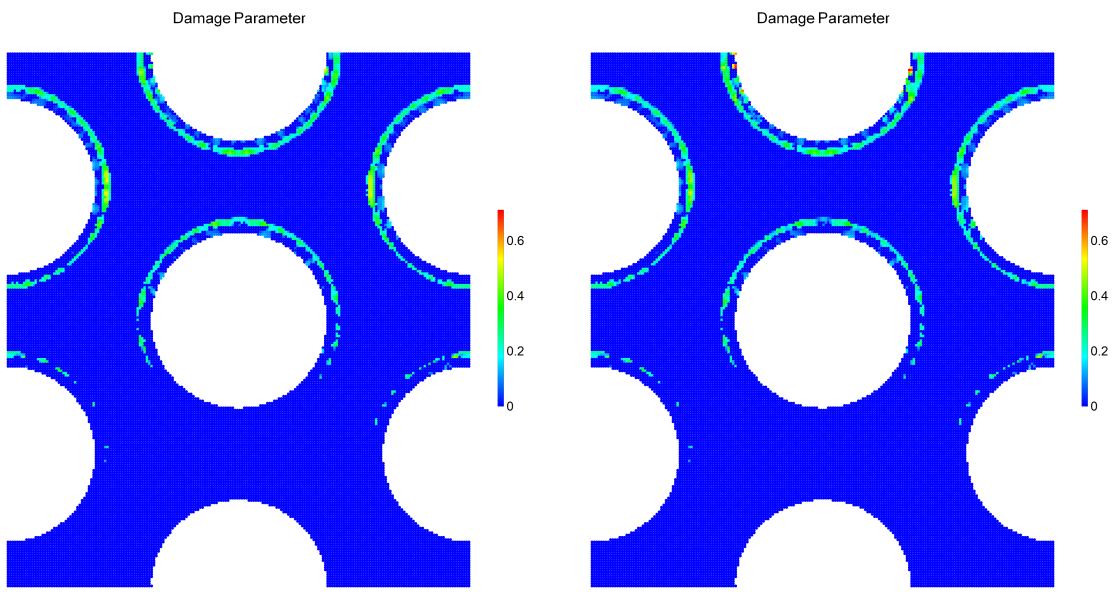

(a) $t_{ox} = 5\ \mu m$

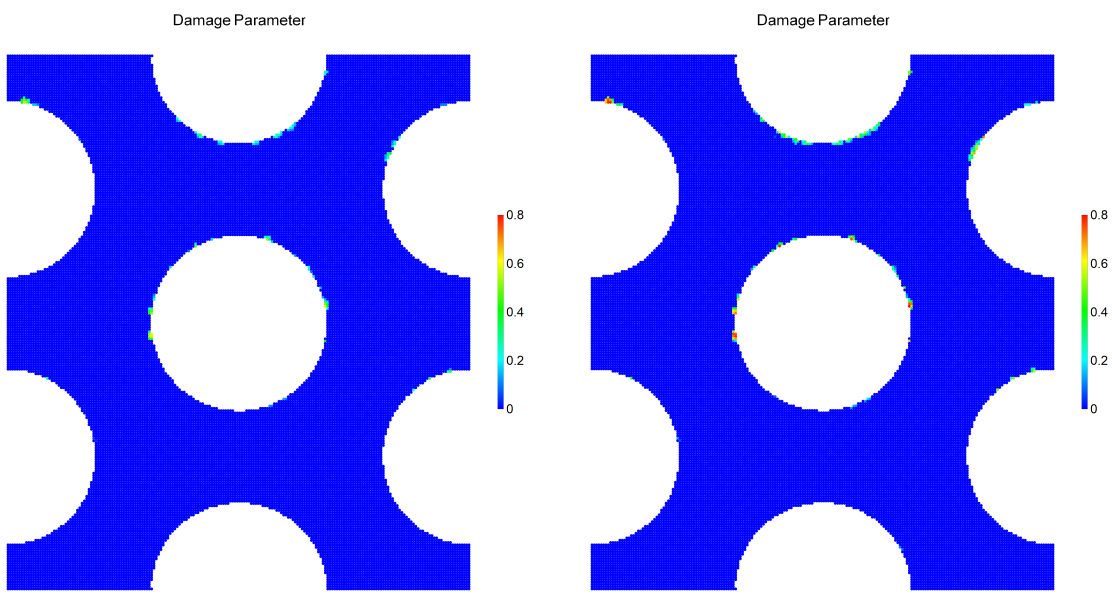

(b) $t_{ox} = 50\ \mu m$

Figure 6.20: Damage field contour plots for hex snapshots with 40% macroporosity subjected to the cyclic thermal load. The left and right columns for each oxide layer show $t = 48s$ and $t = 50s$, respectively.

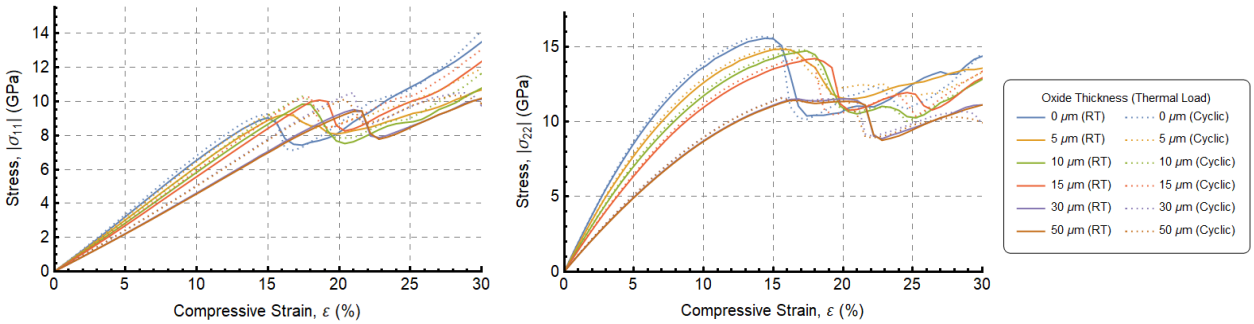

(a) Stress 11-Component (b) Stress 22-Component

Figure 6.21: Stress vs. compressive strain curves for hexagonal RVEs with 40% macroporosity subjected to the cyclic thermal load at varying levels of oxidation.

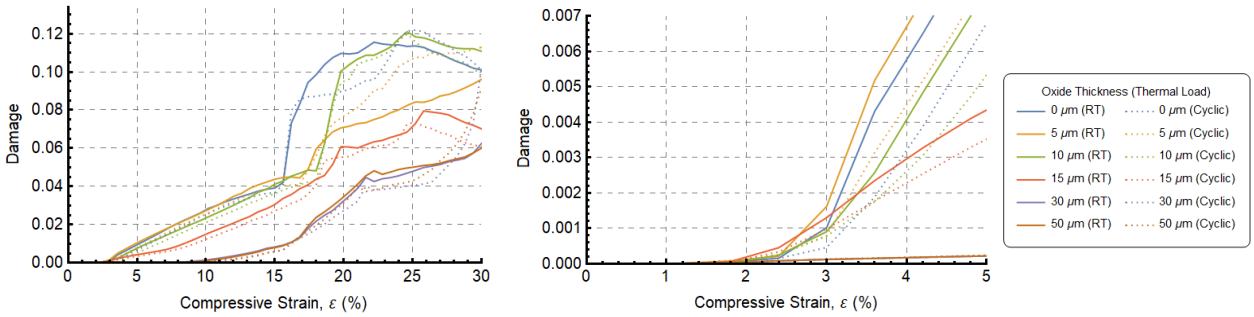

(a) Full Response (b) Initial Response

Figure 6.22: Damage vs. compressive strain curves for hexagonal RVEs with 40% macroporosity subjected to the cyclic thermal load at varying levels of oxidation.

initiation strain occurs one strain step earlier for all snapshots, which makes sense given that the increased heating rate leads to higher thermal stresses.

Table 6.5: Elastic and damage properties of 40% hexagonal RVE snapshots with the cyclic thermal load applied at various levels of oxidation

Oxide Thickness (μm)	Effective Elastic Modulus (GPa)	Micro-Damage Initiation Strain (%)	Macro-Damage Initiation Strain (%)	Compressive Strength (MPa)
0	169	0.48	13.8	15,715
5	152	0.24	15	14,989
10	134	0.36	16.2	14,801
15	119	0.36	15	14,015
30	88.1	0.54	15	11,801
50	87.4	0.60	15	11,769

Comparison of Thermal Loading Effects

To put the simulation results for each thermal load case in the proper relative context, a comparison for oxidation levels of 0, 15, and 30 µm is presented. Specifically, the volume-averaged stress- and damage-strain curves for these snapshots are shown in Figures 6.23 and 6.24, respectively. These curves are the result of previously discussed thermomechanical simulations at room temperature (RT) and under ramped and cyclic thermal loading.

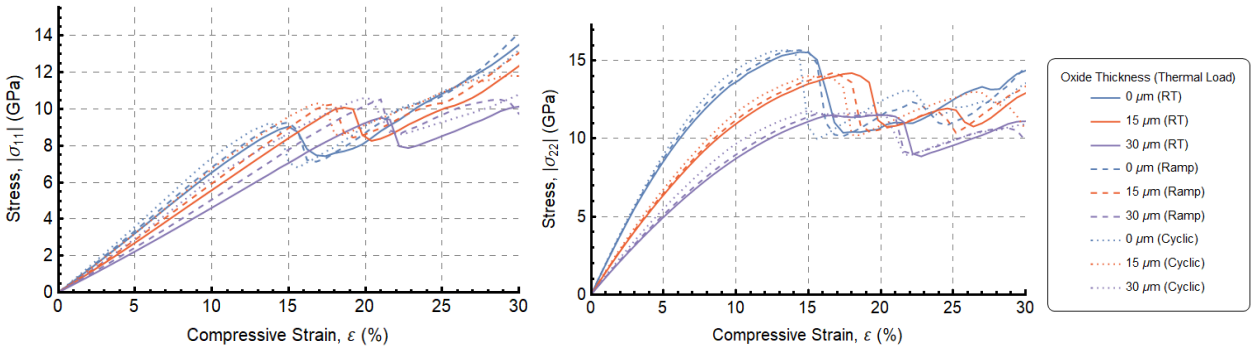

(a) Stress 11-Component (b) Stress 22-Component

Figure 6.23: Stress vs. compressive strain curves for hexagonal RVEs with 40% macroporosity subjected to each thermal load at varying levels of oxidation.

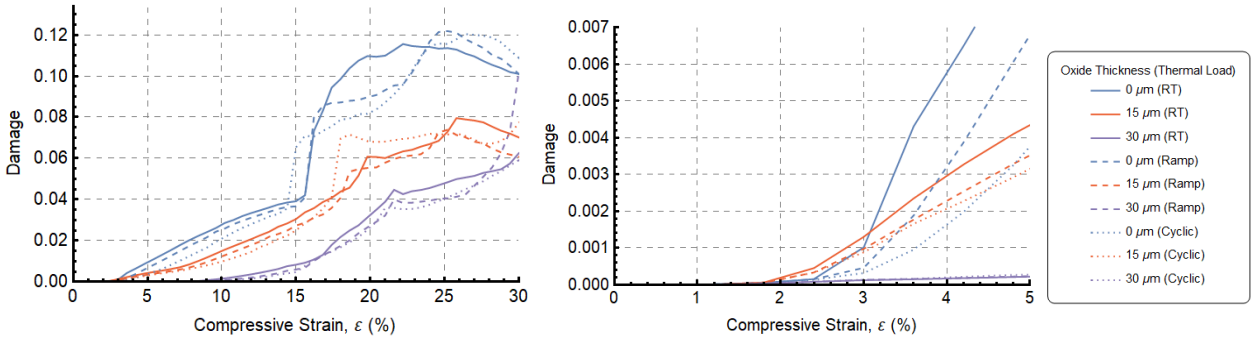

(a) Full Response (b) Initial Response

Figure 6.24: Damage vs. compressive strain curves for hexagonal RVEs with 40% macroporosity subjected to each thermal load at varying levels of oxidation.

To better interpret these figures, the elastic and damage metrics from Tables 6.3, 6.4, and 6.5 are plotted versus oxide layer thickness for each thermal load case in Figure 6.25. It is

immediately apparent that the effective elastic modulus shows little variation with thermal load. The only change to be expected for this metric is due to the slight difference in temperature at the first load step, where the effective stiffness is calculated. Similarly, the compressive strength varies minimally with oxide thickness, though it should be noted that the 15 µm snapshot is the only one which exhibits a decrease in compressive strength due to cyclic thermal loading. This is attributed to this snapshot experiencing the largest decrease in macro-damage initiation strain relative to the others when subjected to cyclic thermal loading.

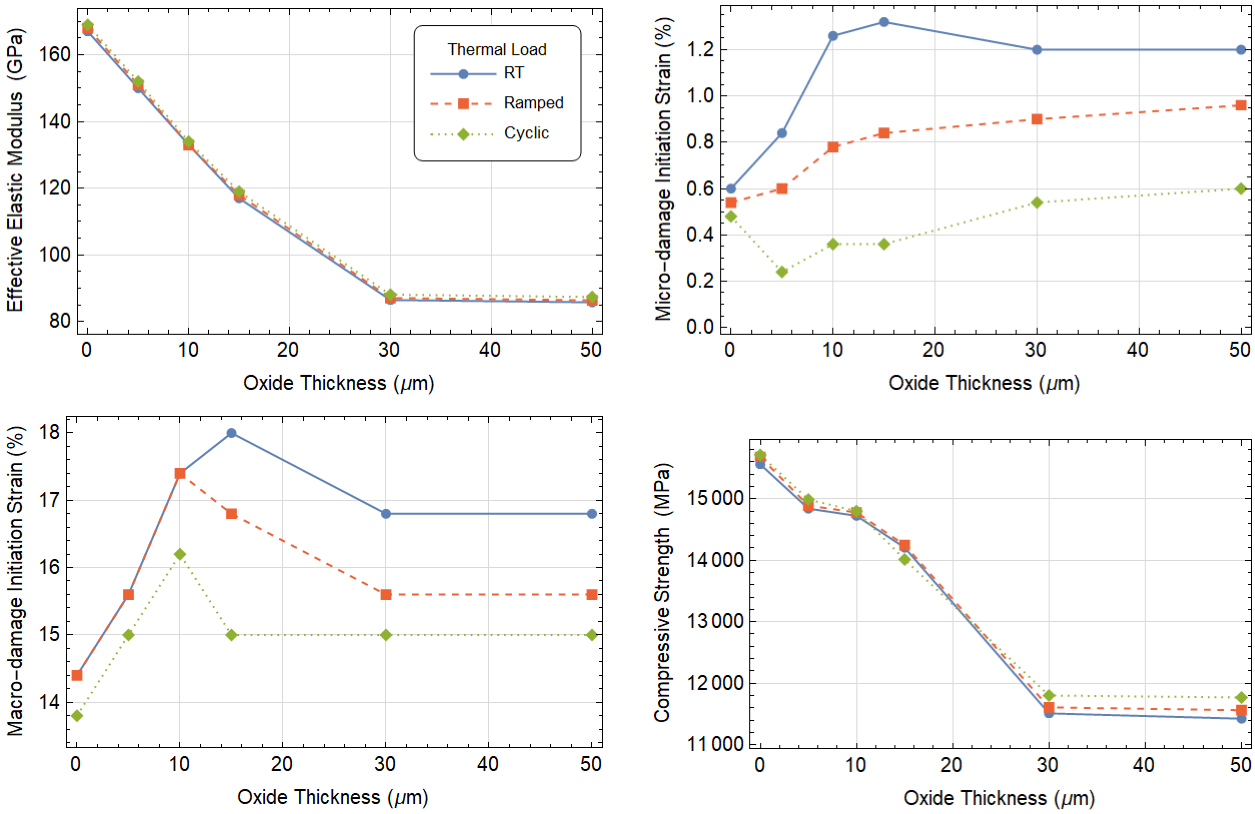

Figure 6.25: Metric comparison for the 40% porous hex snapshot across all three thermal load cases.

The micro-damage initiation strain behavior appears to be inconsistent across the thermal load cases because it increases with oxide thickness at room temperature and under ramped

thermal loading, but decreases when small oxide layers are introduced and cyclic thermal loading is applied. The general trend of the micro-damage initiation strain values, however, decrease as the initial heating rate increases, which is consistent with the behavior observed in the unoxidized RVEs. Compared to the room temperature simulations, the macro-damage initiation strain does not change for oxide layers of 10 µm or less when subjected to ramped thermal loading, while the increased heating rate of the cyclic thermal load causes a decrease for all oxide layer thicknesses. One noteworthy trend observed in each of the metrics is that there is a negligible change between the values obtained from the 30 and 50 µm snapshots. Thus it can be concluded that once the oxide regions percolate, the thermomechanical response will not degrade significantly due to further oxidation.

The response of the 40% macroporosity hex snapshots subjected to compressive strains at room temperature, constrained thermal expansion, and combined thermomechanical loading has been investigated. The room temperature mechanical response of the baseline hexagonal RVEs, combined with this study of the 40% snapshots at room temperature, is deemed sufficient for understanding the effects of oxidation in the 10% and 70% macroporosity hex snapshots with no applied thermal load. Therefore, it was decided that simulations for hex snapshots with 10% and 70% macroporosity would only be performed for a combination of compressive mechanical loading and thermal loading. Due to the complexity in the response to cyclic thermal loading, the ramped thermal load was selected as the only thermal profile to proceed with. This allows the affects of oxidation and thermal expansion to be characterized in a manner more consistent with real-world testing, where the cooling rate proposed in the cyclic thermal profile may be infeasible relative to the initial heating rate.

6.2.2 Mechanical Response of Hex Snapshots with 10% Porosity

Following an in-depth investigation of the hex snapshots with 40% macroporosity, thermo-mechanical simulations comprised of compressive applied strain and ramped thermal loading were performed for snapshots containing 10% macroporosity. The volume-averaged stress-strain curves shown in Figure 6.26 illustrate that σ_{11} does not vary significantly with oxidation. The volume-averaged damage-strain curves are shown in Figure 6.27, which indicate that while the damage behavior roughly follows the same trend in snapshots with oxide layers of 15 µm or lower, the 30 and 50 µm thick oxide layer snapshots develop less damage at low strain levels and throughout the simulation.

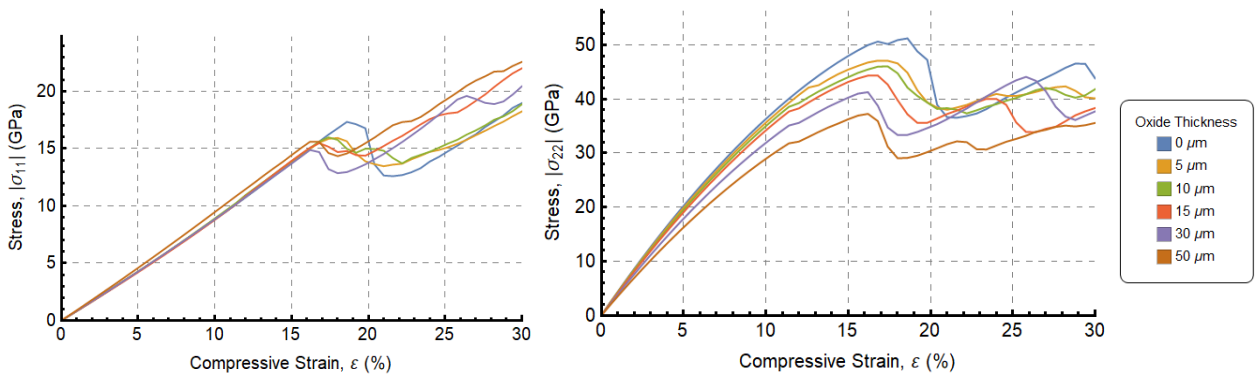

(a) Stress 11-Component (b) Stress 22-Component

Figure 6.26: Stress vs. compressive strain curves for hexagonal RVEs with 10% macroporosity subjected to the ramped thermal load at varying levels of oxidation.

The elastic and damage metrics summarized in Table 6.6 show that the effective elastic modulus is reduced by less than 0.4% per µm of oxide layer thickness applied, leading to a final 23% reduction for the 50 µm snapshot. This small change is due to the oxide layer making up a lesser volume fraction of the RVE compared to snapshots with 40% or 70% macroporosity. The micro-damage initiation strain increases from 0.24% to 0.42% due to the first 5 µm layer, but this value decreases to 0.36% for the 10µm snapshot. When the 50 µm layer is applied, the micro-damage initiation strain increases to a maximum value of 1.02%

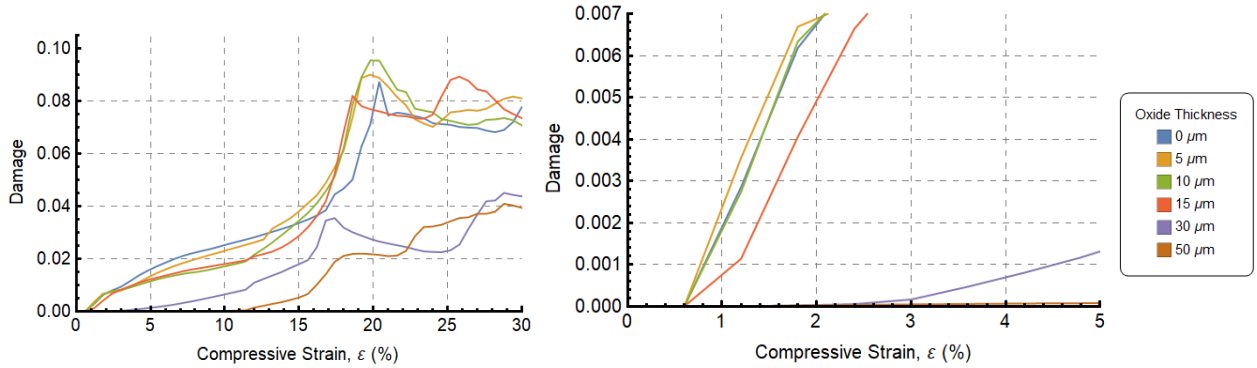

(a) Full Response (b) Initial Response

Figure 6.27: Damage vs. compressive strain curves for hexagonal RVEs with 10% macroporosity subjected to the ramped thermal load at varying levels of oxidation.

strain, which is four times higher than in the unoxidized RVE. The macro-damage initiation strain does not change due to an oxide thickness of 5 µm, but the corresponding compressive strength drops by 6.9%. For a thickness of 10 µm, the macro-damage initiation strain increases to 17.4% while the compressive strength falls by 2.2%. The remaining snapshots experience macroscale failure at the same strain level of 16.2%, but the compressive strength continues to decrease. Overall, the compressive strength decreases by $1 \pm 0.5\%$ per µm of oxide, which leads to a final reduction of 33% for the 50 µm snapshot compared to the unoxidized RVE.

Table 6.6: Elastic and damage properties of 10% hexagonal RVE snapshots with the ramped thermal load applied at various levels of oxidation

Oxide Thickness (μm)	Effective Elastic Modulus (GPa)	Micro-Damage Initiation Strain (%)	Macro-Damage Initiation Strain (%)	Compressive Strength (MPa)
0	421	0.24	16.8	50,634
5	413	0.42	16.8	47,108
10	404	0.36	17.4	46,051
15	395	0.66	16.2	44,345
30	366	0.78	16.2	41,278
50	324	1.02	16.2	37,271

The damage field contours at the respective macro-damage initiation strains for each 10% macroporosity hex snapshot are shown in Figure 6.28. It is observed in these plots that the damage reduction seen in Figure 6.27 is due to the phase transition on the pore surfaces. The damage hot spots shown in 6.28(a) remain the most critical regions, even when oxide layers of up to 30 µm are introduced. It is not until the 50 µm layer is applied that the pore hot spots are nearly completely eliminated in favor of mild damage-level shear bands forming in the lower struts. Figure 6.29 shows the damage fields in the same RVEs subjected to 21% compressive strain to illustrate where macroscale failure occurs. The snapshots of 15 µm thickness or less show damage accumulation at the pores in addition to through-strut shear failure. These contours reveal that the increased damage-initiation strain and decreased elastic modulus in the oxide layer surrounding the pores inhibits this pore-centralized damage accumulation. Instead, the struts experience isolated shear failure.

As predicted due to the increased size of the 10% macroporosity hexagonal RVE compared to the oxide layer, the levels of oxidation considered herein do not have a significant effect on the thermomechanical response of the RVE. The effective stiffness and compressive strength were reduced by 23% and 32% respectively, while the macro-damage initiation strain saw little variation. The damage contour plots show consistent failure behavior until the oxide layer reaches 30 µm, where macroscale failure occurs in thin bands through the thickness of the struts.

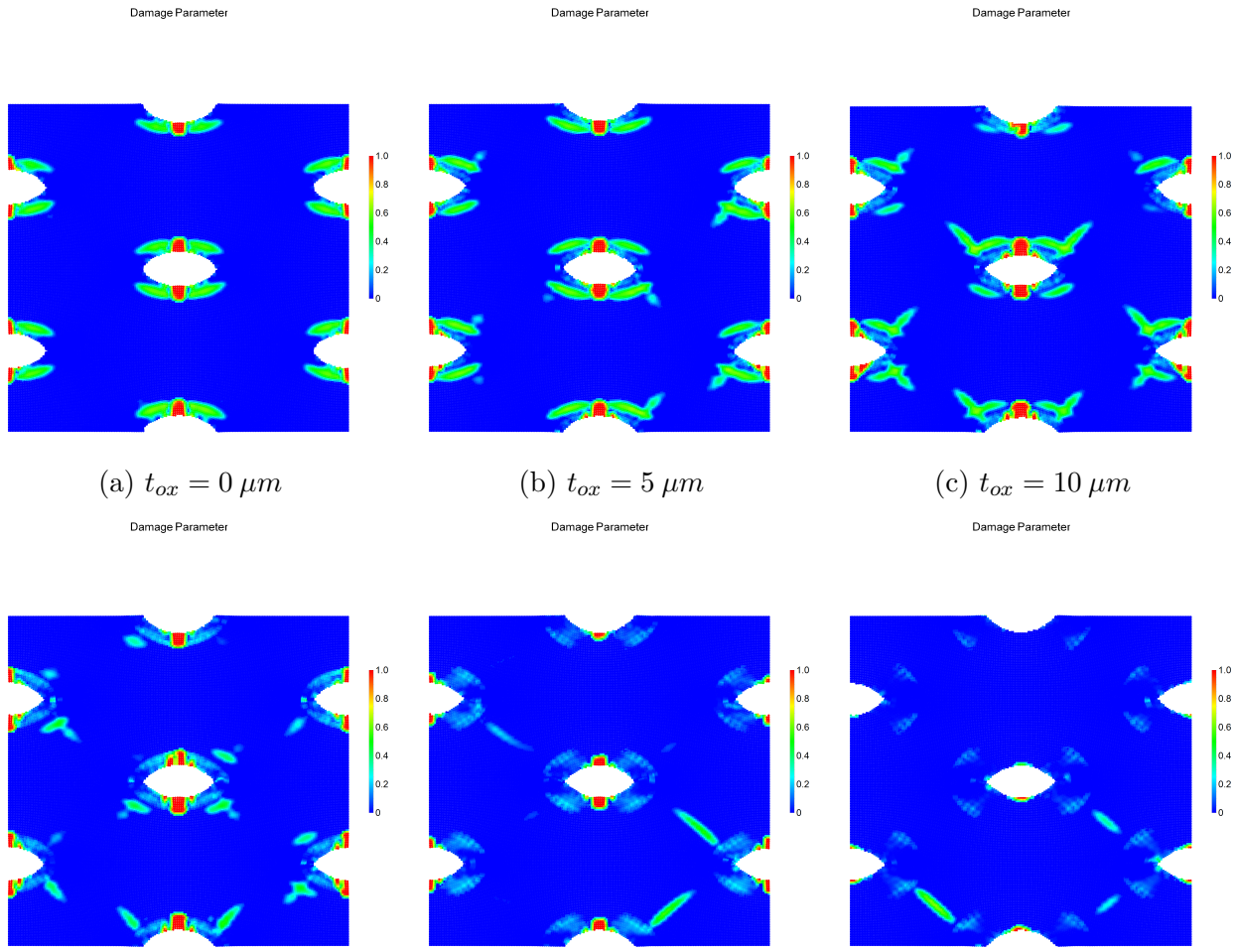

(a) $t_{ox} = 0\ \mu m$ (b) $t_{ox} = 5\ \mu m$ (c) $t_{ox} = 10\ \mu m$

(d) $t_{ox} = 15\ \mu m$ (e) $t_{ox} = 30\ \mu m$ (f) $t_{ox} = 50\ \mu m$

Figure 6.28: Damage field contour plots for hex snapshot with 10% macroporosity showing the response at the corresponding macro-damage initiation strain with varying levels of oxide layer thickness

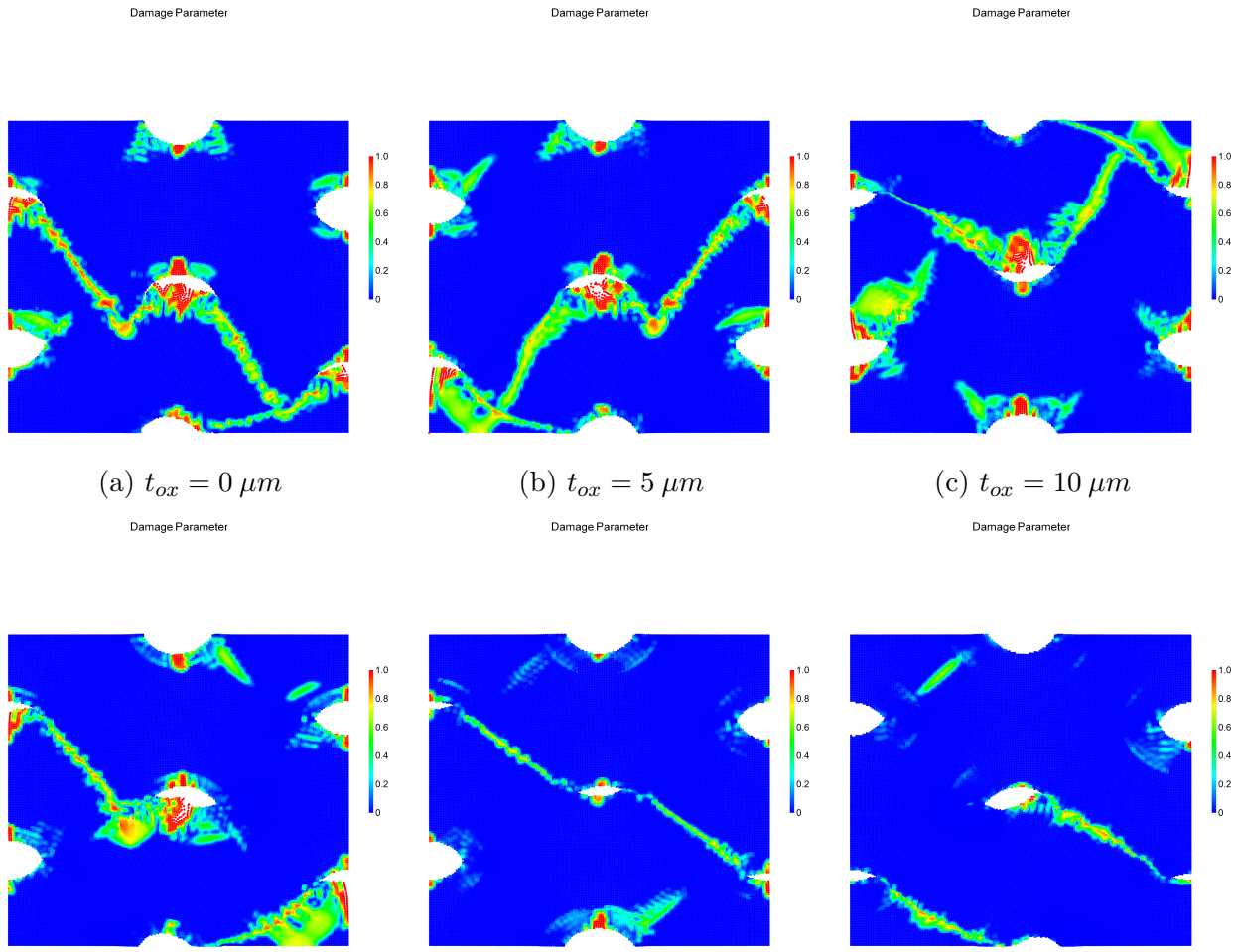

(a) $t_{ox} = 0\ \mu m$ (b) $t_{ox} = 5\ \mu m$ (c) $t_{ox} = 10\ \mu m$

(d) $t_{ox} = 15\ \mu m$ (e) $t_{ox} = 30\ \mu m$ (f) $t_{ox} = 50\ \mu m$

Figure 6.29: Damage field contour plots for hex snapshot with 10% macroporosity showing the response at 21% applied engineering strain with varying levels of oxide layer thickness

6.2.3 Mechanical Response of Hex Snapshots with 70% Porosity

To conclude the characterization of the hex snapshot mechanical responses, thermomechanical simulations comprised of compressive applied strain and ramped thermal loading were performed for snapshots containing 70% macroporosity. The volume-averaged stress-strain curves presented in 6.30 show similar behavior between σ_{11} and σ_{22}, both of which exhibiting macroscale failure at lower strain levels than seen in the 10% and 40% macroporosity snapshots. The volume-averaged damage-strain plots in Figure 6.31 indicate that while the damage in the 5 µm snapshot is higher in magnitude than the unoxidized RVE, further oxidation causes a net reduction in the damage accumulation, though the damage behavior is similar across the oxidation levels.

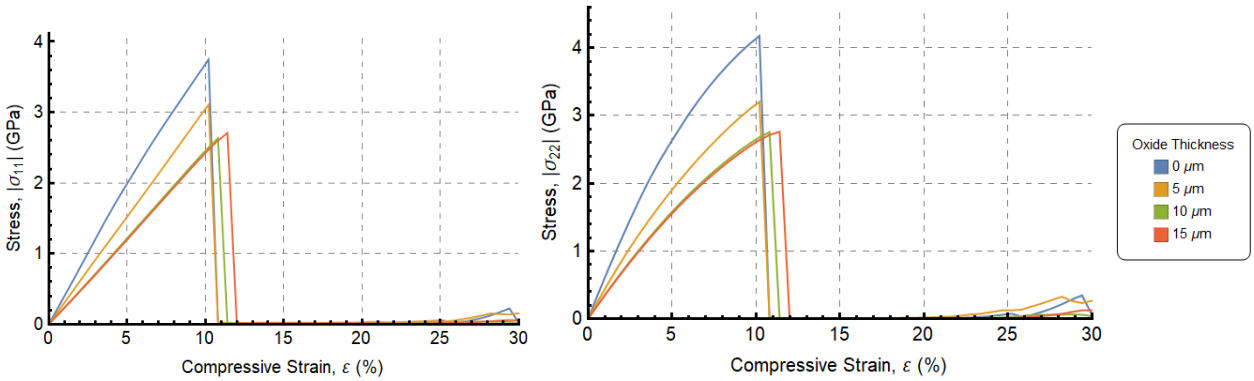

(a) Stress 11-Component (b) Stress 22-Component

Figure 6.30: Stress vs. compressive strain curves for hexagonal RVEs with 70% macroporosity subjected to the ramped thermal load at varying levels of oxidation.

The elastic and damage properties for this set of simulations is presented in Table 6.7. The effective elastic modulus falls to just 63% of the unoxidized value after the 5 µm oxide layer is introduced. The effective stiffness then falls to a value of 56% of the unoxidized value in the 10 µm snapshot, at which point the oxide layer is percolated. As seen in the 40% macroporosity RVEs, once the oxide percolates, there is no significant decrease in the effective stiffness. The oxide layer causes an initial reduction in the micro-damage initiation

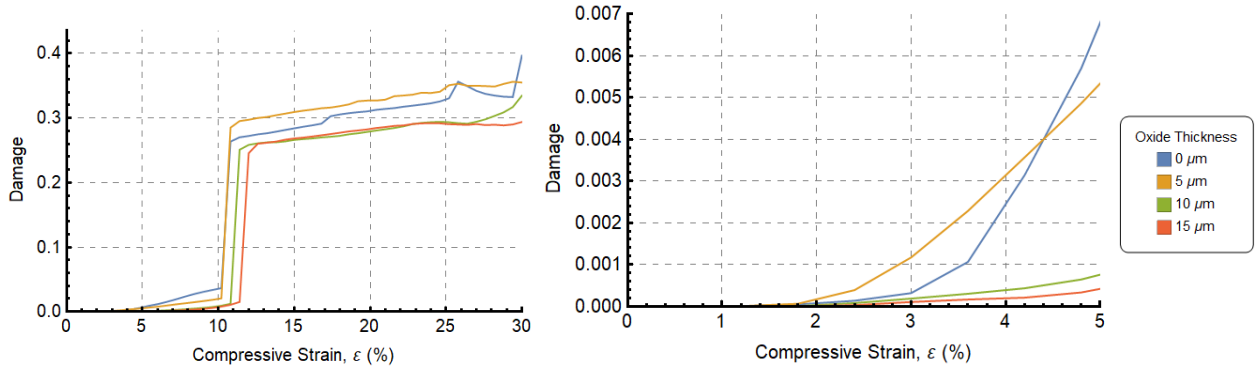

(a) Full Response (b) Initial Response

Figure 6.31: Damage vs. compressive strain curves for hexagonal RVEs with 70% macroporosity subjected to the ramped thermal load at varying levels of oxidation.

strain that can be attributed to the thermal expansion mismatch present. However, once the RVE is fully oxidized, the micro-damage initiation strain reaches a value 58% higher than in the unoxidized RVE. The macro-damage initiation strain is not greatly affected by oxidation, as evidenced by its maximum change of 12% when the RVE is fully oxidized. Similar to the micro-scale damage initiation strain, the compressive strength drops by 23% in the 5 µm snapshot, then settles at a value 34% lower than the unoxidized case for the 10 and 15 µm snapshots.

Table 6.7: Elastic and damage properties of 70% hexagonal RVE snapshots with the ramped thermal load applied at various levels of oxidation

Oxide Thickness (μm)	Effective Elastic Modulus (GPa)	Micro-Damage Initiation Strain (%)	Macro-Damage Initiation Strain (%)	Compressive Strength (MPa)
0	31.7	0.72	10.2	4,175
5	20.1	0.60	10.2	3,203
10	17.8	0.66	10.8	2,755
15	17.63	1.14	11.4	2,761

Figure 6.32 shows the damage field contours at the respective macro-damage initiation strains for each snapshot. These reveal a reduction in the intensity of the through-thickness shear bands present in the struts with increased oxide layer thickness, but the damage hot spots

on the pore surfaces remain active regardless of the oxidation level. This indicates that the damage accumulation in the 70% macroporosity hex is more dependent on the geometric configuration than the composition of the phases. That is not to say the oxide phase material properties have no affect on the response. In fact, the increase in macro-damage initiation strain is attributed to the higher damage initiation strain of TiO_2 delaying the onset of damage in the form of shear bands that would otherwise degrade the stiffness of the RVE struts and cause earlier buckling failure. This is further confirmed by plotting the damage contours at 12% applied strain, shown in Figure 6.33. These plots illustrate that strut buckling remains dominant in these highly porous RVEs.

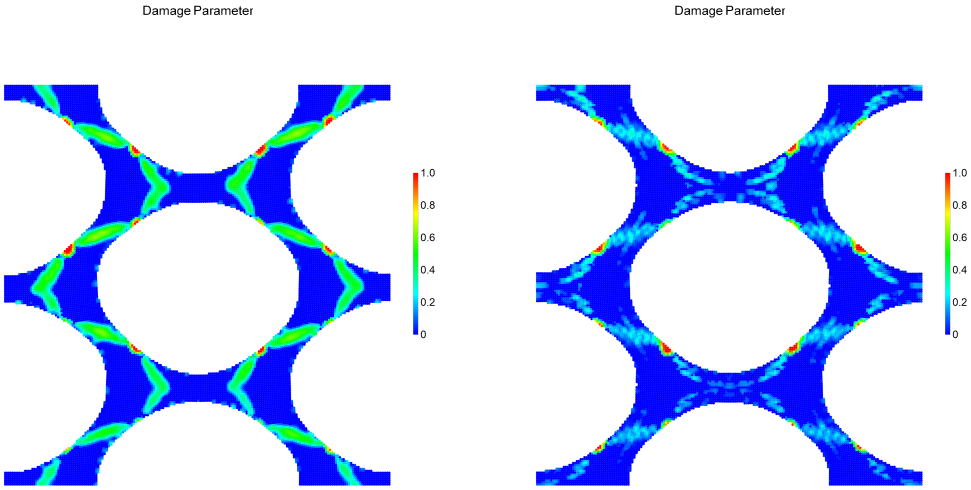

(a) $t_{ox} = 0\ \mu m$

(b) $t_{ox} = 5\ \mu m$

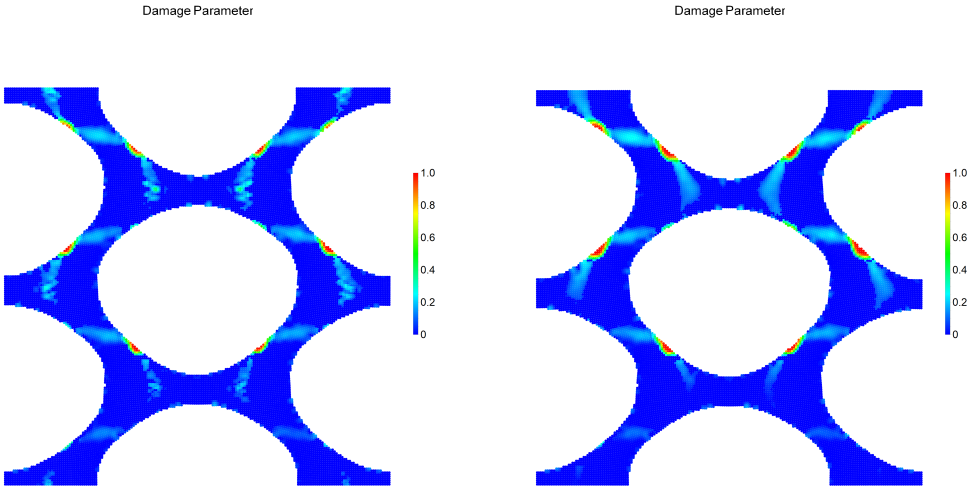

(c) $t_{ox} = 10\ \mu m$

(d) $t_{ox} = 15\ \mu m$

Figure 6.32: Damage field contour plots for hex snapshot with 70% macroporosity showing the response at the corresponding macro-damage initiation strain with varying levels of oxide layer thickness

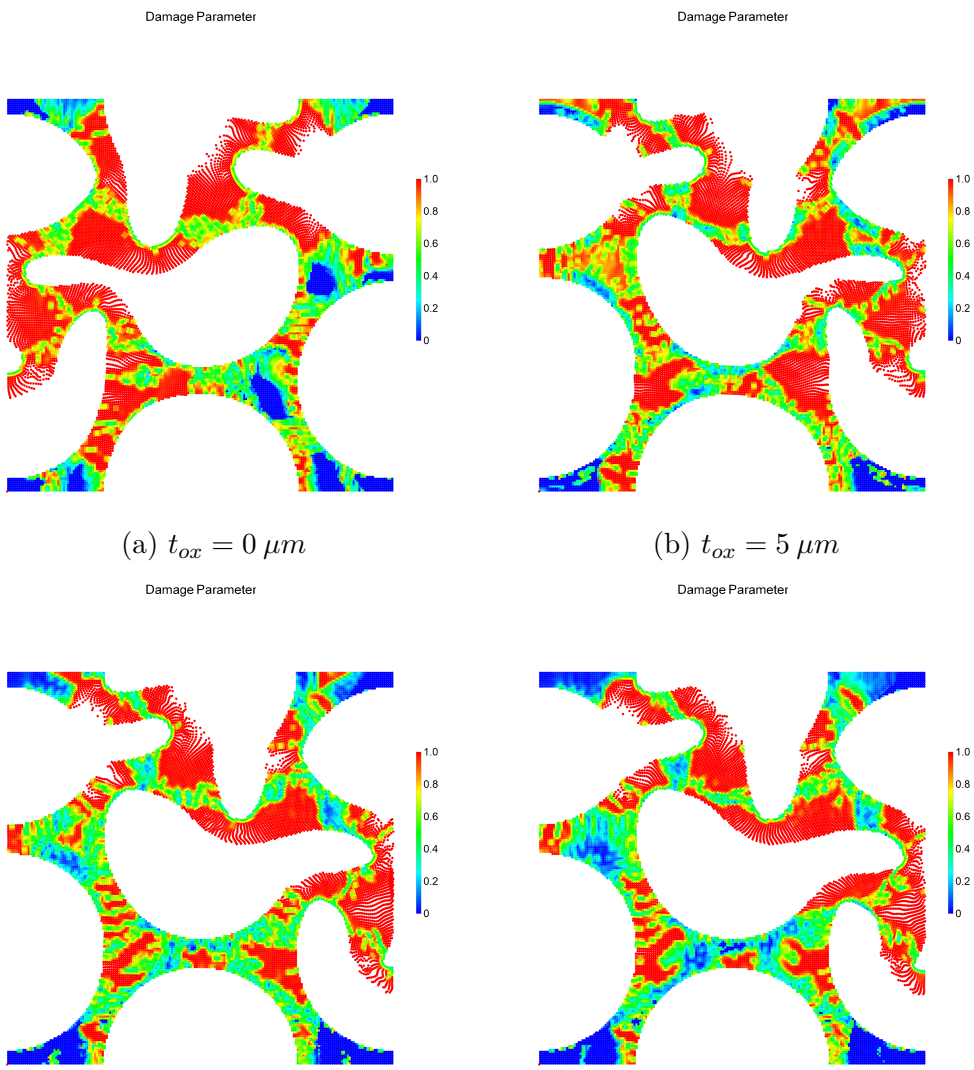

(a) $t_{ox} = 0\ \mu m$ (b) $t_{ox} = 5\ \mu m$

(c) $t_{ox} = 10\ \mu m$ (d) $t_{ox} = 15\ \mu m$

Figure 6.33: Damage field contour plots for hex snapshot with 70% macroporosity showing the response at 12% applied engineering strain with varying levels of oxide layer thickness

6.2.4 Effect of Macroporosity on Hex Snapshot Mechanical Reponse

The elastic and damage comparative metrics for hex snapshots of each volume fraction have been plotted versus oxide layer thickness in Figure 6.34. Note that these results are for combined thermomechanical simulations comprised of compressive applied strain and ramped thermal loading. From these data we can establish trends in the evolution of these properties as a function of oxide layer for various levels of porosity. From the effective elastic modulus plot, it is concluded that the stiffness reduces by an average of 0.5%, 2% and 24% per µm of oxide for macroporosities of 10%, 40% and 70%, respectively, prior to oxide region percolation. After the oxide region percolates, as observed in the snapshots containing 40% and 70% macroporosity, the effective stiffness is not reduced by further oxidation.

The micro-damage initiation behavior is less straightforward to interpret, due to its inconsistent behavior. The micro-damage initiation strain when $t_{ox} = 15\,\mu m$ increases by 54%, 67%, and 58% of the unoxidized value for macroporosities of 10%, 40% and 70%, respectively. While this suggests an average increase in the micro-damage initiation strain of 60%, this is only valid for that level of oxidation. It could vary significantly for less oxidized RVEs, where the damage initiation strain decreases rather than increases. A more useful observation is that the general trend of the micro-damage initiation strain is to increase with oxide layer thickness. It can also be concluded that the transition from bulk- to geometric-based response behavior is dominant in the oxidized RVEs. This is evidenced by the fact that a best-fit line through the micro-damage initiation strain values for each level of macroporosity would be offset by magnitudes decreasing from 70% macroporosity to 10% macroporosity.

The macro-damage initiation behavior in the 10% and 40% snapshots increases until an oxide layer thickness of 10 µm is reached, then both sets of RVEs show a slight decrease

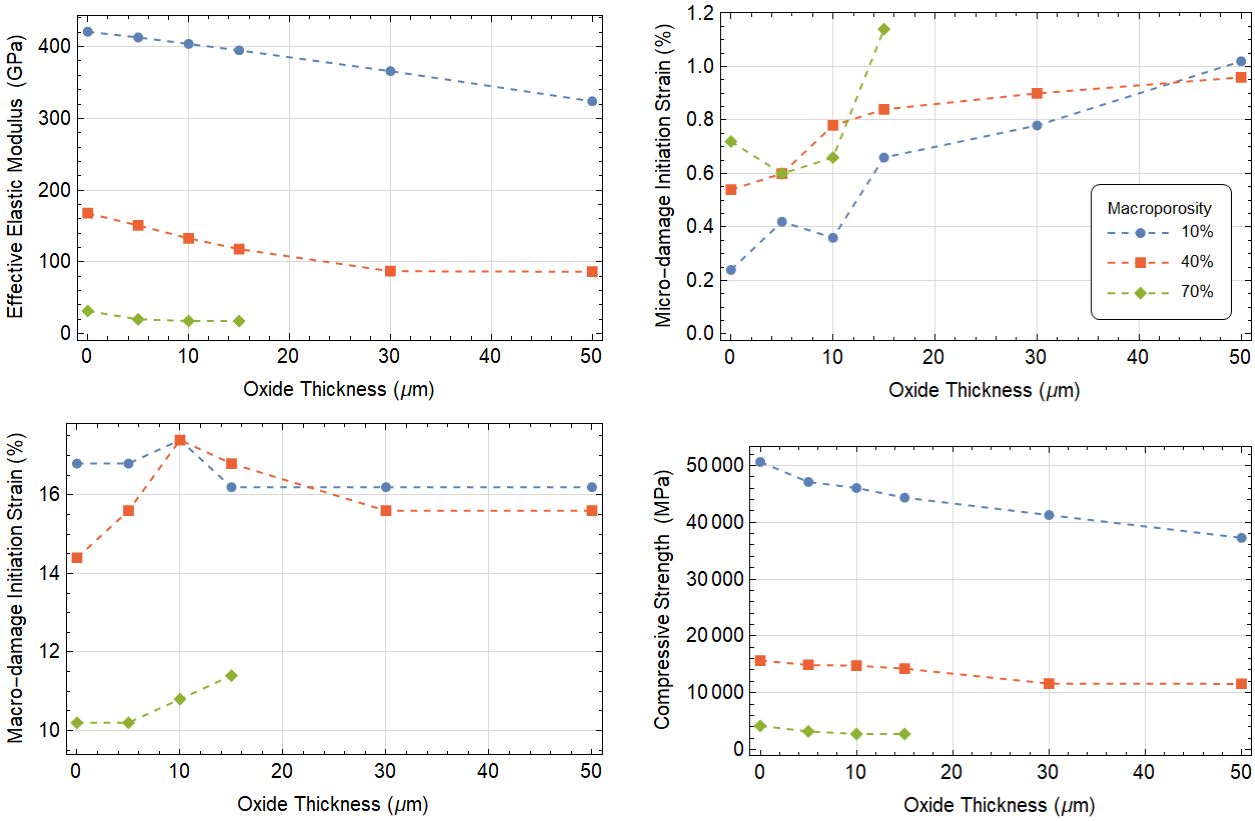

Figure 6.34: Metric comparison for oxidized hex snapshots of all three macroporosity volume fractions subjected to ramped thermal loading.

before reaching a plateau. The plateau is expected in the 40% snapshot due to the oxide percolation, but in the 10% RVE, this is attributed to the transition from catastrophic failure at the pores and through the struts to a more mild form of mild scale failure with less averaged damage accumulation. The 70% macroporosity snapshot experiences continuously increasing macro-damage initiation strain because the oxide phase delays the onset of the strut buckling that causes macroscale failure in these RVEs.

Lastly, the compressive strength follows similar behavior to the effective elastic modulus in that it decreases with increasing oxide layer thickness until the oxide regions percolate. It is concluded that the strength reduces by an average of 0.74%, 0.82% and 3.8% per µm of oxide for macroporosities of 10%, 40% and 70%, respectively, prior to oxide region percolation. It

is important to recognize that the oxide makes up an increasingly greater percentage of the volume fraction as the macroporosity increases, so this change in the strength reduction per µm of oxide is to be expected. The more important takeaway is that the compressive strength is consistently reduced by further oxidizing the RVEs.

6.3 Effective Thermal Conductivity of Hex Snapshots

In the same manner as in Section 5.4, the effective thermal conductivity was determined for each hex snapshot at room temperature (293 K) and 1000 K. The simulation results are provided in Table 6.8, while the rule of mixtures estimates are presented in Table 6.9. To begin making sense of these results, it is expected that the decrease in effective thermal conductivity is greater in RVEs with high macroporosity due to greater presence of the TiO_2 phase, which has a significantly lower thermal conductivity. Similarly, due to the higher volume fraction of air present in the higher porosity RVEs, the baseline effective thermal conductivity should be notably lower.

Viewing these data plotted against oxide layer thickness in Figure 6.35 illustrates that these expectations are indeed met. Beginning with the 70% macroporosity snapshot, it is observed that both the room temperature and 1000 K thermal conductivity values decrease quickly and plateau once the oxide regions percolate. Similarly, the effective thermal conductivity of the 40% macroporosity snapshots for both temperatures decreases to just 2.67 W/(m-K) when the oxide is 30 µm thick, which is only 1 W/(m-K) higher than the effective conductivity of the fully oxidized 70% snapshot. Given that TiO_2 makes up a lesser portion of the 10% snapshot volume and oxide percolation never occurs, the thermal conductivity of these 10% snapshots decreases gradually with oxide thickness. An apparent trend across all three porosity levels is that the difference between the room temperature and 1000 K effective

thermal conductivity decreases as the oxide layer grows, which is a result of the material property inputs. As a larger percentage of the volume fraction becomes TiO_2, which has no specified temperature dependency in thermal conductivity, the room temperature and elevated temperature simulation results should converge.

Table 6.8: Effective thermal conductivity of hexagonal RVE snapshots at various oxide layer thicknesses as determined by **simulation**

	Effective thermal conductivity $(W/m-K)$					
Oxide Thickness	10% Macroporosity		40% Macroporosity		70% Macroorosity	
(μm)	RT	1000 K	RT	1000 K	RT	1000 K
0	54.7	45.0	28.7	23.6	11.5	9.49
5	52.5	43.2	23.6	19.5	4.90	4.16
10	50.4	41.5	18.8	15.6	1.18	1.17
15	48.1	39.7	14.1	11.8	1.01	1.01
30	41.1	34.1	2.69	2.67	-	-
50	31.3	26.2	2.46	2.46	-	-

Table 6.9: Effective thermal conductivity of hexagonal RVE snapshots at various oxide layer thicknesses as determined by **rule of mixtures**

	Effective thermal conductivity $(W/(m-K))$					
Oxide Thickness	10% Macroporosity		40% Macroporosity		70% Macroorosity	
(μm)	RT	1000 K	RT	1000 K	RT	1000 K
0	60.5	49.8	40.3	33.2	20.2	16.7
5	59.2	48.7	35.1	29.0	11.1	9.31
10	57.8	47.6	29.5	24.5	3.77	3.41
15	56.2	46.4	23.3	19.5	1.69	1.76
30	50.9	42.1	5.15	4.84	-	-
50	42.1	34.9	3.39	3.43	-	-

In Section 5.4, the rule of mixtures was deemed a reasonable upper-bound estimation approach for effective thermal conductivity of unoxidized hexagonal RVEs. For the hex snapshots, the estimate provided by the rule of mixtures scales with the change in volume fraction of each phase. As seen in Figure 6.35, there is a significant overestimation of the effective

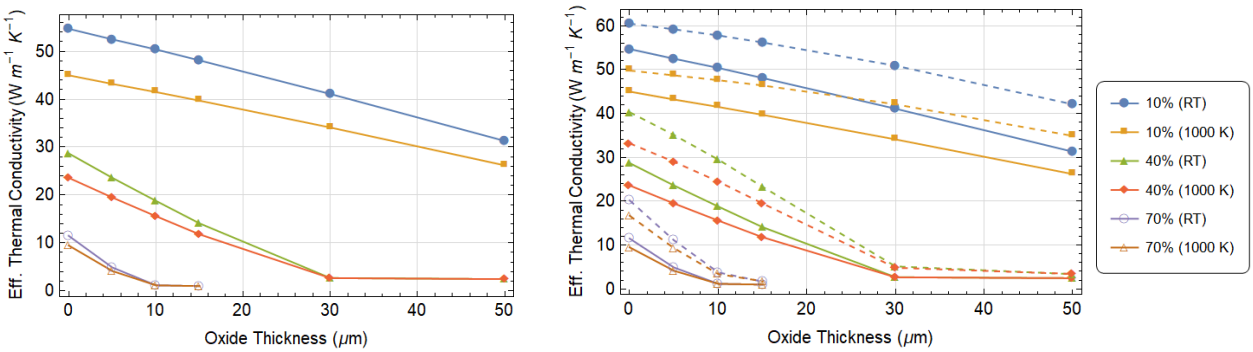

(a) Simulation Results (b) Rule of Mixtures Comparison

Figure 6.35: Effective thermal conductivity vs. oxide thickness at room- and elevated temperatures. Rule of mixtures prediction shown with dashed lines.

thermal conductivity when $t_{ox} = 0$ µm, but the difference drops as the oxide layer thickness increases. This is due to the fact that the oxide layer has a lower thermal conductivity, thus the difference between the air and the oxide phase is less pronounced. As such, the rule of mixtures more closely matches the simulation results once the oxide layer takes over a larger volume fraction of the RVE, compared to TiB_2. In general, the rule of mixtures estimate could again be deemed a reasonable upper-bound for effective thermal conductivity, especially at higher oxidation levels.

To investigate the correlation between damage and thermal conductivity with oxidation present, compressive simulations were performed in the two temperature regimes. The resulting variation in thermal conductivity presented in Figure 6.36 shows that the only discernible difference between the room temperature and 1000 K simulations is increased smoothness of the 1000 K curves for the 10% macroporosity snapshots with 5 to 15 µm of oxide thickness. It is postulated that this is due to the temperature dependence of the specific heat capacity and thermal conductivity of TiB_2 being more significant because it occupies a large percentage of the volume. For all levels of macroporosity, the magnitude of effective thermal conductivity decreases gradually beyond the micro-damage initiation strain, which is to be expected. Due to the strut-shearing failure in the 10% and 40% macroporosity RVEs, there is only a small

drop when catastrophic failure occurs. In the 70% RVE, the thermal conductivity drops off sharply when the struts buckle and most of the RVE becomes completely damaged. Towards the end of the applied load, all three RVEs see a slight increase in thermal conductivity as more self-contact occurs. With the addition of oxide layers of varying thicknesses, these simulations still confirm that the damage model affects thermal conductivity in an intuitive way.

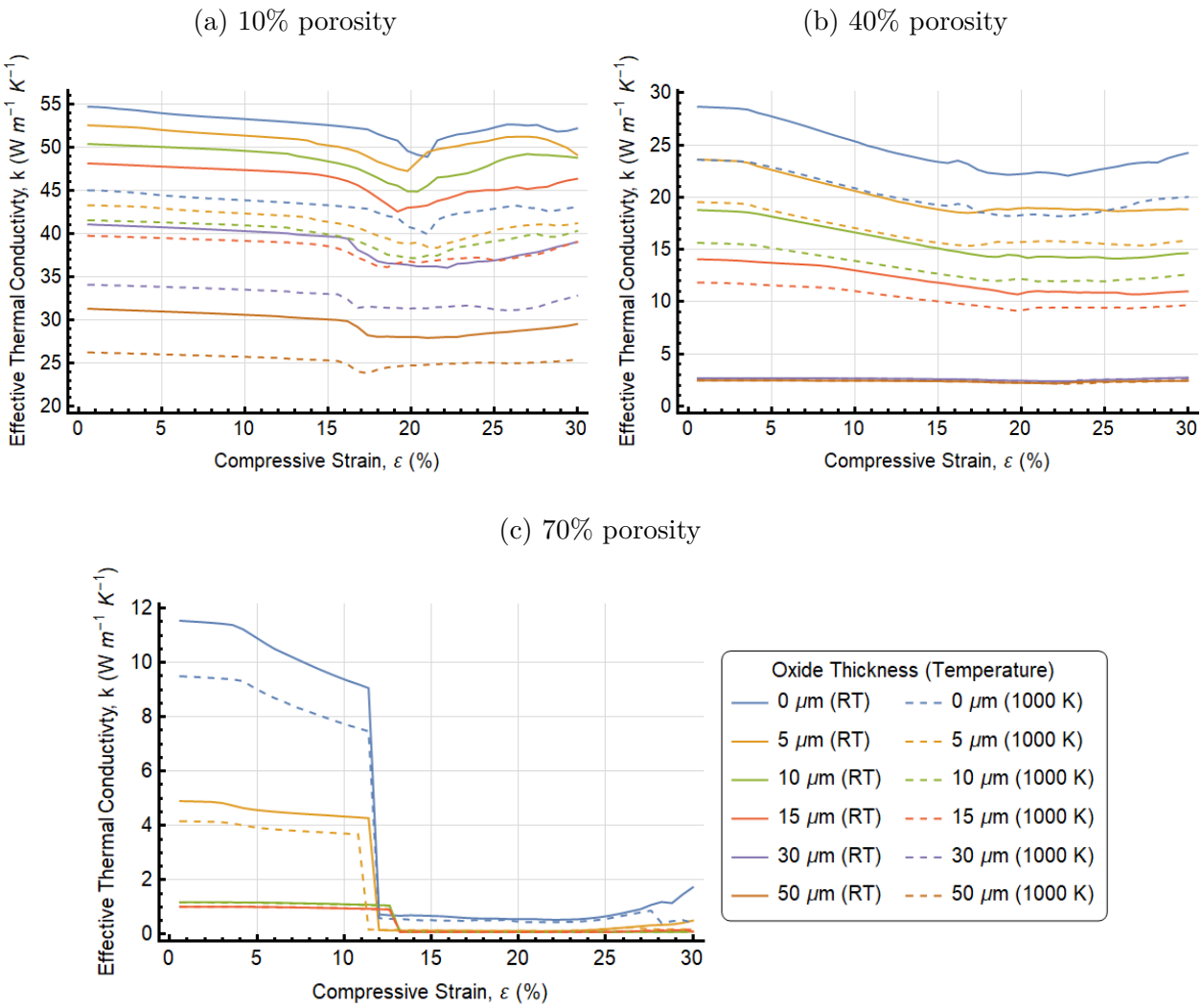

Figure 6.36: Variation of effective thermal conductivity in hexagonal RVEs with the applied engineering load at room temperature and 1000 K

6.4 Extension to Large Porous TiB_2 RVE

Following comparison of the oxidized hexagonal RVEs, focus was shifted to the final goal of this effort: modeling the oxidation effects in RVEs derived from an actual porous UHTC specimen. For the TiB_2 foam investigated by Povolny et al., X-ray micro-computed tomography (µ-CT) images of various specimens were used as the basis for generating such RVEs [27]. Figure 6.37 shows the original image, along with a binarization of the image using a 30% threshold. Povolny found that the binarization process yielded an RVE with 45% macroporosity despite the samples containing 77.1% macroporosity. Artificial porosity was then added back into the RVEs to reach a final macroporosity of 70%. For the purposes of the oxidation study, the snapshot modeling approach was applied to a single large porous TiB_2 RVE.

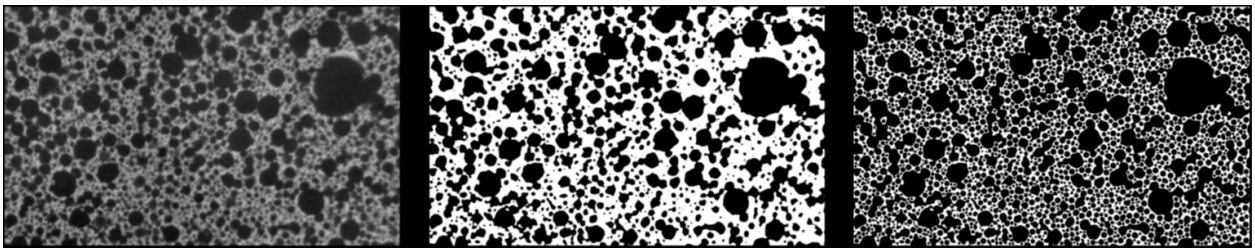

Figure 6.37: Large porous RVE CT image with binarization and addition of artificial porosity performed by Povolny et al. [27]

6.4.1 Large Porous RVE & Boundary Conditions

The large porous RVE used in the present work and its corresponding mechanical boundary conditions are shown in Figure 6.38. These boundary conditions match those of the hexagonal RVE snapshots with up to 10% compressive strain being applied at the top boundary. Given that the previously defined ramped and cyclic load profiles were applied to this RVE, the thermal boundary conditions shown in Figure 6.39 also match that of the hex snapshots.

To be consistent with the hex snapshot simulations, oxide layers of 5, 10, 15, and 30 µm were applied to the large porous RVE. These layers are measured locally at all exposed surfaces within the RVE as it is again assumed that any voids are filled with an oxygen rich atmosphere. Figure 6.40 shows each of the oxidized large porous RVE snapshots, which reach full oxidation when $t_{ox} = 30\ \mu m$.

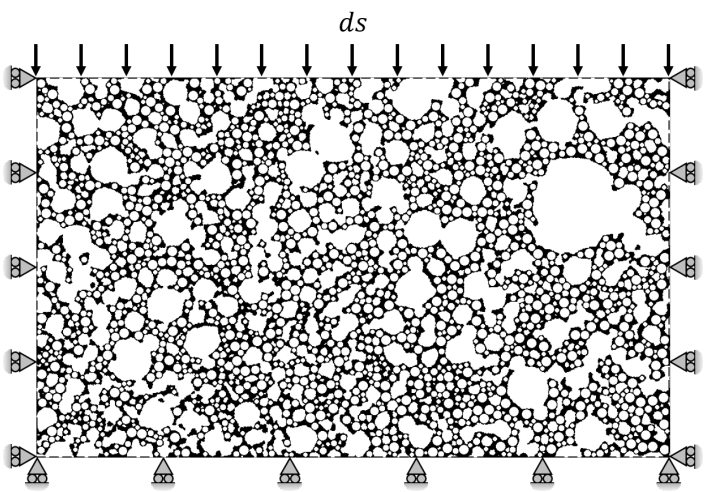

Figure 6.38: Mechanical boundary conditions applied to the large porous RVE. Dashed lines indicate the RVE domain. The boundary conditions are applied directly to the background grid (not shown).

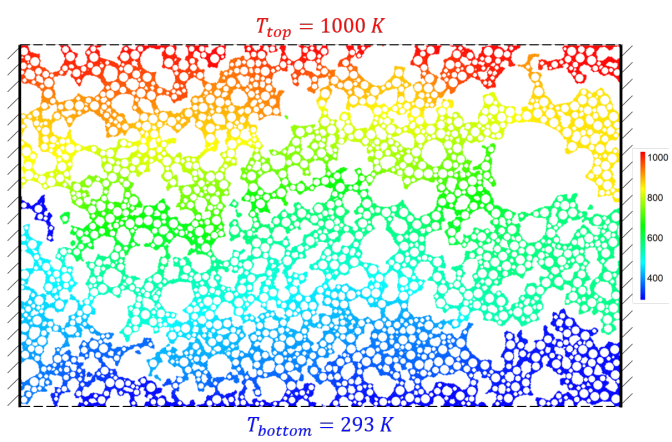

Figure 6.39: Thermal boundary conditions applied to the large porous RVE. This temperature contour snapshot illustrates the thermal gradient due to either applied thermal load reaching its maximum top boundary temperature of 1000 K while the bottom boundary remains fixed at room temperature. The side boundaries are thermally insulated.

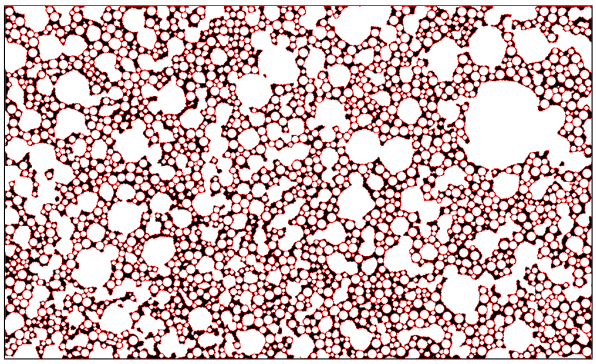

(a) $t_{ox} = 5\,\mu m$

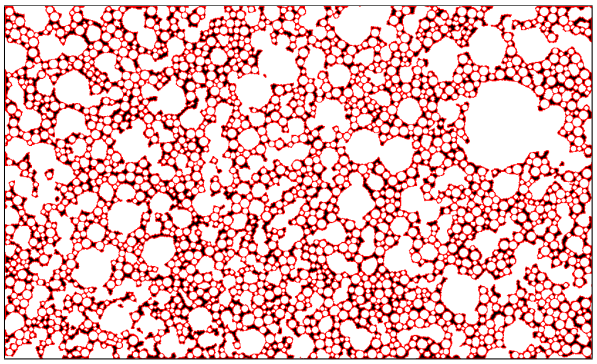

(b) $t_{ox} = 10\,\mu m$

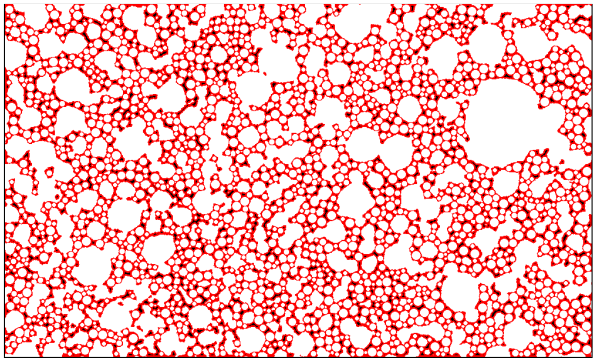

(c) $t_{ox} = 15\,\mu m$

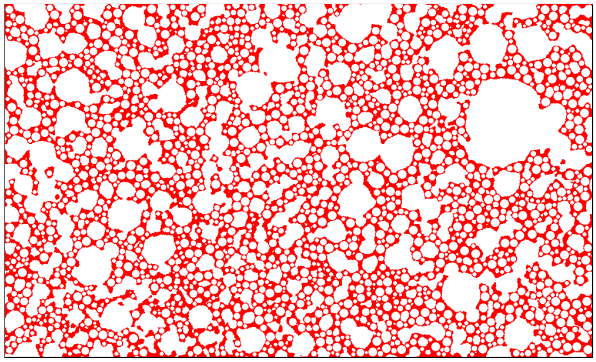

(d) $t_{ox} = 30\,\mu m$

Figure 6.40: Oxidized Large Porous RVE Snapshots with 70% macroporosity

6.4.2 Compression of Large Porous RVE Snapshots

As with the hexagonal RVEs, investigation of the large porous RVE snapshots begins with compressive strain simulations at room temperature. Strains of up to 10% were applied in 0.1% increments and the volume-averaged stress-strain and damage-strain curves are shown in Figure 6.41. The σ_{11} and σ_{22} curves, while differing slightly in magnitude, appear to show very similar behavior. To determine if this response should be expected, the volume-averaged stress components for the unoxidized 70% macroporosity hexagonal RVE were plotted against the unoxidized response of the large porous RVE, as shown in Figure 6.42. This RVE was selected for comparison because its macroporosity level most closely matches that of the large porous RVE. The plot shows that the σ_{11} and σ_{22} curves are indeed very similar, indicating that the large porous RVE response is valid. Furthermore, the magnitudes of the stress components within the large porous RVE are notably lower than in the hexagonal RVE, which suggests that the wide range of pore sizes and shapes has a significant impact on the response, especially compared to the uniform pore distribution in the hexagonal RVE.

It is also observed in Figure 6.41 that there is a distinguishable drop in the magnitude of the stress components after the first oxidation snapshot, but further oxidation has a negligible effect on the response. Due to the nature of the addition of artificial macroporosity in these RVEs, which intentionally places pores such that at least 5 µm thick struts are left in the material, the RVE contains many thin struts that become fully oxidized in the first snapshot. These oxidized struts, shown in Figure 6.43 for the 5 µm snapshot, are scattered throughout the RVE. It is hypothesized that the stiffness reduction in these regions creates a network of thin, flexible joints that reduce the effective stiffness of the RVE. This is explored further by plotting the damage field contours for a small portion of the RVE for different levels of oxidation for 3% compressive strain at room temperature, as shown in Figure 6.44. The circled regions in each contour plot highlight areas where the through-thickness damage of

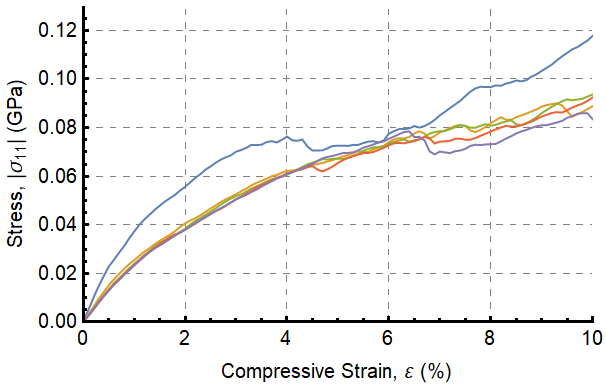

(a) Stress 11-Component

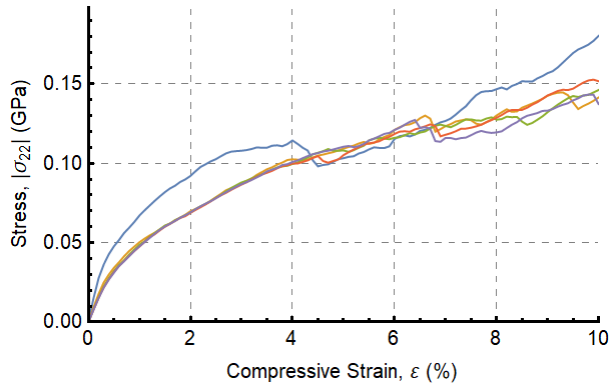

(b) Stress 22-Component

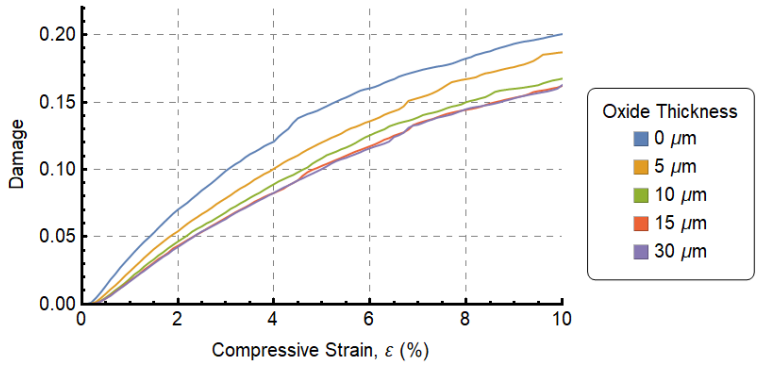

(c) Damage

Figure 6.41: Stress vs. compressive strain curves (a,b) and Damage vs. compressive strain curves (c) for the large porous RVE at room temperature.

the thin struts is reduced as the oxide layer grows from 0 to 15 µm. Despite the reduction of damage observed in these plots and in Figure 6.41(c), the stress-strain response of the oxidized RVEs remains nearly constant. Therefore, it can be concluded that the thin, flexible struts dictate the load-carrying capability of the material.

In terms of the elastic and damage metrics used to compare the hexagonal RVEs, only the effective elastic modulus retains its meaning for the large porous snapshots. A value of 12.4 GPa was calculated for the unoxidized RVE, but this dropped to 7.57 GPa after the first oxide snapshot before decreasing marginally again to 6.63, 6.39, and 6.29 GPa for the 10, 15, and 30 µm snapshots, respectively. The stress- and damage-strain curves for the oxidized

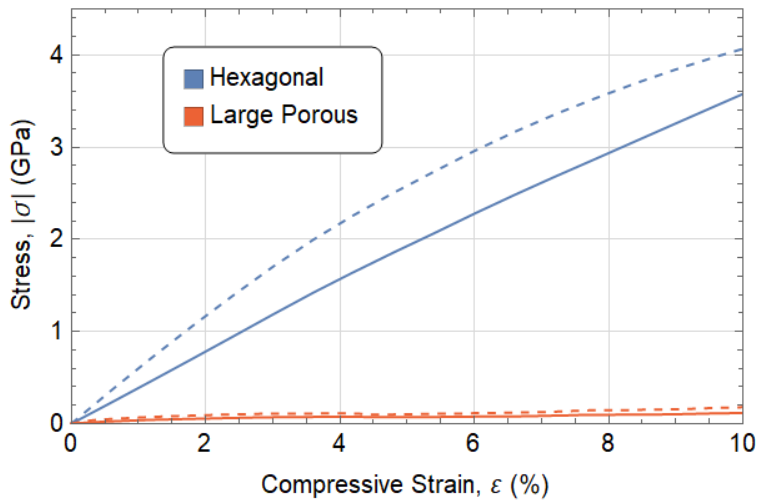

Figure 6.42: Overlay of the volume-averaged compressive stresses in the 1- (solid) and 2-directions (dashed) for the hexagonal RVE with 70% macroporosity (blue) and large porous RVE (red).

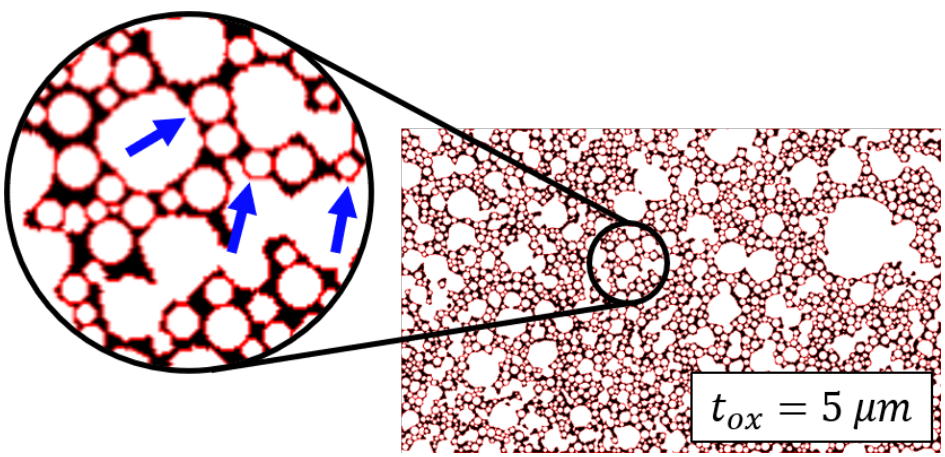

Figure 6.43: Thin struts throughout the RVE are oxidized after just the first snapshot, thus creating a network of flexible joints that strongly influence the overall mechanical response.

RVEs do not exhibit the macroscale failure behavior seen for each of the hex snapshots, thus quantifying the micro- and macro-damage initiation strains or compressive strength would not be useful in characterizing the material. This is caused by a wide distribution of pore sizes and strut thicknesses throughout the RVE. The geometric flexibility caused by the larger pores, combined with the complete damaging of thin struts at low strain levels, causes the stress and damage to increase without the occurrence of a significant failure incident.

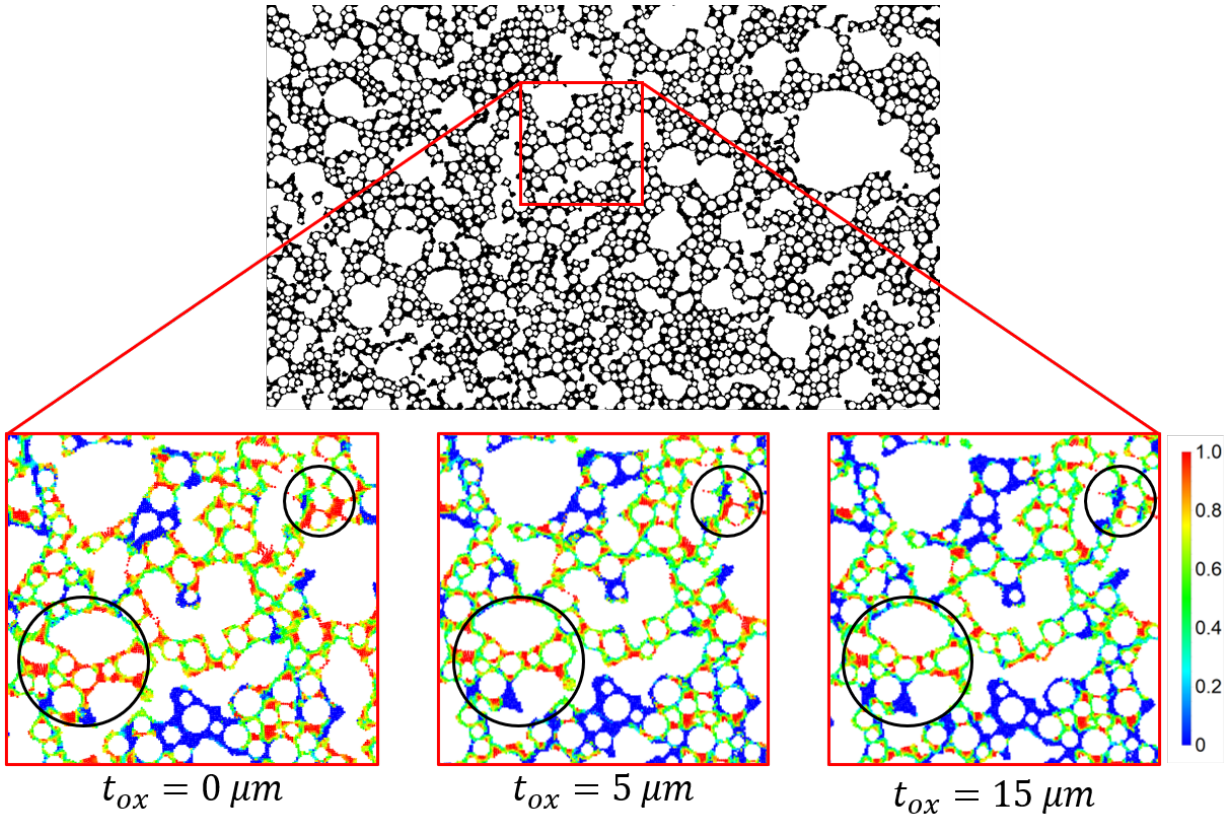

Figure 6.44: Damage contours for a small region of the RVE at oxidation levels of $t_{ox} = 0 - 15\ \mu m$ for a compressive strain of 3% at room temperature.

Effect of Ramped Thermal Loading

With the room temperature mechanical response of the large porous snapshots analyzed, the effects of thermal expansion were introduced by applying the ramped thermal profile to the constrained large porous snapshots. The stress- and damage-time responses are shown in Figure 6.45. Both stress components show similar behavior with a slight offset relative to each other. The damage curves indicate that the damage decreases consistently as the oxide layer is increased, which is consistent with the hexagonal RVE simulations. The damage shown in the 0% µm snapshot is to be expected given the tension that could develop due to thermal expansion in an RVE of such complex geometry.

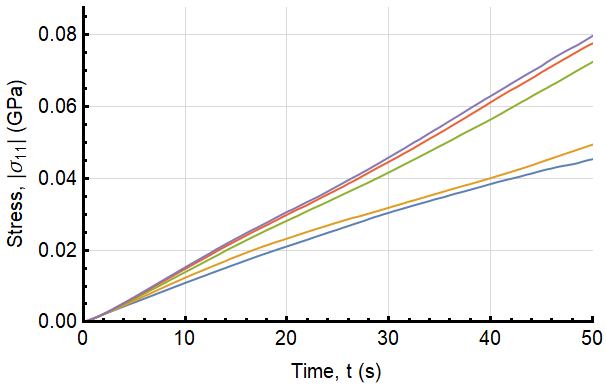

(a) Stress 11-Component

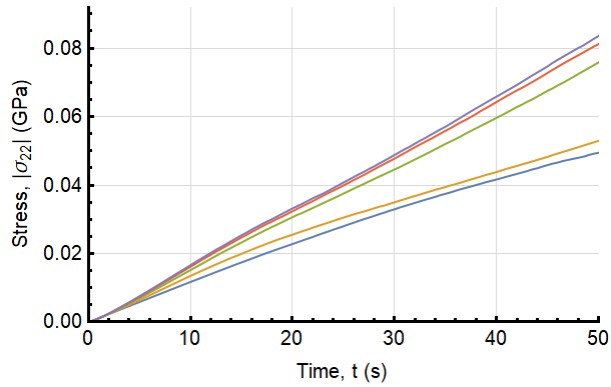

(b) Stress 22-Component

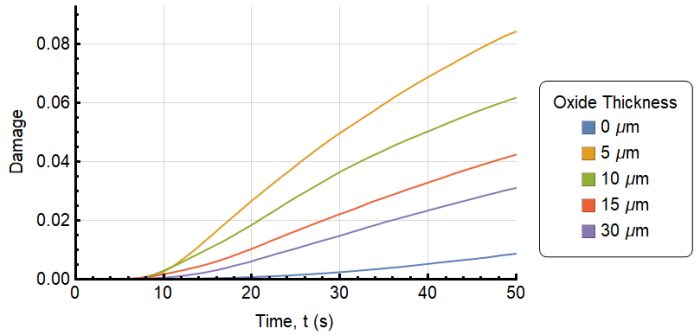

(c) Damage

Figure 6.45: Stress-time curves (a,b) and damage-time curves (c) for the large porous RVE subjected to constrained ramped thermal loading.

Next, compressive loading up to 10% was combined with the ramped thermal load profile. The volume-averaged stress- and damage-strain curves are shown in Figure 6.46, which exhibit very similar behavior to the room temperature simulations. The magnitude of the stress curves is shifted upward due to the addition of thermal stresses, while the damage curves are shifted downward with the exception of the 5 µm snapshot. The damage due to thermal expansion, as shown in Figure 6.45(c) is the highest in the 5 µm snapshot, so this behavior makes sense. The effective elastic modulus for the unoxidized RVE increased by 0.1 GPa for due to the thermal load, while an average change of 0.14 GPa for the oxidized snapshots was observed.

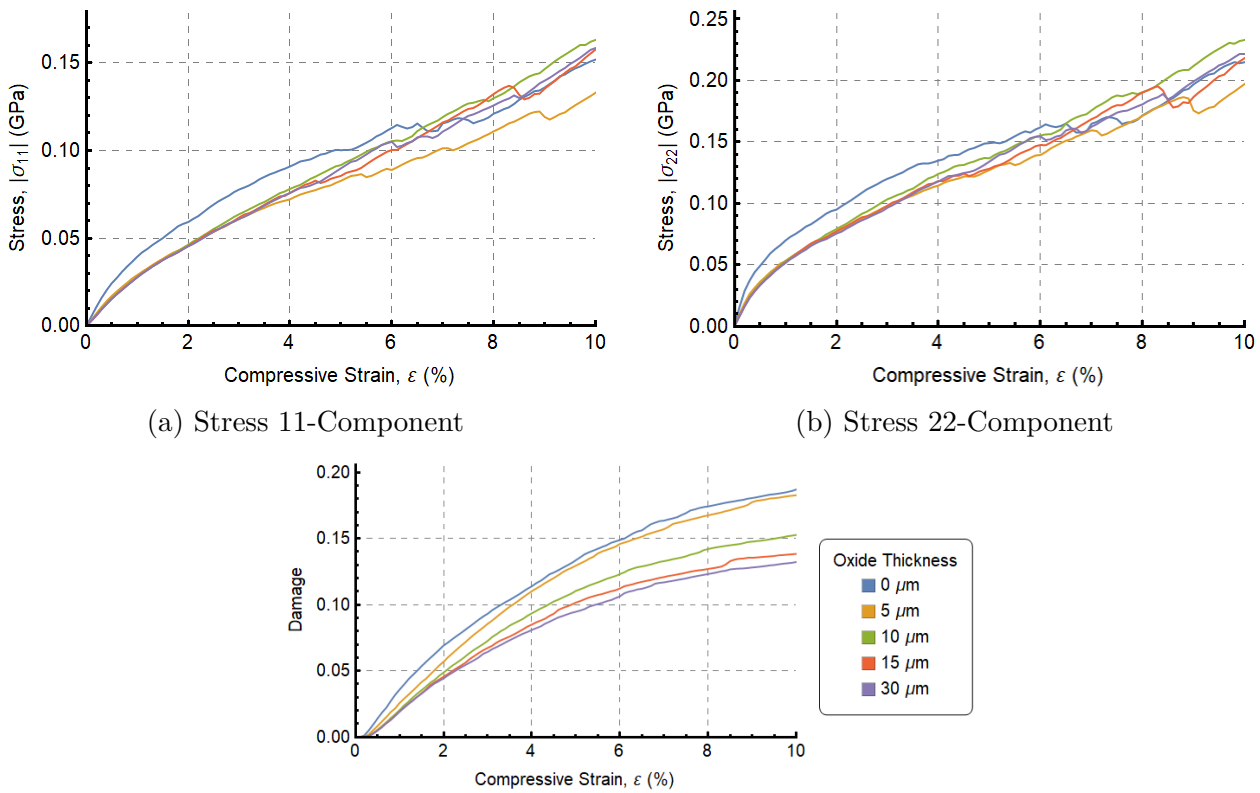

(a) Stress 11-Component

(b) Stress 22-Component

(c) Damage

Figure 6.46: Stress vs. compressive strain curves (a,b) and Damage vs. compressive strain curves (c) for the large porous RVE subjected to ramped thermal loading.

Effect of Cyclic Thermal Loading

Next, effects of thermal expansion due to a heating and cooling cycle were investigated by applying the cyclic thermal load to the large porous RVE snapshots. The stress- and damage-time curves corresponding to constrained thermal expansion induced by this thermal profile are shown in Figure 6.47. The response is similar to that of the hex snapshots in that the stress component magnitudes increase, reach a plateau where temperature is held constant, then decrease as the top boundary is cooled. The damage profile shows that damage increases with temperature, but there is not enough compression in the RVE during the cooling phase to have the effective damage be reduced by the tensile damage scalar α_t. The damage

instead remains mostly constant during the cooling portion before increasing at the end of the simulation, as was observed in the 40% macroporosity hex snapshots.

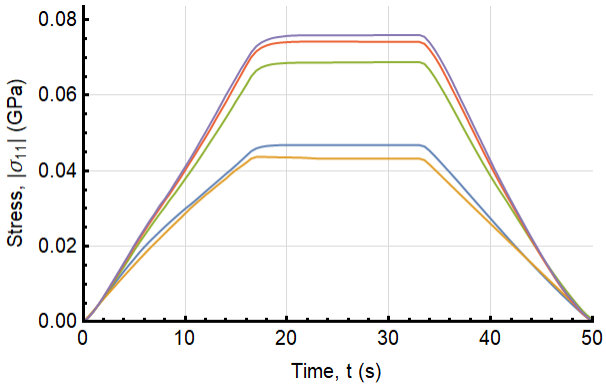

(a) Stress 11-Component

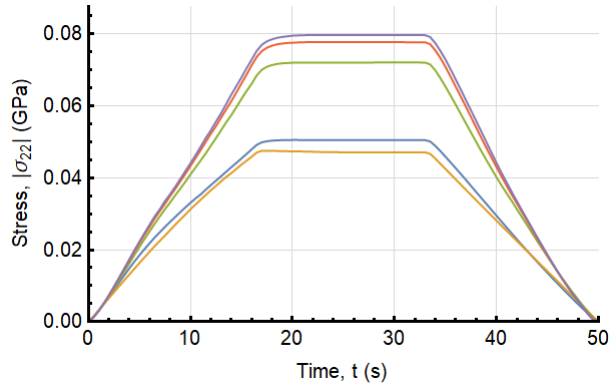

(b) Stress 22-Component

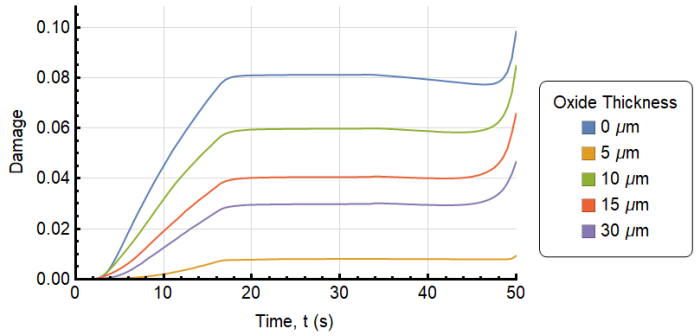

(c) Damage

Figure 6.47: Stress-time curves (a,b) and damage-time curves (c) for the large porous RVE subjected to constrained ramped thermal loading.

Next, compressive loading was combined with cyclic thermal loading. The volume-averaged stress- and damage-strain curves are shown in Figure 6.48, which are strongly affected by the thermal stresses present due to the introduction of the oxide phase. In snapshots where t_{ox} > 5 µm, the stress components increase beyond the unoxidized snapshot curves. TiO_2 is the predominant phase in these RVEs, thus thermal stresses are exaggerated by the subsequent increase in thermal expansion and the higher initial heating rate associated with the cyclic thermal profile. The damage due to thermal expansion, as shown in Figure 6.47(c) is the highest in the 5 µm snapshot and exceeds the damage present in the unoxidized RVE.

Also observed are three distinct regions in the stress-strain curve, the first of which being associated with the initial heating ramp. The temperature is held at 1000 K from strain values of 33.3% to 66.6%, where the stress components are only seen to increase due to mechanical loading. Lastly, the temperature is decreased, thus removing thermal stress from the RVEs and causing the stress components to return to near their final values in the room temperature simulations. The effective elastic modulus for the unoxidized RVE increased by 0.4 GPa due to the cyclic thermal load relative to the room temperature value, while an average change of 0.38 GPa for the oxidized snapshots was observed.

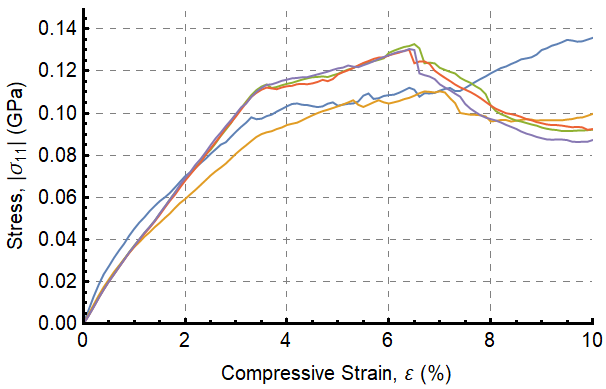

(a) Stress 11-Component

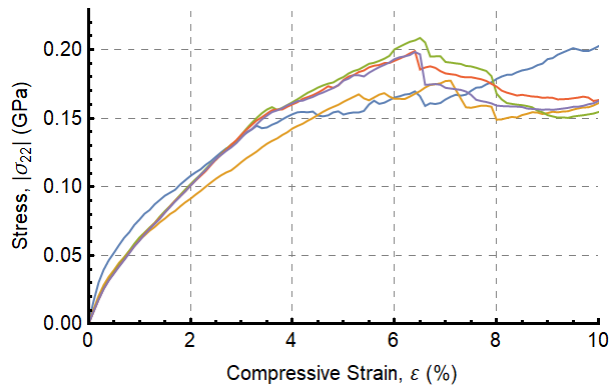

(b) Stress 22-Component

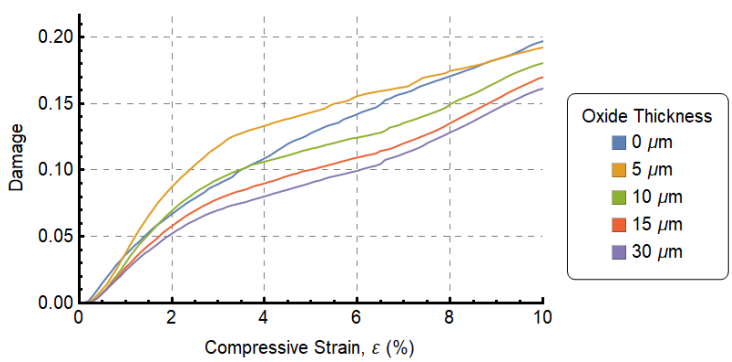

(c) Damage

Figure 6.48: Stress vs. compressive strain curves (a,b) and damage-strain curves (c) for the large porous RVE subjected to cyclic thermal loading.

Comparison of Thermal Loads

In this section, the variation in elastic response due to the change in thermal load for large porous RVEs is discussed. As shown in Table 6.10, there is little variation in the elastic modulus due to the change in thermal load, which makes sense because they each start near room temperature. The notable change in the effective modulus comes from the oxidation. Across these simulations, the elastic modulus decreases by $38 \pm 1\%$ due to the first 5 µm layer, then drops to a final value of $49 \pm 0.7\%$ of the unoxidized value. Aside from the change in elastic modulus, the coupling of oxidation with thermal loading has been shown to cause a large increase in the volume-averaged stress due to the difference in thermal expansion coefficients of the TiB_2 and TiO_2. As in the hex snapshots, the damage accumulation tends to decrease in magnitude as the oxide layer becomes thicker.

Table 6.10: Effective elastic modulus of oxidized large porous RVE snapshots for different thermal load cases.

Oxide Thickness	Effective Elastic Modulus (GPa)		
(μm)	Room Temperature	Ramped Load	Cyclic Load
0	12.4	12.5	12.8
5	7.57	7.72	7.97
10	6.63	6.77	7.01
15	6.39	6.54	6.77
30	6.29	6.42	6.66

6.4.3 Thermal Conductivity of the Large Porous RVE

To conclude this brief investigation of the large porous RVE snapshots, the effective thermal conductivity has been calculated at room temperature (293 K) and 1000 K. The data presented in Table 6.11 and plotted in Figure 6.49 show poor agreement with the results of the 70% macroporosity hex snapshot simulations, which is attributed to the range of pore sizes

present and the thin conductive pathways distributed throughout the RVE. A maximum value of 5.67 W/(m-K) is achieved at room temperature in the unoxidized RVE, while the effective thermal conductivity of the fully oxidized RVEs dropped to just 0.48 W/(m-K). As shown for the hex snapshots, the difference between the room temperature and 1000 K results decreases as oxide thickness increases due to the lack of temperature dependency in the TiO_2 thermal conductivity.

The correlation between damage and effective thermal conductivity is once again explored by determining the effective thermal conductivity as a function of applied compressive strain in both temperature regimes. Figure 6.50 shows that the thermal conductivity drops by over 50% due to the mechanical load in the oxidized RVE, however this decrease is much less noticeable in oxidized RVEs with a significantly lower initial effective thermal conductivity. It can be concluded from these results that the introduction of an oxide layer aids a porous UHTC in its role as a thermal insulator, despite the reduction in load carrying capability.

Table 6.11: Effective thermal conductivity of large porous RVE snapshots at various oxide layer thicknesses as determined by **simulation** [Units: $W/(m-K)$]

Oxide Thickness	Effective Thermal Conductivity	
(μm)	Room Temperature	1000 K
0	5.67	4.67
5	1.39	1.26
10	0.65	0.64
15	0.53	0.53
30	0.48	0.48

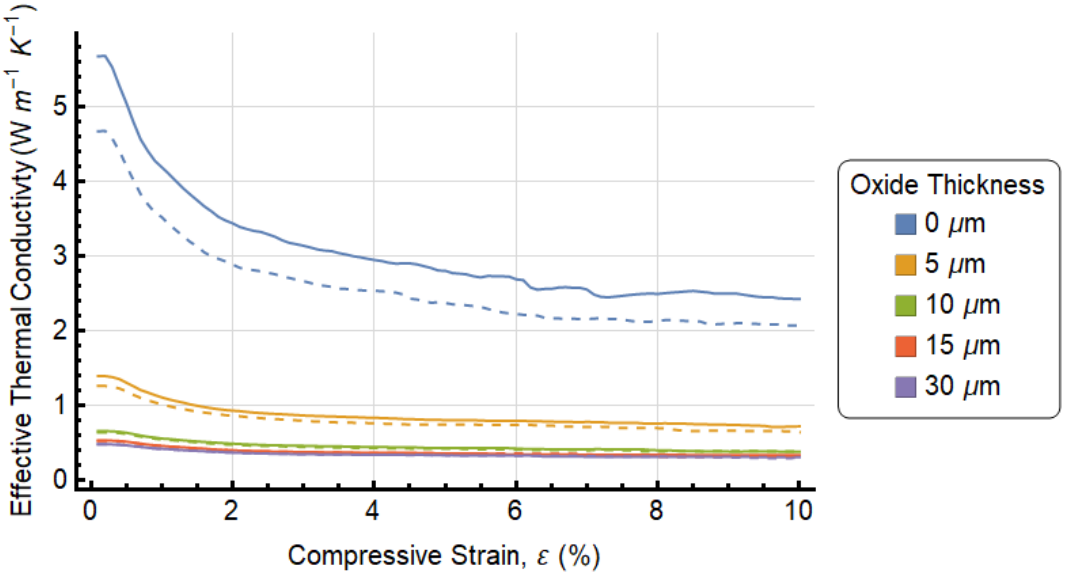

Figure 6.49: Variation of effective thermal conductivity with the applied engineering load at room temperature (solid) and 1000 K (dashed)

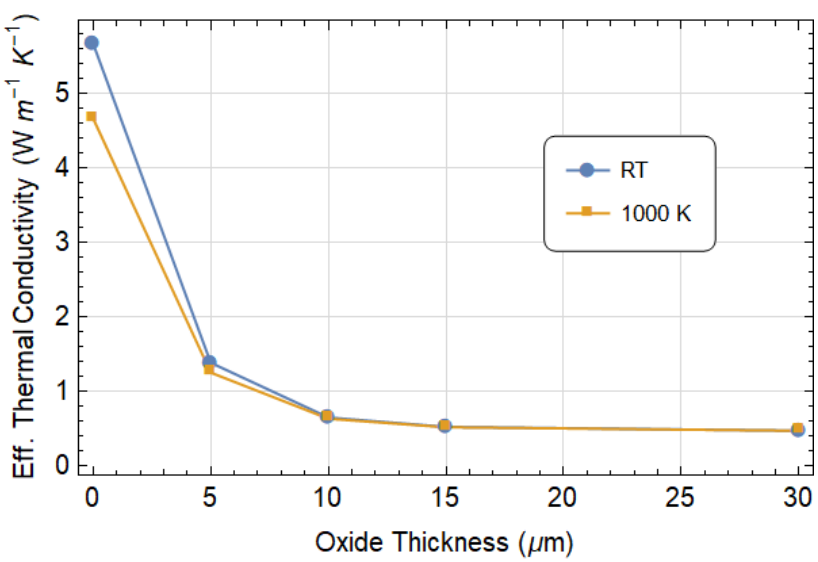

Figure 6.50: Effective thermal conductivity vs. oxide thickness at room temperature and 1000 K

Chapter 7

Conclusions

This thesis presents a first pass at coupling the effects of oxidation with high-temperature material response by employing a snapshot oxidation model derived from experimental data. An existing quasi-static implementation of the material point method was utilized as the computational tool for performing this analysis due to its efficient handling of continuum damage, in addition to the self-contact and large deformations that occur in porous materials under compressive loading. The MPM code allowed 2D plane strain simulations to be performed on RVEs which represent TiB_2 foam, a highly porous UHTC material.

Prior to the oxide snapshot simulations, temperature-dependent functions for the material properties of TiB_2 were developed, then the several uniaxial bar simulations were performed to investigate the use of these functions with uniform and non-uniform temperature distributions. These simulations did not provide a novel result but proved that the material property functions could be effectively implemented within the FEM and eventually the MPM. Following these simple 1D simulations, 2D plane strain simulations were performed on hexagonal RVEs of three different macroporosity volume fractions to characterize the thermomechanical response of the material in the unoxidized state. This was used to establish a baseline for assessing the response with oxidation effects present. These RVEs also contained 30% macroporosity to emulate the multiscale porosity present in TiB_2 foam, which was achieved by using rule of mixtures with the material properties of air. Calibration of the input properties could not be performed due to the lack of experimental data for oxi-

dized UHTCs. This calibration is left as a follow-on effort, should experimental data become available.

Four elastic and damage metrics were introduced to quantitatively compare the results of the simulations being performed. These are the effective elastic modulus, micro-damage initiation strain, macro-damage initiation strain, and compressive strength. It was concluded that the introduction of multi- and macroporosity led to a decrease in effective elastic modulus ranging from 26%, 70% and 94% for 10%, 40%, and 70% macroporosity, respectively, which was attributed to the transition from bulk response to geometric response of the RVE. Contour plots of the damage parameters in these RVEs confirmed that while shear failure in the RVE struts occurs in the 10% and 40% RVEs, the dominant failure mechanism in the 70% RVE is strut buckling, which is a function of the material stiffness and slenderness. Bending in the struts of RVEs with higher porosity was shown to increase the micro-damage initiation strain, although the macro-damage initiation strain decreases with increasing porosity due to their lesser overall tolerance for damage given their thinner struts. The magnitudes of compressive strength for these RVEs were shown to significantly overpredict published values for TiB_2, thus this value was only calculated for relative comparison.

Similar to the macro-damage initiation strain, the compressive strength decreased significantly in RVEs with higher amounts of porosity. The damage accumulation behavior in the hexagonal RVEs was compared, which further highlighted the transition from bulk- to geometric-based response. Damage forms in shear bands through the thickness of the struts, which causes shear failure in the 40% RVE and weakens the struts of the 70% RVE to cause earlier buckling failure. The effects of ramped and cyclic thermal loading were explored in the context of constrained thermal expansion and combined thermomechanical loading. Several conclusions were drawn, namely that while the variation in the elastic and damage metrics due to thermal loading is small, the mechanics behind these variances indicate the

complexity of the thermomechanical modeling being performed. It was shown that temperature dependencies of the elastic modulus, damage initiation strain, and thermal expansion coefficient, combined with the thermal gradient across the RVE, leads to a complex response that affects RVEs of varying porosities in different ways.

The effective thermal conductivity was determined at room temperature and 1000 K for the baseline hexagonal RVEs and was shown to decrease as a function of increasing porosity. Rule of mixtures was concluded to provide a reasonable upper bound for estimating the effective thermal conductivity of these RVEs with greater accuracy shown for lower levels of porosity. Except in the case of catastrophic failure in the 70% macroporosity RVE removing nearly all conductive pathways, the effective thermal conductivity was shown to change minimally due to compressive loading.

After interpreting the results of the baseline hexagonal RVE simulations, the concept of oxidation snapshot modeling was introduced as a means by which the effects of oxidation can be incorporated without implementing a transient, diffusion-based oxidation solver in the MPM code. Instead, simulations were performed on an RVE with a predefined level of oxidation, which does not vary with simulation time. Oxide layers ranging from 5 to 50 µm were applied to the hexagonal RVEs of all three macroporosities, then thermomechanical simulations were performed to determine the oxide layer's impact on the material response. Partially oxidized (pre-percolation) RVEs of 40% macroporosity were shown to endure higher strain levels before macroscale failure due to the increased damage initiation strain of TiO_2, although the effective elastic modulus and compressive strength were reduced by up to 30% and 8.6%, respectively, at room temperature. This reduction in load-carrying capability is due to the reduction in stiffness of the oxide phase. Subsequent oxide percolation in the RVE struts reduces the effective elastic modulus and strength to 48% and 26% of their respective unoxidized values. Further oxidation was shown to have a minimal impact on the stiffness

and load-carrying capability of the material.

Constrained thermal expansion simulations of the 40% macroporosity hex snapshots subjected to ramped thermal loading showed that the thermal expansion coefficient mismatch between the substrate and oxide materials caused volume-averaged damage accumulation on the phase interfaces of up to 1% in the 5 µm snapshot. As the oxide layer thickness was increased, the damage due to thermal expansion diminished, reaching zero when the RVE was fully oxidized. This was attributed to the increase in damage initiation strain associated with the oxide phase material and the reduction in the size of the phase interface regions. Similarly, the higher thermal expansion coefficient of TiO_2 led to an increase in the thermal stress as the oxide layer thickness increased. These same behavioral trends were observed when the snapshots were subjected to cyclic thermal loading, though the magnitude of the volume-averaged stress and damage were increased. The cooling portion of the cyclic thermal loading also caused some tensile stresses to develop, thus a low amount of damage, roughly 3% occurred in the fully oxidized snapshot.

Thermomechanical simulations which combined compressive loading with ramped and cyclic thermal loading were then performed to fully characterize the material response of the 40% macroporosity snapshots. It was shown that because the heating profiles each began at room temperature, there was little variation in the effective elastic modulus, which is computed after the first load step. The micro-damage initiation strain behavior was inconsistent across the thermal load cases, but a general trend was observed where the micro-damage initiation strain decreases with increased heating rate. The macro-damage initiation strain did not change due to applied thermal loading for oxide thicknesses of 10 µm or less, but did decrease by an average of 7% for higher levels of oxidation. In the cyclic thermal load case, the heating rate was high enough to cause a decrease in macro-damage initiation strains at all oxidation levels. Following the study of the 40% snapshots under all thermomechani-

cal loading combinations, simulations with applied compressive strain and ramped thermal loading were performed on the 10% and 70% macroporosity snapshots.

A comparison of the elastic and damage metrics for the 10%, 40%, and 70% macroporosity snapshots led to several conclusions being drawn on the effect of macroporosity in the hex snapshot results. It was first concluded that the stiffness reduces by an average of 0.5%, 2% and 24% per µm of oxide for macroporosities of 10%, 40% and 70%, respectively, prior to oxide region percolation. After the oxide region percolates, as observed in the snapshots containing 40% and 70% macroporosity, the effective stiffness is not reduced by further oxidation. Observation of the micro-damage initiation strain indicates that this quantity increases with oxide layer thickness consistently across RVEs of all microporosities in a general sense, even if the layer-by-layer behavior is somewhat inconsistent. This is attributed to the transition from bulk- to geometry-based behavior being dominant over the oxidation effects.

The macro-damage initiation strain in the 10% and 40% snapshots increases until an oxide layer thickness of 10 µm is reached, then both sets of RVEs show a slight decrease before reaching a plateau. The plateau is expected in the 40% snapshot due to the oxide percolation, but in the 10% RVE, this is attributed to the transition from catastrophic failure at the pores and through the struts to a more mild form of failure with less volume-averaged damage accumulation. The 70% macroporosity snapshot experiences continuously increasing macro-damage initiation strain because the oxide phase delays the onset of the strut buckling that causes macroscale failure in these RVEs. The compressive strength follows similar behavior to the effective elastic modulus in that it decreases with increasing oxide layer thickness until the oxide regions percolate. It is concluded that the strength reduces by an average of 0.74%, 0.82% and 3.8% per µm of oxide for macroporosities of 10%, 40% and 70%, respectively, prior to oxide region percolation. It is important to recognize that the oxide makes up an

increasingly greater percentage of the volume fraction as the macroporosity increases, so this change in the strength reduction per µm of oxide is to be expected. The more important takeaway is that the compressive strength is consistently reduced by further oxidizing the RVEs.

Investigation of the effective thermal conductivity of the hex snapshots revealed that thermal conductivity decreases gradually with an increase in oxide layer thickness until percolation occurs, at which point the change in thermal conductivity plateaus. The effective thermal conductivity of the 40% macroporosity snapshots for both temperatures decreased to just 2.67 W/(m-K) when the oxide is 30 µm thick, which is only 1 W/(m-K) higher than the effective conductivity of the fully oxidized 70% snapshot. From this, it is concluded that the reduced thermal conductivity of the oxide phase drives the effective thermal conductivity of the RVE, rather than the level of macroporosity present. It was also concluded that the effective thermal conductivity does not vary greatly with compressive load due to self-contact which occurs in the 10% and 40% macroporosity snapshots. As with the unoxidized hexagonal RVEs, comparison of the hex snapshot results confirms that the rule of mixtures estimate could be deemed a reasonable upper-bound for effective thermal conductivity, especially at higher oxidation levels.

The final portion of this research effort was extending the snapshot oxidation modeling approach to RVEs derived from an actual porous UHTC specimen. Oxide layers up to 30 µm were applied to one of the large porous TiB_2 foam RVEs generated by Stefan Povolny, then compressive strains up to 10% were applied along with the ramped and cyclic thermal loads. It was observed in the initial room temperature simulations that there is a distinguishable drop in the magnitude of the stress components after the first oxidation snapshot (5 µm), but further oxidation has a negligible effect on the response. The volume-averaged damage in these snapshots decreased as oxide layer was increased, although the magnitude of both

stress components remained nearly constant. Therefore, it was concluded that the load carrying response of the large porous RVE is dominated by many thin, flexible struts that become fully oxidized in the first oxidation snapshot.

The effective elastic modulus of the large porous RVEs reduced to just 47% of the unoxidized value for an oxide thickness of 10 µm. This is similar to the behavior of the 70% macroporosity hex snapshots. These RVEs were not seen to exhibit macroscale failure, thus quantifying micro- and macro-damage initiation strains or compressive strength would not have been useful in characterizing the material response. This is caused by a wide distribution of pore sizes and strut thicknesses throughout the RVE. The geometric flexibility caused by the larger pores, combined with the complete damaging of thin struts at low strain levels, causes the stress and damage to increase in a parabolic manner without the occurrence of a significant failure incident. Damage due to the introduction of ramped and cyclic thermal loading into the large porous RVE simulations decreases with increasing oxide layer thickness, while the thermal stress increased due to the higher thermal expansion coefficient of TiO_2. The effective thermal conductivity of the large porous RVEs was also investigated and it was determined that the thermal conductivity decreased from 5.67 W/(m-K) to just 0.48 W/(m-K) in the 30 µm (fully oxidized) snapshot.

The following final conclusions are drawn:

- Increasing the porosity in a hexagonal RVE reduces the elastic modulus, macro-damage initiation strain, and compressive strength of the RVE, but the additional bending allowed by the geometric configuration of a highly porous RVE delays micro-damage initiation slightly.

- The largest effect of increasing the heating rate (via ramped or cyclic thermal loading) was the reduction of the macro-damage initiation strain for the 40% and 70% RVEs

and a change in macroscale failure location within the RVE.

- Damage due to constrained thermal expansion is highest in multi-phase snapshots with thin oxide layers, then it diminishes for thicker oxide layers and ultimately reaches zero in the fully oxidized RVEs.

- The effective elastic modulus of the hexagonal RVE snapshots is reduced by an average of 0.5%, 2% and 24% per µm of oxide for macroporosities of 10%, 40% and 70%, respectively, prior to oxide region percolation. After the oxide region percolates, the effective stiffness is not significantly reduced by further oxidation.

- The compressive strength of the hexagonal RVE snapshots is reduced by an average of 0.74%, 0.82% and 3.8% per µm of oxide for macroporosities of 10%, 40% and 70%, respectively, prior to oxide region percolation.

- Interpreting these results in the context of the oxide growth curve presented in Section 6.1.1, it is seen that even small exposure times, up to just 4 minutes, can cause sufficient oxidation to degrade the stiffness and strength of highly porous ceramics by 44% and 34%, respectively. This further reinforces the design challenges present in attempting to implement these materials on a hypersonic flight vehicle which may operate in these temperature regimes for several minutes.

- The lower thermal conductivity of TiO_2 compared to TiB_2 dominates the effective thermal conductivity of the RVE, rather than the level of macroporosity present.

- Rule of mixtures was concluded to provide a reasonable upper bound for estimating the effective thermal conductivity of these RVEs with greater accuracy shown for lower levels of porosity and higher levels of oxidation.

- The load-carrying capability of the large porous RVE is dominated by many thin,

flexible struts that become fully oxidized in the first oxidation snapshot. This small level of oxidation reduced the stiffness of the RVE by 47%, which highlights the impact that oxidation has on highly porous UHTCs.

- The large porous RVEs were not seen to exhibit macroscale failure, thus quantifying micro- and macro-damage initiation strains or compressive strength would not have been useful in characterizing the material response.

In conclusion, the simulations performed in this study demonstrate the complexity of the thermomechanical phenomena in porous UHTCs subjected to oxidation, compressive strains, and a variety of thermal loading conditions. This work sets the foundation for further modeling of oxidation effects, such as through the implementation of a diffusion-based oxidation model that is solved alongside thermal and mechanical governing equations to provide more accurate coupling of the three. In addition to a diffusion solver, further refinements of the tool include capturing the effects of oxidation-induced porosity, which affects the oxidation rate and depth, in addition to the thermomechanical response of the oxide layer. While there are literature data available for micro-arc oxidized metals, experimental testing of TiB_2 specimens will be required to characterize the amount of porosity present and its resultant effect on the oxide layer mechanical performance. Also of interest is investigating the material response due to compressive loading and unloading. In any case, the results of this thesis offer a starting point for developing a computational tool which can be used to improve the design of UHTC components and accelerate the development of hypersonic flight vehicle platforms.

Bibliography

[1] J. B. Kouroupis, "Flight capabilities of high-speed-missile radome materials," *Johns Hopkins APL Technical Digest*, vol. 13-3, 1992.

[2] T. A. Barber, "A survey of gaps, obstacles, and technical challenges for hypersonic applications," Master's thesis, University of Tennessee, 2012.

[3] D. E. Glass, "Ceramic Matrix Composite (CMC) Thermal Protection Systems (TPS) and Hot Structures for Hypersonic Vehicles," *15th AIAA International Space Planes and Hypersonic Systems and Technologies Conference*, 2008.

[4] C. A. Steeves, M. Y. He, S. D. Kasen, L. Valdevit, H. N. G. Wadley, and A. G. Evans, "Feasibility of metallic structural heat pipes as sharp leading edges for hypersonic vehicles," *Journal of Applied Mechanics*, vol. 76, 2009.

[5] W. G. Fahrenholtz and G. E. Hilmas, "Ultra-high temperature ceramics: Materials for extreme environments," *Scripta Materialia*, vol. 129, 2017.

[6] M. J. Lewis, "Sharp leading edge hypersonic vehicles in the air and beyond," *SAE International Journal of Aerospace*, vol. 108, 1999.

[7] X. Jin, X. Fan, C. Lu, and T. Wang, "Advances in oxidation and ablation resistance of high and ultra-high temperature ceramics modified or coated carbon/carbon composites," *Journal of the European Ceramic Society*, vol. 38, 2018.

[8] A. R. Bahramian, M. Kokabi, M. H. N. Famili, and M. H. Beheshty, "Ablation and thermal degradation behaviour of a composite based on resol type phenolic resin: Process modeling and experimental," *Polymer*, vol. 47, 2006.

[9] T. H. Squire and J. Marschall, "Material property requirements for analysis and design of uhtc components in hypersonic applications," *Journal of the European Ceramic Society*, vol. 30, 2010.

[10] V. Z. Shemet, A. P. Pomytkin, and V. S. Neshpor, "High-temperature oxidation behaviour of carbon materials in air," *Carbon*, vol. 31, 1993.

[11] T. Parthasarathy, R. Rapp, M. Opeka, and R. Kerans, "A model for the oxidation of ZrB_2, HfB_2 and TiB_2," *Acta Materialia*, vol. 55, 2007.

[12] N. Perez, *Electrochemistry and Corrosion Science*. Boston, Massachusetts: Kluwer Academic Publishers, 2004.

[13] W. Engelund, "Hyper-X program overview." Virginia Tech Aerospace and Ocean Engineering Dept. Seminar, 5 2001.

[14] D. Glass, R. Dirling, H. Croop, T. Fry, and G. Frank, *Materials Development for Hypersonic Flight Vehicles*. 14th AIAA/AHI Space Planes and Hypersonic Systems and Technologies Conference, 2006.

[15] Q.-G. Fu, H.-J. Li, X.-H. Shi, K.-Z. Li, and G.-D. Sun, "Silicon carbide coating to protect carbon/carbon composites against oxidation," *Scripta Materialia*, vol. 52, 2005.

[16] H. Hatta, T. Aoki, Y. Kogo, and T. Yarii, "High-temperature oxidation behavior of SiC-coated carbon fiber-reinforced carbon matrix composites," *Composites Part A*, vol. 30, 1999.

[17] N. S. Jacobson, D. J. Roth, R. W. Rauser, J. D. Cawley, and D. M. Curry, "Oxidation through coating cracks of SiC-protected carbon/carbon," *Surface & Coatings Technology*, vol. 203, 2008.

[18] M. M. Opeka, I. G. Talmy, and J. A. Zaykoski, "Oxidation-based materials selection for 2000 °C + hypersonic aerosurfaces: Theoretical considerations and historical experience," *Journal of Materials Science*, vol. 39, 2004.

[19] E. W. Neuman, G. E. Hilmas, and W. G. Fahrenholtz, "Mechanical behavior of zirconium diboride–silicon carbide ceramics at elevated temperature in air," *Journal of the European Ceramic Society*, vol. 33, 2013.

[20] G. Zhao, C. Huang, H. Liu, B. Zou, H. Zhu, and J. Wang, "Microstructure and mechanical properties of hot pressed TiB_2-SiC composite ceramic tool materials at room and elevated temperatures," *Material Science & Engineering A*, vol. 606, 2014.

[21] P. A. Williams, R. Sakidja, J. H. Perepezko, and P. Ritt, "Oxidation of ZrB_2–SiC ultra-high temperature composites over a wide range of SiC content," *Journal of the European Ceramic Society*, vol. 32, 2012.

[22] C. Tallon, D. Chavara, A. Gillen, D. Riley, L. Edwards, S. Moricca, and G. V. Franks, "Colloidal processing of zirconium diboride ultra-high temperature ceramics," *Journal of the American Ceramic Society*, vol. 96, no. 8, pp. 2374–2381, 2013.

[23] C. Tallon and G. V. Franks, *Near-Net-Shaping of Ultra-High Temperature Ceramics*, ch. 5, pp. 83–111. John Wiley & Sons, Ltd, 2014.

[24] G. V. Franks, C. Tallon, A. R. Studart, M. L. Sesso, and S. Leo, "Colloidal processing: enabling complex shaped ceramics with unique multiscale structures," *Journal of the American Ceramic Society*, vol. 100, no. 2, pp. 458–490, 2017.

[25] C. Tallon and G. V. Franks, "Multi-scale porous ultra high temperature ceramics," tech. rep., Melbourne Univ Parkville (Australia), 2015.

[26] D. C. Hicks, Z. Zhou, G. Liu, and C. Tallon, "Aligned continuous cylindrical pores derived from electrospun polymer fibers in titanium diboride," *International Journal of Applied Ceramic Technology*, vol. 16, no. 2, pp. 802–813, 2019.

[27] S. Povolny, G. Seidel, and C. Tallon, "Investigating the mechanical behavior of multi-scale porous ultra-high temperature ceramics using a quasi-static material point method," *Mechanics of Materials (Under Review)*, 2021.

[28] S. Povolny, G. Seidel, and C. Tallon, "Numerical investigation of thermomechanical response of multiscale porous ultra-high temperature ceramics," *Computational Materials Science (In-work)*, 2021.

[29] Y.-H. Koh, S.-Y. Lee, and H.-E. Kim, "Oxidation behavior of titanium boride at elevated temperatures," *Journal of the American Ceramic Society*, vol. 84, 2001.

[30] T. A. Parthasarathy, M. D. Petry, M. K. Cinibulk, T. Mathur, and M. R. Gruberk, "Thermal and oxidation response of UHTC leading edge samples exposed to simulated hypersonic flight conditions," *Journal of the American Ceramic Society*, vol. 96, 2013.

[31] L. Silvestroni, S. Mungiguerra, D. Sciti, G. D. D. Martino, and R. Savinob, "Effect of hypersonic flow chemical composition on the oxidation behavior of a super-strong UHTC," *Corrosion Science*, vol. 159, 2019.

[32] R. G. Munro, "Material properties of titanium diboride," *Journal of Research of the National Institute of Standards and Technology*, vol. 105, 2000.

[33] A. Bongiorno, C. J. Först, R. K. Kalia, J. Li, J. Marschall, A. Nakano, M. M. Opeka, I. G.Talmy, P. Vashishta, and S. Yip, "A perspective on modeling materials in extreme environments: Oxidation of ultrahigh-temperature ceramics," *MRS Bulletin*, vol. 31, 2006.

[34] A. Radhi, V. Iacobellis, and K. Behdinan, "A passive oxidation, finite element kinetics model of an Ultra-High Temperature Ceramic composite," *Composites Part B: Engineering*, vol. 175, 2019.

[35] J. Pelleg, *Diffusion in Ceramics*. Springer, 2016.

[36] H. Hosoda, T. Inamura, T. Shimoyamada, H. Noma, and K. Wakashima, "Phase Reactions of Al-Ti-B Ternary and Al-Ti-B-O Quaternary Systems for Al-based Metal Matrix Composites," pp. 2015–2056, 9 2010.

[37] T. Parthasarathy, R. Rapp, M. Opeka, and M. K. Cinibulk, "Modeling oxidation kinetics of SiC-containing refractory diborides," *Journal of the American Ceramic Society*, vol. 95, 2012.

[38] C. Jiang, C. Schroeder, J. Teran, A. Stomakhin, and A. Selle, "The material point method for simulating continuum materials," May 2016. ACM SIGGRAPH Course Notes.

[39] J. Mazars, "A description of micro- and macroscale damage of concrete structures," *Engineering Fracture Mechanics*, vol. 25, no. 5, pp. 729–737, 1986.

[40] W. R. Inc., "Mathematica, version 12.1." `https://www.wolfram.com/mathematica`, 2020.

[41] J. N. Reddy, *Introduction to the Finite Element Method*. McGraw-Hill Education, 4 ed., 2019.

[42] S. Povolny, *Investigating the Thermo-Mechanical Behavior of Highly Porous Ultra-High Temperature Ceramics using a Multiscale Quasi-Static Material Point Method*. PhD thesis, Virginia Polytechnic Institute and State University, Blacksburg, VA, 2021.

[43] D. C. Hammerand, G. D. Seidel, and D. C. Lagoudas, "Computational micromechanics of clustering and interphase effects in carbon nanotube composites," *Mechanics of Advanced Materials and Structures*, vol. 4, 2007.

[44] N. Savchenko, I. Sevostyanova, T. Sablina, L. Gömze, and S. Kulkov, "The influence of porosity on the elasticity and strength of alumina and zirconia ceramics," vol. 1623, 11 2014.

[45] X. Sun, H. Yang, and T. Mi, "Thermo-structural behaviour prediction of the nose cap of a hypersonic vehicle based on multifield coupling," *International Journal of Aerospace Engineering*, vol. 2020, 2020.

[46] D. G. Isaak, J. D. Carnes, O. L. Anderson, H. Cynn, and E. Hake, "Elasticity of TiO_2 rutile to 1800 K," *Physics and Chemistry of Minerals*, vol. 26, pp. 31–43, 1998.

[47] AZo Materials Inc., "Titanium Dioxide - Titania (TiO_2)." `https://www.azom.com/article.aspx?ArticleID=1179`, 2002.

[48] W. Weibull, "A statistical distribution function of wide applicability," *Journal of Applied Mechanics*, vol. 18, pp. 293–297, 1951.

Appendices

Appendix A

Simulation Result Verification

A.1 Numerical Noise in Constrained Cyclic Thermal Loading Simulations

When performing simulations on the baseline hexagonal RVEs to determine the isolated effect of thermal expansion, the ramped and cyclic thermal loads were applied separately to fully constrained RVEs with no applied engineering strain. While no damage accumulated due to the ramped thermal load, Figure A.1 shows that damage accumulated in the hexagonal RVE with 10% macroporosity near the end of the simulation. While the maximum volume-averaged damage magnitude of roughly 5×10^{-6} is negligible, the result was unexpected for a single-phase material with no mismatch in thermal expansion coefficient.

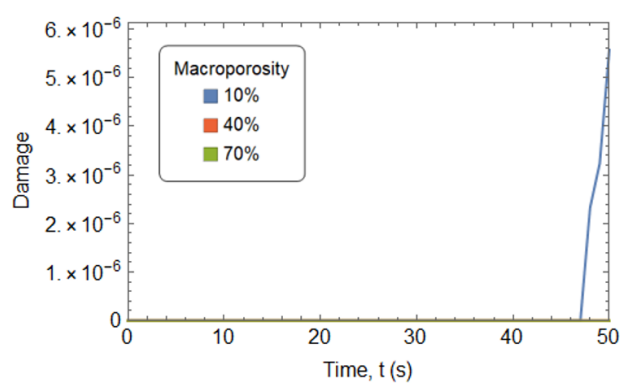

Figure A.1: Damage-time response for fully constrained baseline hexagonal RVEs with no applied engineering strain.

Plotting the damage field contours at the end of the simulation ($t = 50s$), as shown in Figure A.2, revealed that a single material point had become fully damaged, while the rest of the domain was undamaged. With the damage being completely isolated and resulting in a very low volume-averaged damage value, this was determined to be numerical noise. Thus, it is not expected to noticeably impact later simulation results.

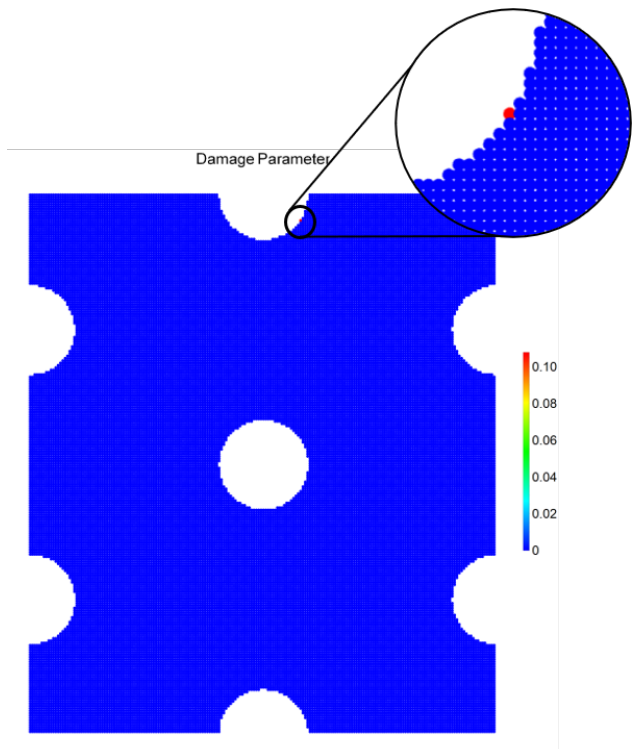

Figure A.2: Damage-field contour plot corresponding to $t = 50s$ the fully constrained baseline hexagonal RVE with 10% macroporosity and no applied engineering strain. The magnified region shows a single damaged material point which is deemed to be numerical noise.